Fakultät für Medizin

Institut für Zellbiologie des Nervensystems

Mitochondrial pathology in acute and chronic neuroinflammation

Yi-Heng Tai

Vollständiger Abdruck der von der Fakultät für Medizin der Technischen Universität München zur Erlangung des akademischen Grades eines

Doctor of Philosophy (Ph.D.)

genehmigten Dissertation.

Vorsitzender: Prof. Dr. Stefan Lichtenthaler

Betreuer: Prof. Dr. Martin Kerschensteiner

Prüfer der Dissertation:

1. Prof. Dr. Thomas Misgeld

2. Prof. Dr. Mikael Simons

Die Dissertation wurde am 22.06.2020 bei der Fakultät für Medizin der Technischen Universität München eingereicht und durch die Fakultät für Medizin am 20.08.2020 angenommen.

Table of Contents

List of Abbreviations

2PEM	Two-Photon Excitation Microscopy (2PM)
AAV	Adeno-Associated Virus
Ab	Antibody
aCSF	Artificial Cerebrospinal Fluid
BBB	Blood-Brain Barrier
BSA	Bovine Albumin Serum
Ca^{2+}	Calcium
CerTN	CerTN-L15 calcium sensor protein
CFA	Complete Freund’s Adjuvant
CIS	Clinically Isolated Syndrome
CNS	Central Nervous System
CSF	Cerebrospinal Fluid
CyPD	Cyclophilin D
DMEM	Dulbecco’s Modified Eagle Medium
DMF	Dimethyl fumarate
DMSO	Dimethylsulfoxide
DMT	Disease-Modifying Treatment
DTA	Diphtheria Toxin A fragment
EAE	Experimental Autoimmune Encephalomyelitis
EB	Ethidium Bromide
EBV	Epstein - Barr virus
EGTA	Ethylene glycol tetraacetic acid
FAD	Focal axonal degeneration
FBS	Fetal Bovine Serum
FDA	Food and Drug Administration (US)
GA	Glatiramer Acetate
FRET	Fluorescence (Förster’s) resonance energy transfer
GaAsP	Gallium arsenide phosphide
GECI	Genetically encoded calcium indicator
GFP	Green fluorescent protein

GM	Grey Matter
GWAS	Genome-wide Association Study
H_2O_2	Hydrogen peroxide
HLA	Human Leukocyte Antigen
IDH3A	Isocitrate dehydrogenase [NAD] subunit alpha, mitochondrial
IFN-β	Interferon-β
IFN-γ	Interferon-γ
IGF-1	Insulin-like Growth Factor 1
Kd	Dissociation constant
MDH2	Malate dehydrogenase, mitochondrial (malate dehydrogenase 2)
MHC II	Major Histocompatibility Complex II
MOG	Myelin Oligodendrocyte Glycoprotein
MRI	Magnetic Resonance Imaging
MS	Multiple Sclerosis
NADH	Nicotinamide adenine dinucleotide
NAGM	Normal-appearing Grey Matter
NAWM	Normal-appearing White Matter
NIRB	Near-infrared Branding
NO	Nitric oxide
OCT	Optical coherence tomography
OPC	Oligodendrocyte progenitor cell
PBS	Phosphate Buffered Saline
PDGFαR	Platelet-Derived Growth Factor-α Receptor
PFA	Paraformaldehyde
PEG	Polyethylene glycol
PEI	Polyethylenimine
PLP	Myelin Proteolipid Protein
PNS	Peripheral Nervous System
PPMS	Primary Progressive Multiple Sclerosis
RNS	Reactive nitrogen species
ROS	Reactive oxygen species
RRMS	Relapsing-Remitting Multiple Sclerosis
S.E.M.	Standard error of the mean

SPMS	Secondary Progressive Multiple Sclerosis
TNF-α	Tumor Necrosis Factor-α
WM	White Matter
XFP	‘X’ Fluorescent Protein

List of Figures

Abstract

Multiple sclerosis (MS), characterized by immune-mediated axonal degeneration, which is a highly correlated to permanent neurological deficits, is the most common cause of non-traumatic disability in young adults. Focal axonal degeneration (FAD) has been identified in MS and acute experimental autoimmune encephalomyelitis (EAE), its animal model, as a potential cellular mechanism of this axon degeneration process. In this process, the axonal pathology starts with normal-appearing morphology and focal swellings induced by reactive oxygen species released from immune cells eventually results in irreversible axon fragmentation[1].

Decoding the underlying mechanisms that mediate this axon degeneration process is an important step towards developing neuroprotective therapies for MS. Mitochondrial pathology was suggested to be preceding the axonal degeneration in acute neuroinflammation. In this project, we aimed to unveil the intricate roles mitochondria play in the pathogenesis of axonal demise in acute EAE. We first investigated the axonal energy state in acute EAE based on the crucial role of mitochondria as an energy supplier in cellular metabolism. Our results suggested a universal axonal energy deficiency in all stages of FAD in acute inflammatory lesions. The deficits lasted to the chronic phase of acute EAE. Next, we explored the relation of essential damage mediators such as calcium and reactive species to mitochondrial and axonal pathology. Somewhat unexpectedly, we found that mitochondrial oxidation and calcium accumulation occur only at the late stages of FAD and are thus unlikely to mediate the initial damage to axons. To obtain a more refined molecular understanding of mitochondrial pathology, we next established an organelle and cell-specific proteomic profile of neuronal mitochondria in acute EAE and depicted differentially regulated mitochondrial proteins and pathways related to the energy metabolism. Our data indicated that an early alteration in the components of the TCA

cycle further strengthens our hypothesis that profound energy deficits associated with mitochondrial dysfunction are important pathogenetic features in neuroinflammatory lesions.

In conclusion, our results improve our understanding of the subcellular and molecular mechanisms underlying axonal energy deficits in neuroinflammatory lesions and can help pave the way towards the development of targeted therapeutic strategies to reverse such deficits.

Zusammenfassung

Die Multiple Sklerose (MS) ist die häufigste nicht-traumatische Ursache für Behinderung bei jungen Erwachsenen Sie ist gekennzeichnet durch eine immunvermittelte axonale Degeneration, die das Korrelat für permanente neurologische Defizite darstellt. Die fokale axonale Degeneration (FAD) wurde bei MS Patienten sowie im in der akuten experimentellen Autoimmunenzephalomyelitis (EAE), einem Tiermodell für Multiple Sklerose, als ein wichtiger Mechanismus dieser immun-vermittelten axonalen Degeneration identifiziert. Die axonale Pathologie beginnt dabei in morphologisch unauffällig erscheinenden Axone, bei denen es anschließend zunächst zu fokalen Schwellungen und schliesslich zur irreversiblen Fragmentierung der Axone kommt[1].

Die Entschlüsselung der zugrunde liegenden Mechanismen ist ein wesentlicher Schritt zur Entwicklung einer effizienten neuroprotektiven Therapie für MS. Da es bereits in frühen Stadien der axonalen Degeneration zu mitochondrialen Veränderungen kommt, wollten wir in diesem Projekt, die molekularen und funktionellen Veränderungen von Mitochondrien im EAE Modell charakterisieren.

Zunächst untersuchten wir dazu den Energiezustand der Axone in der akuten EAE, basierend auf der Rolle der Mitochondrien als Energielieferant im Zellstoffwechsel. Als nächstes analysierten wir wmögliche Schlüssel-Mediatoren der mitochondriale Schädigung wie Kalzium und reaktive Spezies sowie ihre Assoziation mit der axonalen Pathologie. Unsere Ergebnisse deuten auf einen universellen axonalen Energiemangel in allen Stadien der FAD hin. Die Defizite beginnen in der akuten Phase der EAE und hielten bis zur chronischen Phase an. Trotz der frühen morphologischen Veränderungen der Mitochondrien zeigten die Messungen der mitochondriale oxidative Spezies und Kalciumkonzentration aber erst Veränderungen im Spätstadium der Axondegeneration an. Um die grundlegenden molekularen Veränderungen der

Mitochondrien aufschlüsseln zu können, erstellten wir ein Zell- und Organellen-spezifisches Proteom neuronaler Mitochondrien in der akuten EAE mittels eines validierten Isolationsansatzes. Hierbei konnten wir differentiell regulierte mitochondriale Proteine und Protein-Netzwerke im Zusammenhang mit dem Energiestoffwechsel darstellen. Unsere Daten zeigten einen frühen Verlust von wichtigen Komponenten des Citratzyklus an, der eine molekulare Erklärung für die weitverbreiteten axonalen Energiedefizite in entzuündlichen Läsionen liefert. Zusammenfassend verbessern unsere Ergebnisse also unser Verständnis der mitochondrialen Schädigung im entzündeten Nervensystem und können erste Schritte auf dem Weg zur einer rationalen Entwicklung metabolischer Therapiestrategien für die Multiple Sklerose sein.

1. Introduction

1.1 Multiple sclerosis

Although the earliest description of MS dates back to the 14th century[2], multiple sclerosis (MS) was initially defined as a clinical entity by the French neurologist Dr. Jean-Martin Charcot in 1868 as “la sclérose en plaques”. Three clinical indices of multiple sclerosis including intention tremor, nystagmus and telegraphic speech are known to be Charcot triad. The symptoms of MS often carry a lifelong limitation of physical activity and working capacity for the subjects and, as a consequence, cause a massive economic and mental burden on the patients, family, health system and society. A better understanding of this heterogenic neurological disease, therefore is requisite.

1.1.1 Etiology and epidemiology

Multiple sclerosis is an inflammatory autoimmune disease of the central nervous system and is listed as the leading cause of non-traumatic disability[3]. It manifests for the first time mostly in young adults with the peak of incidence at the age of 30 and often progresses with accumulating neurological dysfunction[4]. Roughly 2.3 million people are affected[4] by multiple sclerosis, with an estimated prevalence of about 50-300 per 100,000 people worldwide (Figure 1)[5]. Females are approximately twice as likely to be affected than males[6,7].

Strong impacts of genetic predisposition and environmental factors can help to explain the increased prevalence of MS in specific populations. The high prevalence of MS in immigrants tends to correspond to that of the indigenous populations[8]. The patterns of settlement by the Viking origin has been proposed to support that the complexity of the genetic composition of MS susceptibility has led to the present global distribution of multiple sclerosis given the fact that it is most pronounced in Scandinavia, North America, Australia and New

Zealand[9-11]. Other than the variants of human leucocyte antigens (HLAs) contained within the major histocompatibility complex (MHC) which have been associated with MS[12], non-MHC susceptibility alleles have been identified through Genome-wide association studies (GWAS)[13,14] as well. However, the biological effects of these associated genetic variants are yet to be well established.

Environmental factors, including infectious and non-infectious causes, shape the susceptibility to MS. Infection with Epstein-Barr virus (EBV) for instance, as a noted pathogen with a high prevalence in the population, has been shown to increase the probability of developing the disease. The specific CD4$^+$ T cell-mediated immune response initiated by EBV-encoded antigen reveals a potential link with the pathogenesis of MS, as T cells can cross-recognize EBV and myelin antigens [15,16]. Non-infectious causes such as smoking and vitamin D deficiency have been associated with an elevated risk of MS. The active form of vitamin D acts as an immunomodulator being involved in lymphocyte activation and proliferation, regulatory T cell induction, tissue-specific lymphocyte homing, among others[17]. Epidemiology indicates the MS global prevalence correlates to the latitude, as a higher incidence of MS prevails in the northern regions. In contrast, MS rarely occurs in areas close to the equator. A possible interpretation of this phenomenon is a negative correlation of MS risk to sunlight exposure and related serum vitamin D levels[18,19], suggesting that vitamin D supplementation might be used as a preventive or even therapeutic compound in the treatment of MS [20,21].

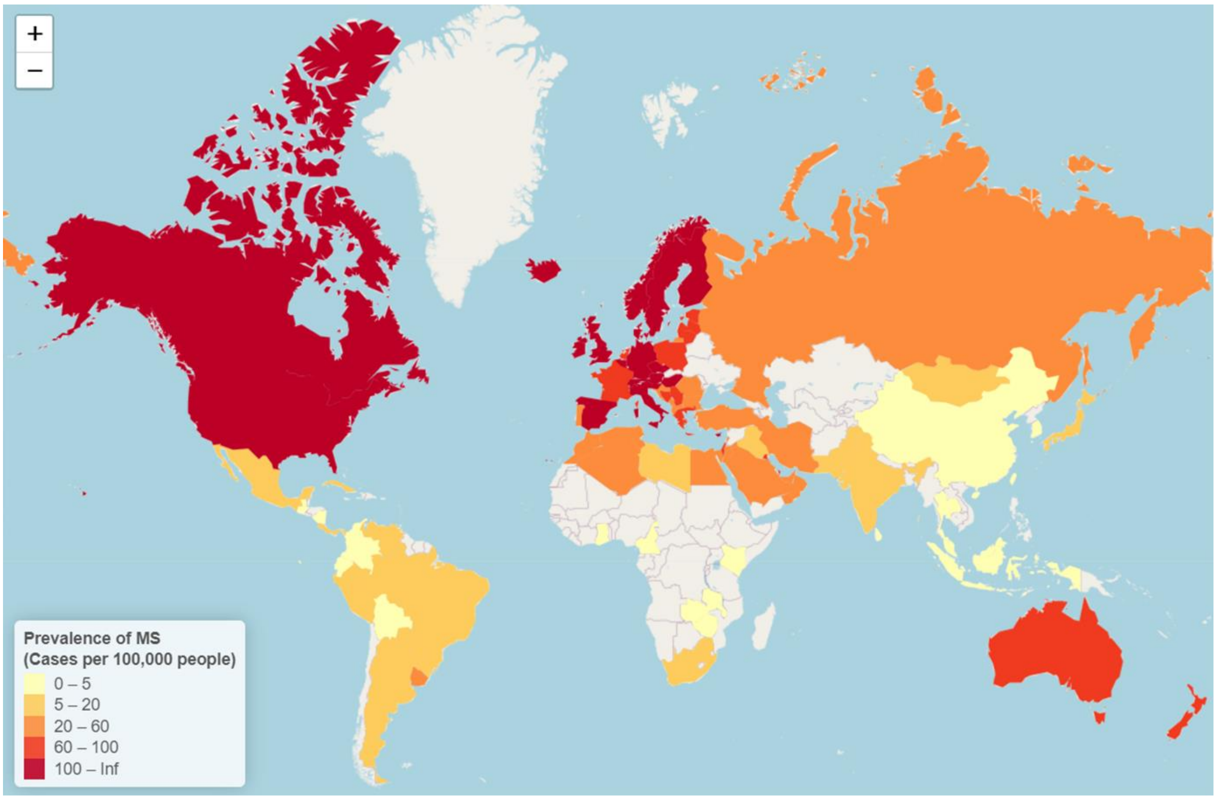

Figure 1: The global prevalence of multiple sclerosis. (Adapted from Atlas of MS 2013, MS International Federation)

1.1.2 Clinical features and diagnosis

The diagnosis of MS is ambiguous and intricate as many of the clinical features are not pathognomonic. The most up-to-date clinical guideline, the refined 2017 McDonald[5] criteria, allows for prediction and early diagnosis of multiple sclerosis. With a combination of laboratory examinations such as CSF oligoclonal band assessment and MRI imaging, it is possible to minimize misdiagnosis. Using contrast-enhanced MRI of the brain and spinal cord, one can visualize lesions at different stages of their development, which are considered in determining dissemination in time. Additionally, the site of lesions is considered in determining the dissemination in space (Figure 2)[4].

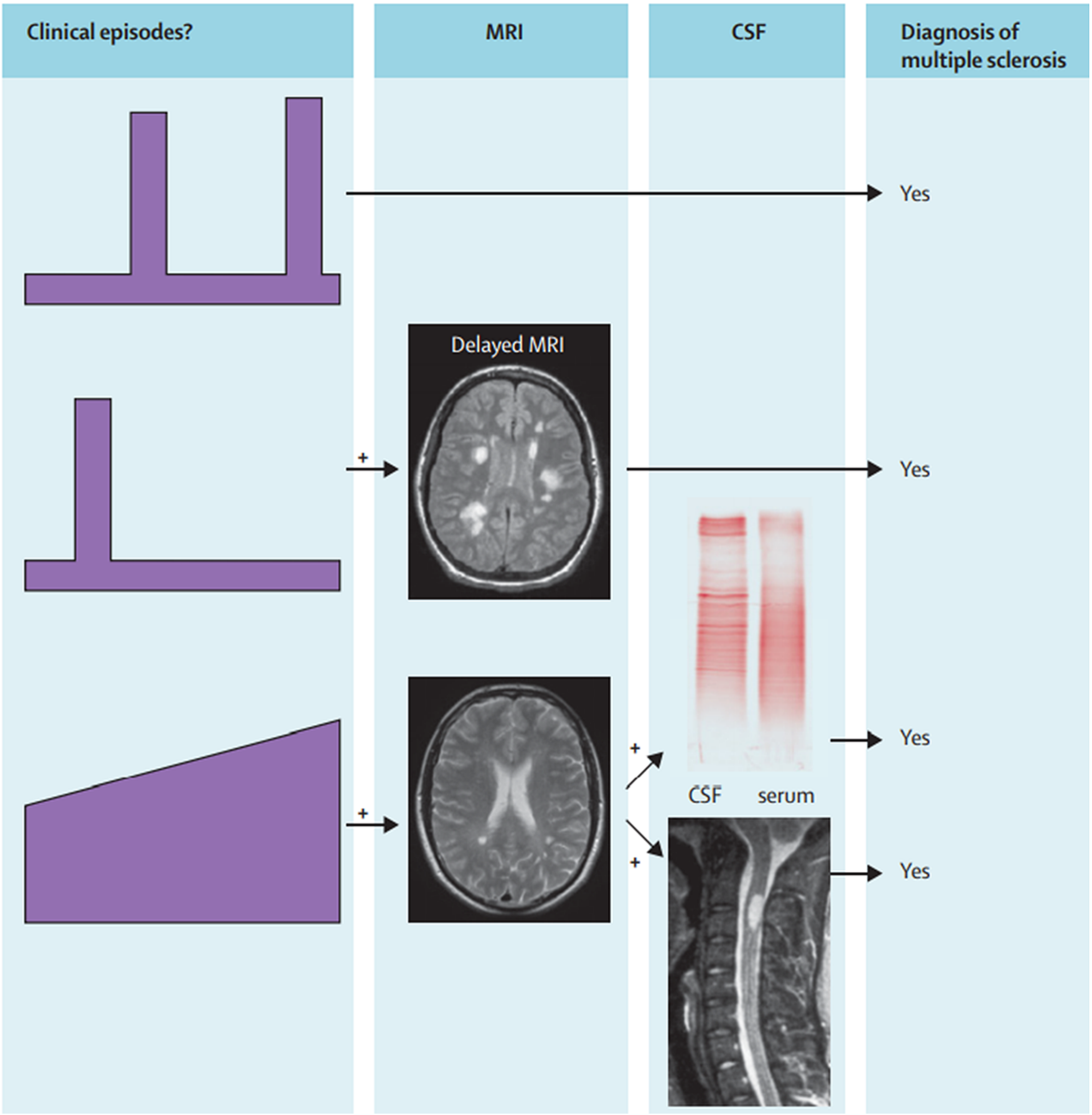

Figure 2: Criteria for the diagnosis of multiple sclerosis.
Modified from the McDonald criteria. The principle is to establish the dissemination in time and space of the lesions, particularly episodes affecting separate sites within the CNS occurring at least 30 days apart. It integrates clinical, imaging and laboratory data with the following conditions to be fulfilled: (i) Number of clinical episodes (left column). (ii) The number of lesions in distinct anatomical locations. MRI can substitute for one of these clinical episodes (middle left column). (iii) The presence of CSF oligoclonal IgG bands as dissemination in time. Primary progressive multiple sclerosis can be diagnosed after one year of a progressive deficit and two of (1) a positive brain MRI; (2) a positive spinal cord MRI; and (3) positive oligoclonal bands. Patients having an appropriate clinical presentation, but who do not meet all of the diagnostic criteria but cannot be attributed to other neurological disorder can be classified as having possible multiple sclerosis[4]. Figure reprint by permission of Elsevier, license number 4827840743650.

Clinically isolated syndrome (CIS), the monophasic episode of inflammatory demyelination in CNS, does not by itself meet the diagnostic criteria of MS but is considered as part of the MS phenotype and could potentially be the first attack followed by other episodes (also termed as relapses or exacerbations). Multiple relapses where symptoms disappear (termed remission) or that show remaining dysfunction with no apparent progression of the disease (partial recovery) will be diagnosed as relapsing-remitting multiple sclerosis (RRMS) and characterized as active or not active within a specified time frame (e.g. six months to 1 year). It is the most common course of disease affecting about 85% of the patients diagnosed. Most of them will subsequently transit to a more progressive form over time with the accumulation of neurological dysfunction or disability, termed secondary progressive multiple sclerosis (SPMS). Approximately 10% of MS patients have primary progressive MS, characterized by continually worsening of neurological function and accumulation of disability from the very onset, without initial relapses or remissions, but with fewer lesions and inflammation in the brain which make the diagnosis and treatment difficult. Progressive courses of MS have to be defined over a certain time, e.g. one year, with steadily increasing neurological dysfunction or disability without recovery. Whereas MRI lesion assessment has been widely established as a biomarker for relapses and disease activity in RRMS, no standardized imaging techniques have yet been established to precisely assess the disease progression since it does not present in a uniform fashion but with partly stable but also fluctuating phases[4,22-25].

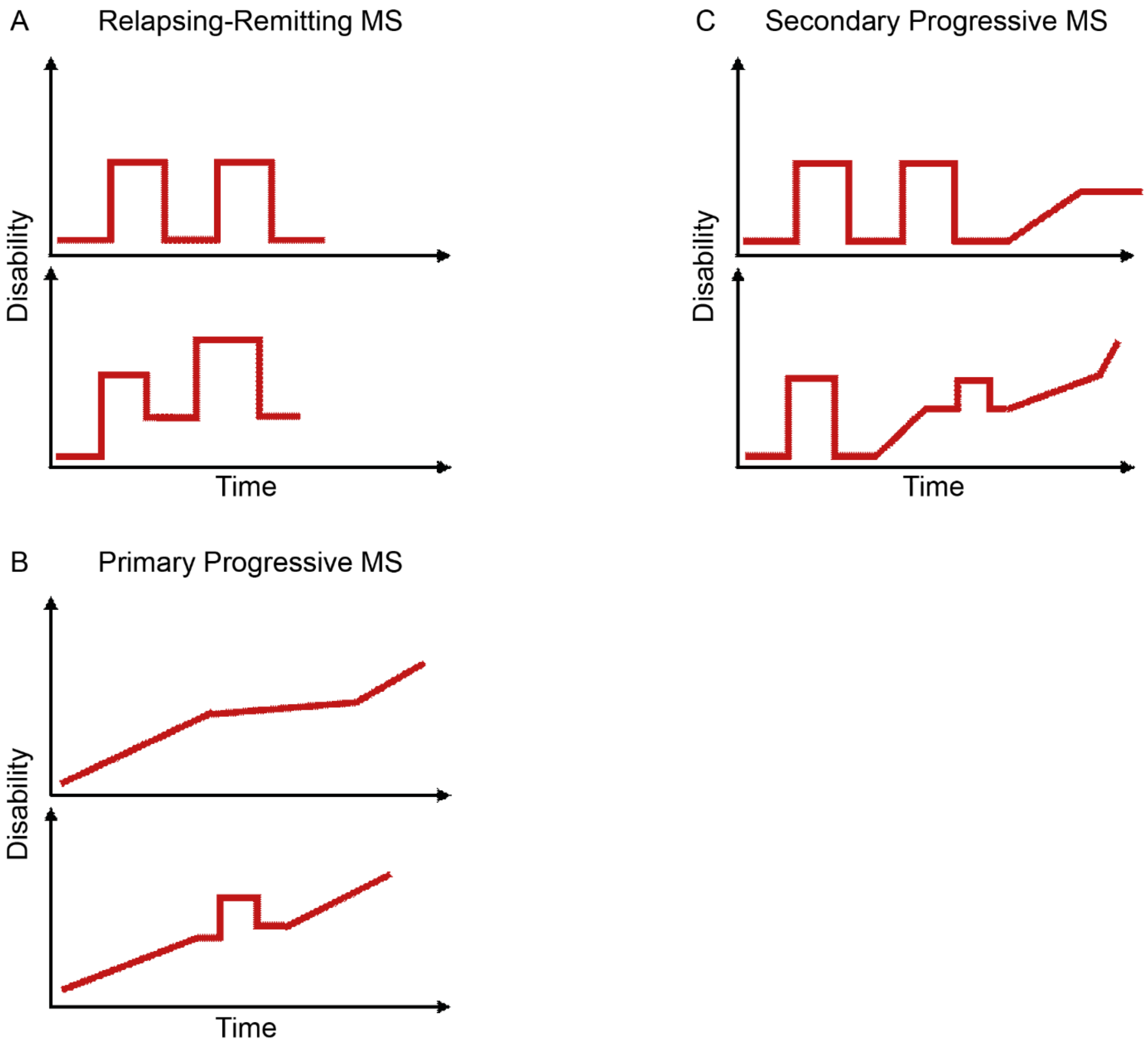

Figure 3: Types of MS
CIS followed by relapses with a complete or partial remission could develop different clinical courses. (A) A representative clinical course for RRMS, the first attack is followed by a relapse. Patients stay stable without any increase in neurological disability or recover completely or incompletely and therefore worsening the disability level. (B) Following RRMS, patients develop a constantly increasing disability over time, which is defined as SPMS. (C) Patients show a continuous worsening of neurological function from the onset of symptoms, without any features of prior remissions, which is defined as PPMS. (Image adapted from www.nationalmssociety.org)

1.1.3 Therapeutic options

Unfortunately, there is yet to be a cure available for MS. Current therapies are primarily aimed at reducing acute relapses, alleviating the severity of the attacks, modulating the disease or suppressing the immune system to slow the accumulation of neurological symptoms and disability. Therapeutic development has been substantially improving over the past 25 years[26] (Figure 4). Novel treatments with higher efficacy in reducing the intensity and frequency of relapses have emerged; however, present approved medications only have minor effects on the disability progression, especially if patients have already entered the phase of accumulating disability progression. Therefore, there is a need to understand further the underlying disease mechanisms, in particular, those resulting in neurodegeneration in order to develop better treatment options for progressive MS patients.

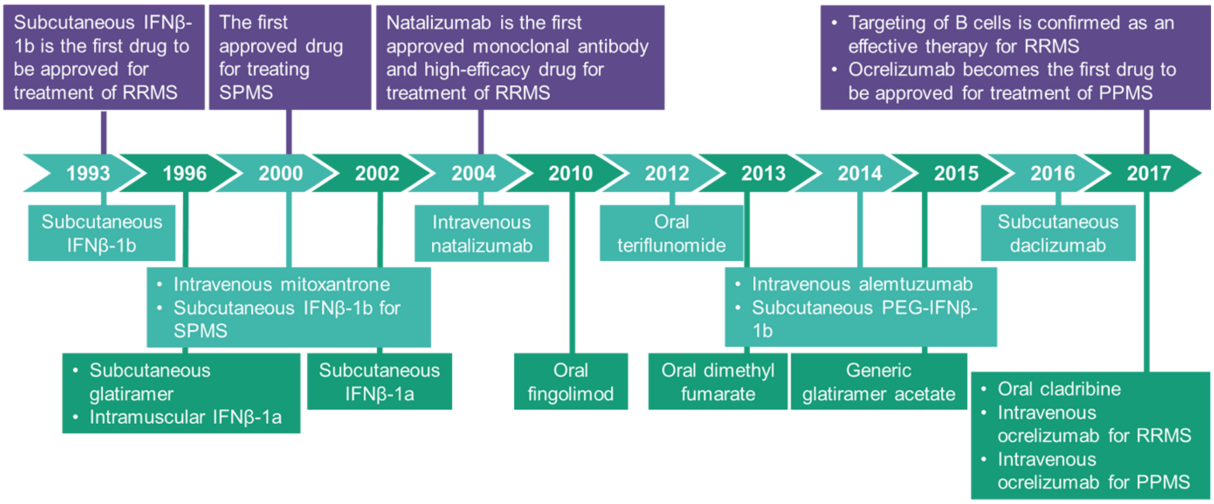

Figure 4: Timeline of developments in the treatment of multiple sclerosis.
Significant milestones in the development are shown in purple boxes, and drugs approved by the FDA (or the European Medicines Agency) are shown in green boxes. PEG, polyethylene glycol; PPMS, primary progressive MS; RRMS, relapsing-remitting multiple sclerosis; SPMS, secondary progressive MS. (Adapted from Tintore *et al.*, 2018)

Two different therapeutic strategies have been proposed to balance the efficacy, safety, and compliance of patients to the treatment regime: (a) the escalation strategy starts from moderately effective medications as the first line of response to mild to moderate relapsing-remitting disease (such as IFNβ 1b/a, GA, teriflunomide and dimethyl fumarate) and further adopts more aggressive therapies when disease activity progresses; (b) the induction approach, applied for highly active forms of the disease, suggests to start with strongly active therapeutics, like humanized monoclonal antibodies. Natalizumab, the first monoclonal antibody introduced to the market for treating RRMS, prevents lymphocytes from migrating across the blood-brain-barrier through binding to α-4 subunit of α4β1 integrin (very late antigen 4, VLA4), which is present on the surface of lymphocytes. It has an efficacy of reducing the annual relapse rate (aRR) by 70% [9]. Alemtuzumab, another option for aggressive MS and a monoclonal antibody against CD52, depletes circulating T and B lymphocytes[27,28] and reduces the aRR by 55% and disability worsening by 40%. The biggest concern for Alemtuzumab is the adverse effects, e.g. secondary autoimmunity, which requires thorough safety monitoring[29]. Also, the Natalizumab treatment induces a severe condition of progressive multifocal leukoencephalopathy, which requires extensive monitoring of the treated patients and therefore, higher treatment-related cost.

Elusive options for progressive MS pinpoint the obstacles, with a great amount of negative results from the clinical trials for both secondary progressive MS and primary progressive MS. Ocrelizumab, a CD20-binding antibody which has revealed a profound effect in the suppression of inflammation in RRMS patients with rapid onset efficacy of depletion of B cells[30], has been the first approved drug for treating primary progressive MS, alongside increasing evidence of the involvement of B cells in the pathogenesis of disease[31]. Fingolimod, the first-approved orally administered drug which is a sphingosine 1-phosphate analogue acting on S1P receptors, prevents T cells from leaving the secondary lymph organs. It results in about 50% reduction on aRR, one-third reduction on disability accumulation, and a significant improvement on MRI data[32]Siponimod has been approved for the treatment of secondary progressive MS. Although further studies are required for confirmation, other drugs like statins and ibudilast (a phosphodiesterase inhibitor) which have shown promising effects on the risk of disability, brain volume loss and T2 lesions volume might develop into further options for secondary progressive MS[33-35].

1.1.4 Pathology and pathogenesis

The histopathological hallmark of multiple sclerosis is the inflammatory plaque, which is characterized by immune cell infiltration, demyelination, reactive astrogliosis and neuronal loss (referred to as neurodegeneration). The latter is believed to be highly relevant to permanent clinical disability[9].

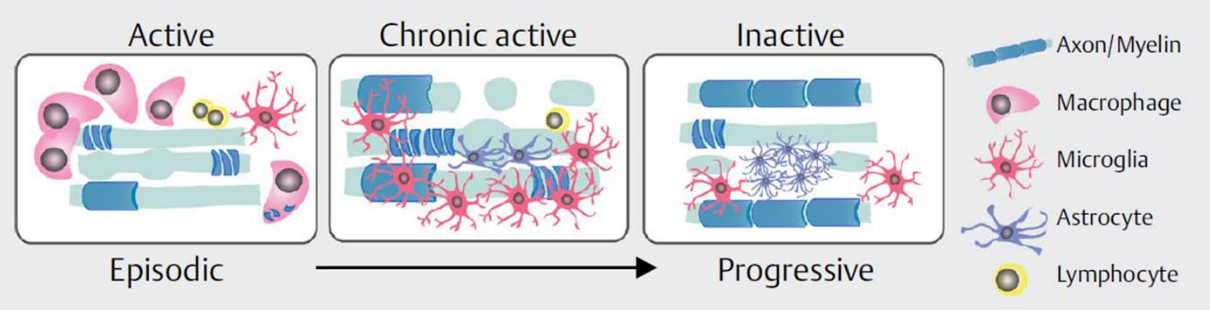

Figure 5: Transformation of typical lesion patterns in the course of multiple sclerosis[36]. Acute, chronic active and chronic inactive lesions are classified according to the inflammatory infiltration, demyelination, astrogliosis.

Active lesions with demyelinated axons, loss of oligodendrocytes and infiltration of macrophages occur predominantly in white matter during the relapsing-remitting phase of MS. $CD8^+$ T cells and $CD68^+$ macrophages accumulate in the core of the lesions together with the presence of perivascular cells, which mainly comprise of $CD4^+$T lymphocytes and to a lesser degree B lymphocytes. With the progression of the disease, in chronic active lesions, diffuse low-grade but a widespread accumulation of T cells and microglial activation occurs predominantly at the lesion borders (Figure 5). This pathology is defined as smoldering lesions[37] and primarily found in progressive MS patients. Most commonly, in aged patients with long-lasting progressive MS, inactive lesions evolve from chronic active lesions and represent a “burned out” status with gliotic appearance but no signs of active inflammation[38,39].

Immunopathogenesis

The initiation of immune responses to CNS autoantigens could be conceived in two scenarios based on in which compartments the autoantigen exposure occurs (Figure 6): (a) the CNS intrinsic hypothesis (inside-out model) states that the induction of the immune response is primarily activated by antigens released from the CNS. These can be a result of myelin and/or oligodendrocyte destruction and local microglial activation in so-called “prephagocytic” lesions, which subsequently leads to infiltration of immune cells from the pheriphery[40]. (b) The CNS extrinsic pathway (outside-in model) hypothesized that the autoimmune attack is initiated outside the CNS. The activated antigen presenting cells (APCs) present foreign antigens, which could be, for instance, from a neurotropic virus and lead to a molecular mimicry type reaction with priming of effector T-cells[41]. Subsequently, $CD4^+$ T cells are activated in the draining lymph nodes, migrate through the blood-brain barrier, and invade CNS parenchyma, where they trigger the formation of the inflammatory lesions [42,43].

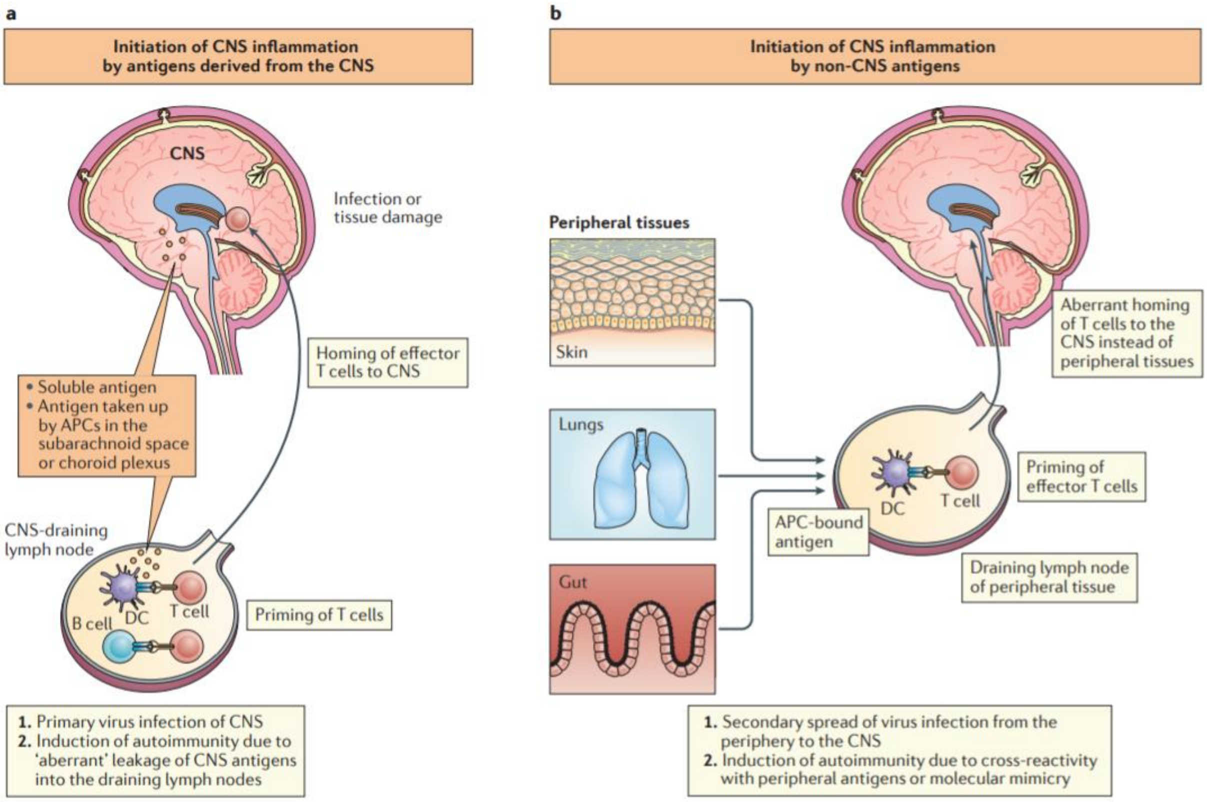

Figure 6: Models of autoimmune T-cell driven inflammation in the central nervous system. (A) Inside-out model: CNS inflammation resulting from adaptive immune responses against target CNS antigens is initiated in the CNS-draining lymph nodes. Self-antigens or foreign antigens expressed in the CNS are drained into the deep cervical lymph nodes either in a soluble form or via antigen-presenting cell (APC)-mediated delivery after uptake in the meningeal linings. After priming of antigen-specific T cells in the CNS-draining lymph nodes, these T cells home back to the CNS in order to eliminate foreign antigens or to cause autoimmune inflammation. (B) Outside-in model: T cells that recognize target antigens in the CNS can be primed by non-CNS antigens that are derived from peripheral sites. These antigens can be molecular mimics of CNS antigens or antigens that are produced by viruses that cause a systemic infection before infecting the CNS. DC, dendritic cell[43]. Figure reprint by permission of Springer Nature, license number 4827770079463.

Axonal pathology

Axonal dismantling occurs in many neurological diseases as a result of injury, genetic defects, toxins, metabolic disturbance, and inflammation. The extent of it in MS white matter likely correlates to the severity of inflammation, considered as a primary pathological hallmark. How exactly axonal pathology is caused and mediated in MS is still not fully known.

Focal axonal degeneration (FAD) has been unveiled to be a prominent pathological hallmark in experimental autoimmune encephalomyelitis (EAE), an animal model of multiple sclerosis. Three stages in respect of morphological alterations have been observed and defined: stage 0, myelinated axons which are morphologically intact; stage 1, in which the axons present focal swellings; and stage 2, considered as the late stage of FAD revealing the discontinuity of the axonal structure (Figure 7). Importantly, FAD can happen independently of demyelination.

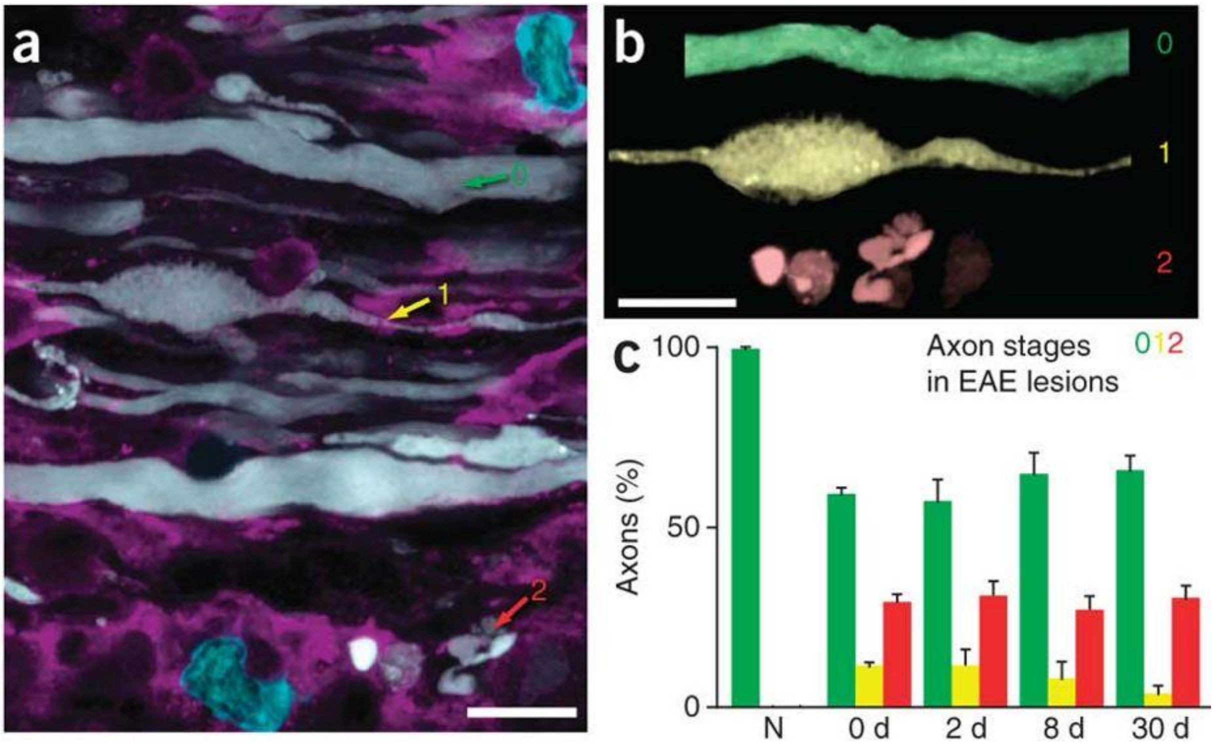

Figure 7: Focal axonal degeneration (FAD).
(A) Confocal projection showing axons (white), activated macrophages/microglia (magenta) and T cells (cyan) in an acute spinal EAE lesion. Some axons appear normal (stage 0), whereas others are swollen (stage 1) or fragmented (stage 2). (B) Pseudocoloured axons isolated from those shown in a: normal-appearing (0, green), swollen (1, yellow), and fragmented (2, red). (C) Frequency (in % ± s.e.m.) of axon stages in the normal spinal cord (N) and EAE lesions (0–30 d after EAE onset[1]. Figure reprint by permission of Springer Nature, license number 4827751067155.

Interestingly morphological alterations of mitochondria are present from the early stages of FAD onwards. It is believed that the damage of axons and possibly mitochondria are caused by the release of reactive oxygen- and nitrogen- species from activated microglia or macrophages. Interestingly, swollen stage 1 axons are shown to either fragment further or to be able to recover back to stage 0. As expected, small-calibre axons are more vulnerable to FAD. The fragmentation process is often initiated at the nodes of Ranvier and can concurrently occur at different positions of the same axon. Notably, the above mentioned morphological changes of axons can also be found in actively demyelinating lesions in MS patients[1].

Numerous factors are presumably important to the sequence of focal axonal degeneration in EAE and MS lesions but are not yet completely clarified. As mentioned above, one of them is reactive species released from mononuclear phagocytes, which has been demonstrated to induce a FAD-like axonal degeneration[1]. This is in accordance with the hypothesis that mitochondrial pathology due to oxidative burst might play an essential role in the pathogenesis of MS[44] which will be discussed in the following section (chapter 1.2.2). Another attribute is the early deficit of axonal transport in morphologically intact axons in EAE lesions. Redox scavenging ameliorates the transport deficits proving its interaction with reactive species[45].

When the disease progresses to the chronic phase, the long-lasting energy failure due to impaired mitochondrial energy production has been suggested to cause a state of virtual hypoxia in chronically demyelinated axons[46]. The underlying mechanisms behind this phenomenon might be a mismatch between energy supply and demand due to the redistribution of sodium channels in the demyelinated axons[47]. In general, high density (around 1,000 μm^{-2}) of sodium channels are assembled in the axonal membrane at the nodes of Ranvier, supporting saltatory conduction in myelinated axons in physiological conditions. The redistribution of ion channels within the demyelinated axon increases the need for energy, further overflows the ATP-producing capacity of mitochondria. Voltage-gated Na^+ channels (Nav) are reorganized to be an important role in axonal degeneration in MS[48]. Especially Nav1.2 channels, one of the most predominant isoforms in CNS, are dispersedly present along the axons[49]. In addition, Na^+/K^+ ATPase is synergistically upregulated to restore Na^+ concentration, a step which requires extra energy. When the amount of energy need surpasses the ATP-producing capacity, sodium can no longer be sufficiently removed by the Na^+/K^+ ATPase, which results in an increased cytoplasmic sodium concentration. The accumulation of cytoplasmic sodium reverses the directionality of the sodium-calcium exchanger (NCLX). It leads to elevated intracellular calcium that can be further augmented by the release of calcium from mitochondria[49].

1.1.5 Animal model: Experimental autoimmune encephalomyelitis (EAE)

Experimental autoimmune encephalomyelitis (EAE) was first introduced and described by Rivers *et al*., in 1933, to study the pathogenesis of post-vaccinal encephalomyelitis in monkeys, which were injected with emulsions and extracts of normal rabbit brains[50,51]. Refined models have been developed to understand autoimmune-mediated pathology, which displays inflammatory and demyelinating processes of the CNS. Due to its clinical and pathological similarities to MS, they are often used to investigate disease development and its specific histopathological characteristics, and to dissect mechanisms of potential therapeutic interventions. There are, however, limitations of translating animal studies to human disease because of fundamental differences: First, the required external immunization. Second, the fact that the induced antigens are known in EAE but not in MS. Third, the fact that the majority of lesions is found predominantly in spinal cord axons with intact cerebrum. Thus, the selection of an appropriate model to be used will strictly depend on the specific scientific questions being addressed and result in which type of immunization method will be needed as well as which animal species and strain has to be chosen [52].

There are two main methods for EAE induction: (a) actively-induced EAE, by immunization with CNS tissue or myelin peptides such as myelin basic protein (MBP), myelin oligodendrocyte glycoprotein (MOG) or proteolipid protein (PLP) in combination with complete Freund's adjuvants (CFA), which contains inactivated mycobacteria tuberculosis and mineral oil[53,54]. This has been shown to produce a high incidence of disease in specific strains[55] with the consequence of white matter inflammation and motor dysfunction. In C57BL/6 mice injected with MOG, the onset of the disease typically occurs 9 to 12 days after immunization [56]. (b) Passively-induced or adoptive-transfer EAE (AT-EAE) was first demonstrated by transferring lymph node cells isolated from rats that were previously immunized with spinal cord homogenate into naïve animals. This method was refined afterwards by transferring MHC class II-restricted T cells after inferring that CD4+ T lymphocytes mediate the disease. It is a model widely used in drug screening, functional gene characterization[57] and to investigate the particular roles and functions of different T-cell subtypes in the pathogenesis of diseases[58].

1.2 Mitochondria

1.2.1 The basic characteristics of mitochondria

Mitochondria are double-layer organelles located in the cytoplasm that are present in almost all eukaryotic cells. Their size ranges from 0.5 to 10 μm. As the powerhouse of cells, mitochondria generate large quantities of adenosine triphosphate (ATP), the usable form of energy along with free reactive radicals such as reactive nitrogen species or reactive oxygen species. Apart from producing energy, mitochondria participate in a wide range of cellular events, for instance, in maintaining the calcium homeostasis which is crucial for multiple signalling pathways as well as stress responses; in regulating cell growth and adaptation by biosynthesis of macromolecules and hormones, protein modification and nuclear-mitochondrial communication; in mediating redox production, which as well involves in the cell signalling; in initiating programmed cell death through release of cytochrome c and in conciliating the formation of mitochondrial permeability transition pore (mPTP)[18].

Speaking of the structure of mitochondria, compared to the outer membrane of mitochondria (OMM) which allows ions and small molecules to permeate through pore-forming membrane proteins freely (e.g. voltage-dependent anion channel, VDAC), the inner membrane (IMM) is tightly regulated. Ions or molecules can only traverse with the aid of specific membrane transport proteins (e.g. mitochondrial calcium uniporter, MCU). As a result of high selectivity, inner membrane potential builds up to 180 mV. It accounts for the overall mitochondrial membrane potential ($\Delta\Psi m$), which is an indicator of the energy capacity that affects ATP synthesis. As the location where oxidative phosphorylation (OXPHOS) takes place, the IMM is folded and compartmentalized with a roughly 5 times more extensive area, a feature referred to as cristae. The matrix contains the deoxyribonucleic acid (DNA) of the mitochondrial genome (mtDNA) with 37 genes (in humans) encoding for two rRNAs, 22 tRNAs and 13 polypeptides[59]. All 13 mitochondrial protein products are involved in the composition of the electron transport chain (ETC) as well as the proteins necessary for tricarboxylic acid (TCA) cycle, which metabolizes pyruvate to intermediates for further energy production[60,61].

As above mentioned, mitochondria also serve as a calcium sensor and reservoir. Mitochondrial Ca^{2+} uptake and efflux were known to be determined by different pathways[62], but both aim at balancing cytosolic Ca^{2+} concentration and therefore can affect the metabolic processes in the cytoplasm. The entry of calcium to mitochondria relies on the cytosolic calcium concentration and is selectively transported to the matrix of mitochondria by mitochondrial calcium transporter (MCU) which allows rapid intramitochondrial calcium accumulation. Another membrane protein, voltage dependent-anion channel (VDAC) which locates on the outer membrane of mitochondria, is permeable to calcium and mediates the transport of calcium from the cytosol to the inner membrane space or vice versa[63-65]. The homeostasis of calcium is particularly critical to certain cell types, such as neurons. Data from our group has shown that calcium influx to intracellular compartments is sufficient to damage the mitochondria in a laser axotomy model[66]. In the same study, chelating Ca^{2+} with ethylene glycol-bis(β-aminoethyl ether)-N', N', N', N'-tetraacetic acid (EGTA) dramatically abolished the upsurge in calcium, preventing mitochondria from being damaged.

1.2.2 Mitochondrial and axonal dysfunction in MS

1.2.2.1 Mitochondria as the primary sources of cellular energy

As above described, energy supply from mitochondria is of significant importance for a wide variety of cellular functions.

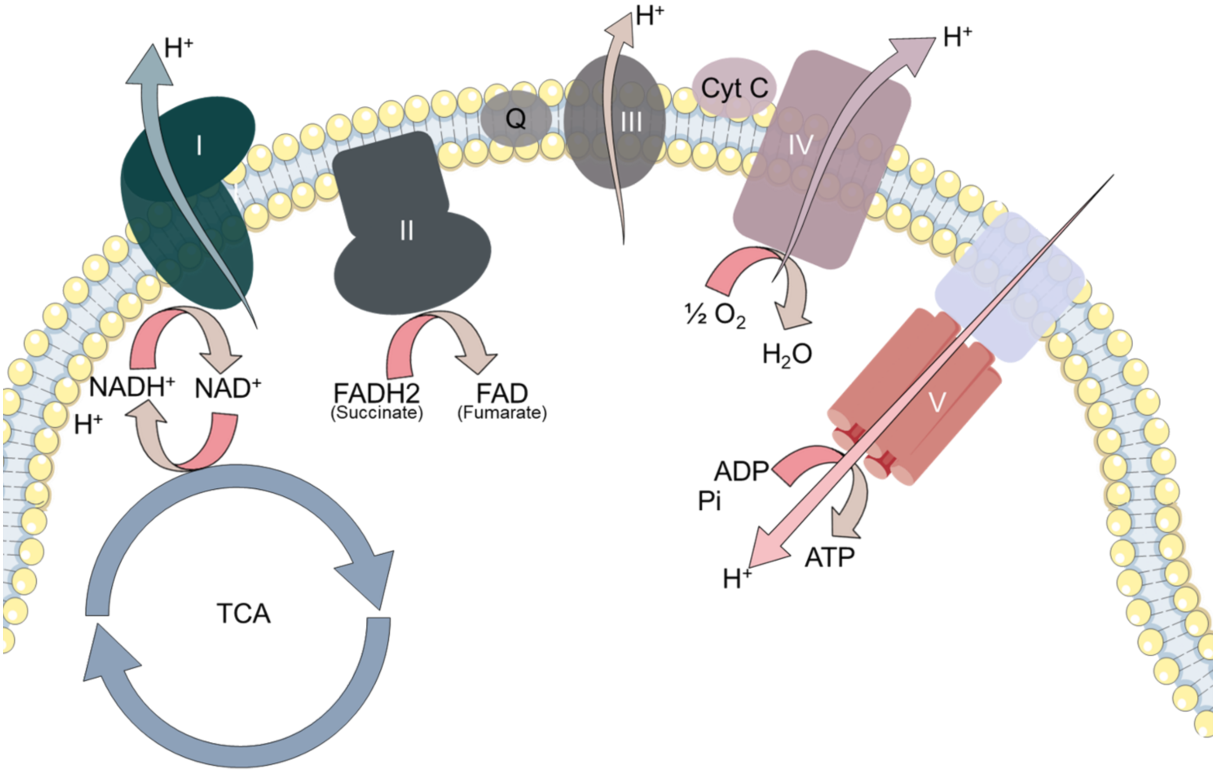

Figure 8: The diagram of the mitochondrial electron transport chain (ETC).
ETC comprises complex I, complex II, complex III, complex IV, and complex V (ATP synthase). NADH as an intermediate derived from the tricarboxylic acid cycle (TCA cycle) are fed to the ETC to generate proton gradient in the intermembrane space across the inner membrane which is further used for the ATP synthesis at complex V. Complex I and complex III are the main sites for the formation of superoxide ($O2^{\cdot-}$).

The oxidative phosphorylation (OXPHOS) process of ATP synthesis in mitochondria starts with the flow of electrons through the respiratory chain complexes, a series of membrane-bound proteins, from NADH to oxygen and conserves the energy which is further converted to ATP. The intermediate ions, H^+, flow across the membrane based on the electrical potential differences together with the ATP production. In addition to generating ATP, mitochondria are the major intracellular sites for producing free radicals as by-products during OXPHOS[67] (Figure 8). Accumulated reactive species which are not adequately scavenged will induce a subsequent process that eventually damages the cells. Deleterious consequences are thus likely to result from defective mitochondrial metabolism, especially in high energy-dependent cell populations like neurons[68].

1.2.2.2 Mitochondrial defects and MS

Energy failure can have a severe impact on axons that need to uphold a delicate metabolic balance for saltatory conduction. It is an extremely energy-intensive process, which makes neurons particularly dependent and vulnerable to the energy supply. The number, the morphology, and the distribution of mitochondria within a cell mainly correspond to its need for energy[69,70]. As an example, within myelinated axons, the morphology of mitochondria in terms of length and volume as well as their moving velocity are not homogeneous, highly depending on their cellular location and the changes in calcium level and energy demand[71].

In the active demyelinating inflammatory lesions, impaired axonal mitochondria have been identified as a critical component involved in the mechanisms of white matter pathology. The substantial loss of cytochrome c oxidase-I activity and complex IV highlights the pathological participation of mitochondria in MS[72]. Interestingly, a compensatory upregulation of mitochondrial mass and respiratory complex activity, especially complex IV which is responsible for a critical step of ATP production, was seen in intact and more than half of the demyelinated axons in inactive lesions[73,74] instead of a complete loss of function (Figure 9).

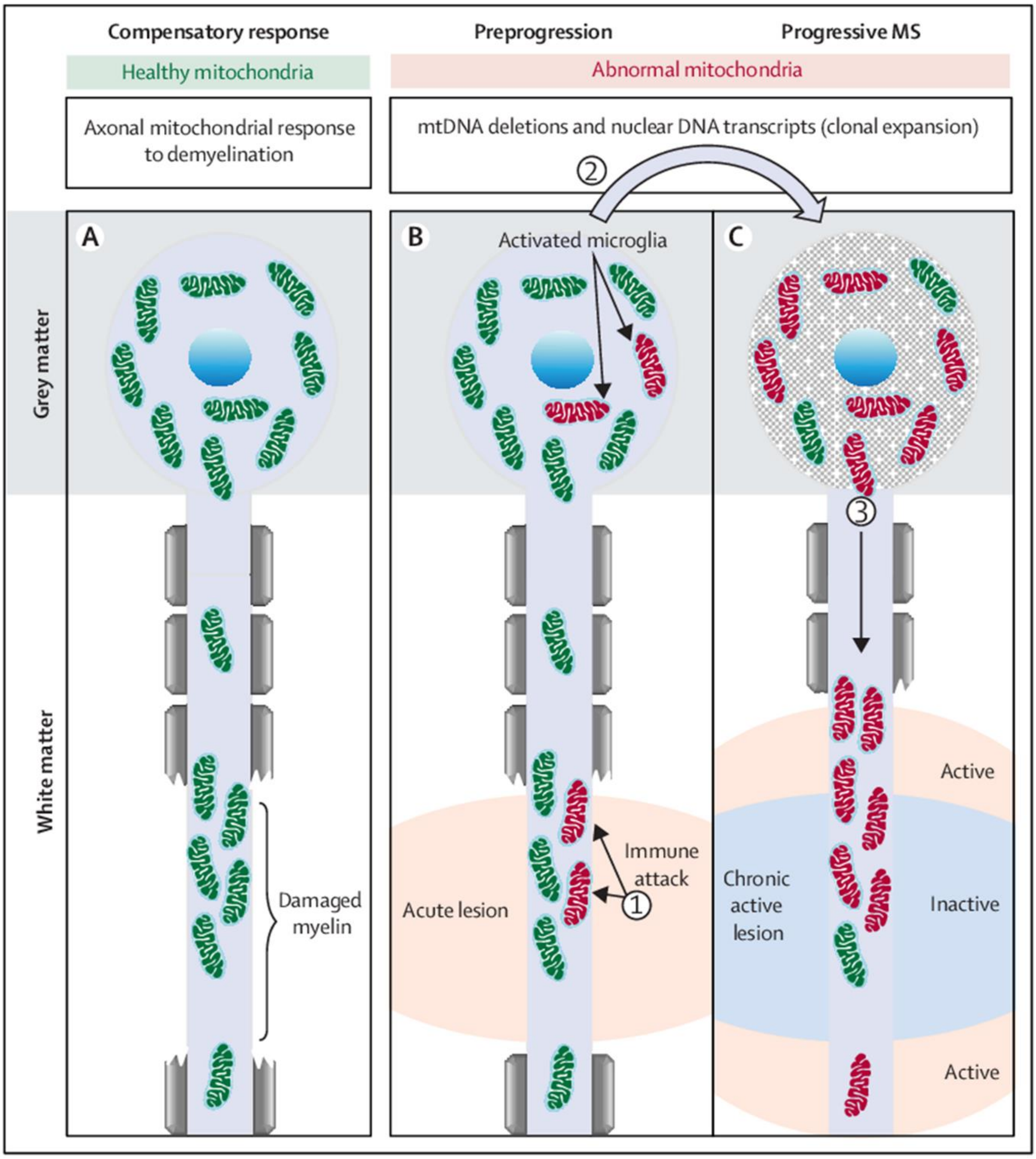

Figure 9: A three-step hypothesis: formation (A), amplification (B), and displacement (C) for the role of mitochondria in axon degeneration in progressive multiple sclerosis.

(A) Functional mitochondria gather upon non-autoimmune demyelination of wild-type neurons *in vivo* and the demyelinated axon in multiple sclerosis. The mitochondrial changes including increased number, size, activity, and speed of movement of mitochondria are reported as the “axonal mitochondrial response to demyelination”. (B) During the preprogression of multiple sclerosis, inflammatory products injure mitochondria in several cell types, including neurons within the lesions, resulting in mitochondrial cytochrome c oxidase-1 dysfunction and subsequent energy deficiency. Additionally, oxidative injury of DNA leads to the formation of mtDNA deletions in both the white matter (1) and grey matter (2). (C) The resulting biochemical deficiency of the mitochondrial respiratory chain complexes or enzymes in neuron acts as a reservoir of abnormal mitochondria, which then undergo aberrant displacement to the demyelinated axon and further cause energy failure accompanied by increased reactive oxygen species production in the axon (3). Figure reprint by permission of Elsevier, license number 4847160287690.

As the active demyelination proceeds to chronically active lesions with continuous inflammation at the lesion edge in progressive stage, mitochondrial damages such as disrupted respiratory chain complexes and mitochondrial DNA (mtDNA) also occur in the grey matter[48,75] (Figure 9). The injured mitochondria which are no longer functional then cause energy failure and concomitantly increase reactive species production[31] which might lead to a vicious consequence followed by the axonal degeneration and cell death when the damages surpass a certain threshold[76].

1.3 Intravital imaging

With the ever-changing development of microscopy, scientists nowadays are able to crack the details of neurophysiology and neuropathology in cellular or even subcellular structures by utilizing two-photon excitation microscopy, which allows observing changes with high spatial and temporal resolution *in vivo*. In contrast to the conventional light microscopy with linear absorption processes that cause light scattering due to the inhomogeneity of the tissue and limit the penetration of the light at the superficial layer within 100 µm, two-photon excitation has a greater imaging-depth up to 1 mm. To solve the problems that limit the resolution, confocal has a sharp optical section in z-axis by narrowing down the depth of field through a pinhole that excludes the light which does not originate from the focal plane. The serial acquisition is taken plane by plane. However, it is more susceptible to photodamage as the absorption above or below the focal plane is not blocked, which is a limitation for *in vivo* time-lapse imaging.

The improvement of tissue penetration arises from the principle of using the simultaneous absorption of two lower-energy photons with longer wavelengths at the near-infrared range, each of which contributes one half of the total energy required to excite a fluorophore[77,78]. Ultrashort pulsed lasers and high-numerical-aperture (N.A.) lenses are necessary for reaching the high excitation efficiency at the focal plane with high spatial resolution. The probability of two photons interacting with samples (fluorophores) at the focus is increased as the photon density is greater when approaching the focal plane[78,79]. The excitation of fluorophores is restricted to only a single focal point, strictly defined in the x, y and z positions where the energy is highest to decrease the photobleaching phenomenon and phototoxicity (Figure 10).

The properties mentioned above explain the differences when compared to single-photon microscopy.

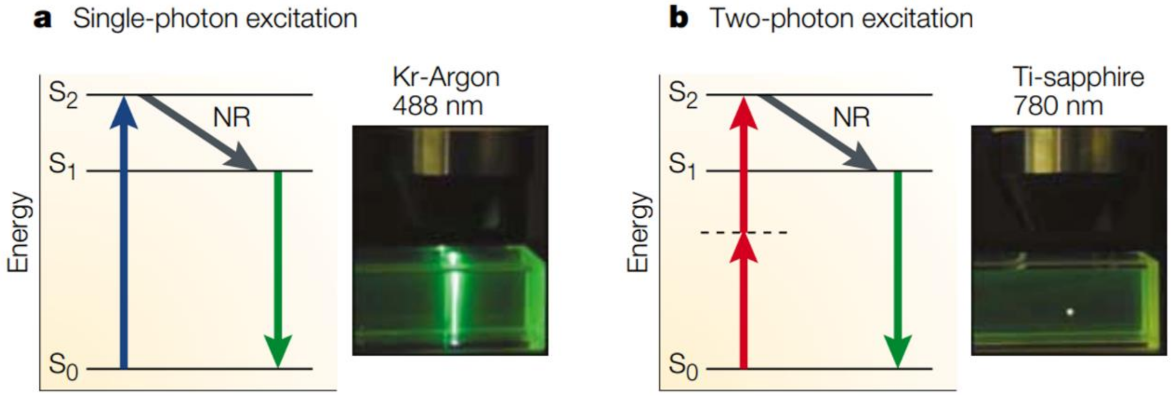

Figure 10: Principles of confocal and two-photon microscopy.
(A) Single-photon excitation. Individual photons of high-energy blue light (wavelength, λ = 488 nm) from a krypton-argon (Kr-Argon) laser excite fluorophores in the sample. After an electron in the fluorophore jumps from the ground state of energy (S_0) to the excited state (S_2) (indicated in blue arrow), it loses energy rapidly owing to non-radiative relaxation (grey arrow, NR). Subsequently, fluorescence emission occurs at a longer wavelength than the excitation light (Stokes shift) as the electron falls back to the ground state (green arrow). As excitation involves single photons, fluorescence is emitted along the whole path of a laser beam focused on a sample of fluorescent dye. (B) Two-photon excitation. Two infrared photons (λ = 780 nm) from a pulsed titanium-sapphire (Ti-sapphire) laser are absorbed simultaneously (red arrows) to excite the fluorophore; light is emitted in the same manner as for single-photon excitation (green arrow). However, light is emitted only at the focal point of the focused laser beam due to the quadratic relationship between excitation intensity and fluorescence emission[77]. Figure reprint by permission of Springer Nature, license number 4831880286495.

1.3.1 Intravital 2-photon microscopy of the nervous system

In vivo imaging has emerged as an important tool for investigating the biological events in both healthy and diseased tissue contexts. In addition to the advances of the imaging modalities as above mentioned, the generation of transgenic animals with fluorescent labels in defined cell populations such as neurons and glia has been helpful for understanding how cells behave and communicate in physiological and pathological conditions[80,81]. Among these, neurons are exceptionally interesting targets in the CNS. In order to identify the neuronal somata and processes, different variants of fluorescent proteins ("X"FPs) are expressed under the control of a Thy1-promoter element[82], making a significant advance for intravital observation in the nervous system. Subcellular compartments can be imaged by attaching biosensors to membrane proteins or expressing them behind specific organelle targeting sequences, which allow functional readouts based on intracellular molecules or ions. These can give an idea about mitochondrial dynamics and transport[45,83], microtubule dynamics[84], pH and redox state[66,85,86], mitochondrial redox signals[66], et cetera.

The improvement of *in vivo* microscopy together with the invention of a diverse biosensor toolset make it possible to access details of the nervous system, which so far have been obscure to research.

1.3.2 Genetically encoded fluorescent biosensors

These bio-engineered sensors now enable us to monitor cellular processes such as ion transport, metabolites, physiological and disease processes in real-time with high temporal and spatial resolution.

1.3.2.1 Redox sensor: Grx1-roGFP

Redox-sensitive green fluorescent proteins (roGFP) were initially developed through substituting two cysteine residues in the purlieu of the chromophore in the beta-barrel of GFP, which renders the probe ratiometric[87,88]. It has been widely used to measure the redox potential in different subcellular compartments such as mitochondria, endoplasmic reticulum and cytosol[85,89].

A particular variant, roGFP2, was used to establish an enzyme-coupling sensor: the cysteine residues engineered at the amino acid positions 147 and 204 with an additional mutation at position 65 (S147C/Q204C/S65T). These mutations make roGFP2 preferentially interact with glutaredoxins instead of thioredoxins. This coupling strategy improves the specificity of the sensor to the designated substrate: glutathione (GSH). It facilitates real-time equilibration as oxidation of Grx1-roGFP2 by GSSG happens 100,000 times faster as compared to uncoupled roGFP2[85].

Moreover, ratiometric measurements with roGFPs are reported to be insensitive to pH changes in the physiological conditions ranged from 5.5 to 8.5 as compared to cpYFP-based (cpYFP and Hyper) redox probes[85,90].

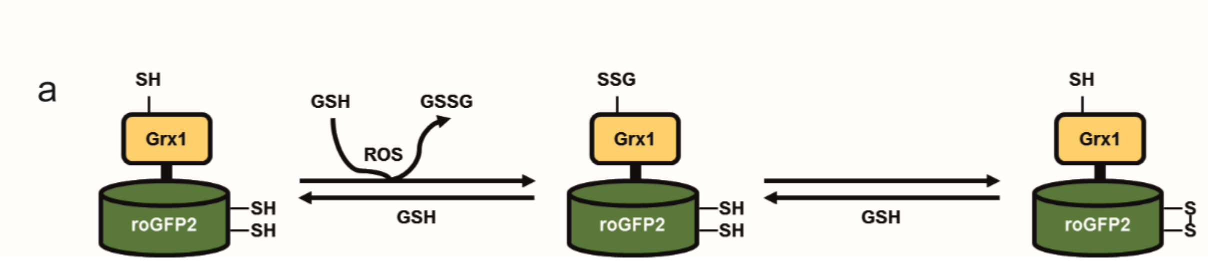

Figure 11: Grx1-roGFP2 indicator.
Modification of roGFP2 in combination with human glutaredoxin 1 (Grx1) substantially improved specificity to detect the glutathione redox potential and the rate of thiol-disulfide exchange between roGFP2 dithiol and 2GSH/GSSG couple (Adapted from Gutscher *et al.*, 2008)

1.3.2.2 Calcium sensor

Calcium is a crucial regulator responsible for various functions in a variety of cell types. Peculiarly, in the nervous system, it regulates membrane polarization and the action potential of neurons, therefore, is critical for neuronal activity. The optical prerequisites for identifying calcium signals *in vivo* have been developed over the past years, including suitable sensors to detect robust calcium baseline and transient signals with enough sensitivity and stability. The sensors should interfere neither with intracellular ion homeostasis nor with endogenous calcium signalling.

Different calcium indicators are described below, including (A) bioluminescent calcium-binding proteins, (B) chemical calcium indicator, (C) FRET-based genetically encoded calcium indicators (GECI) and (D) single-fluorophore GECI[91].

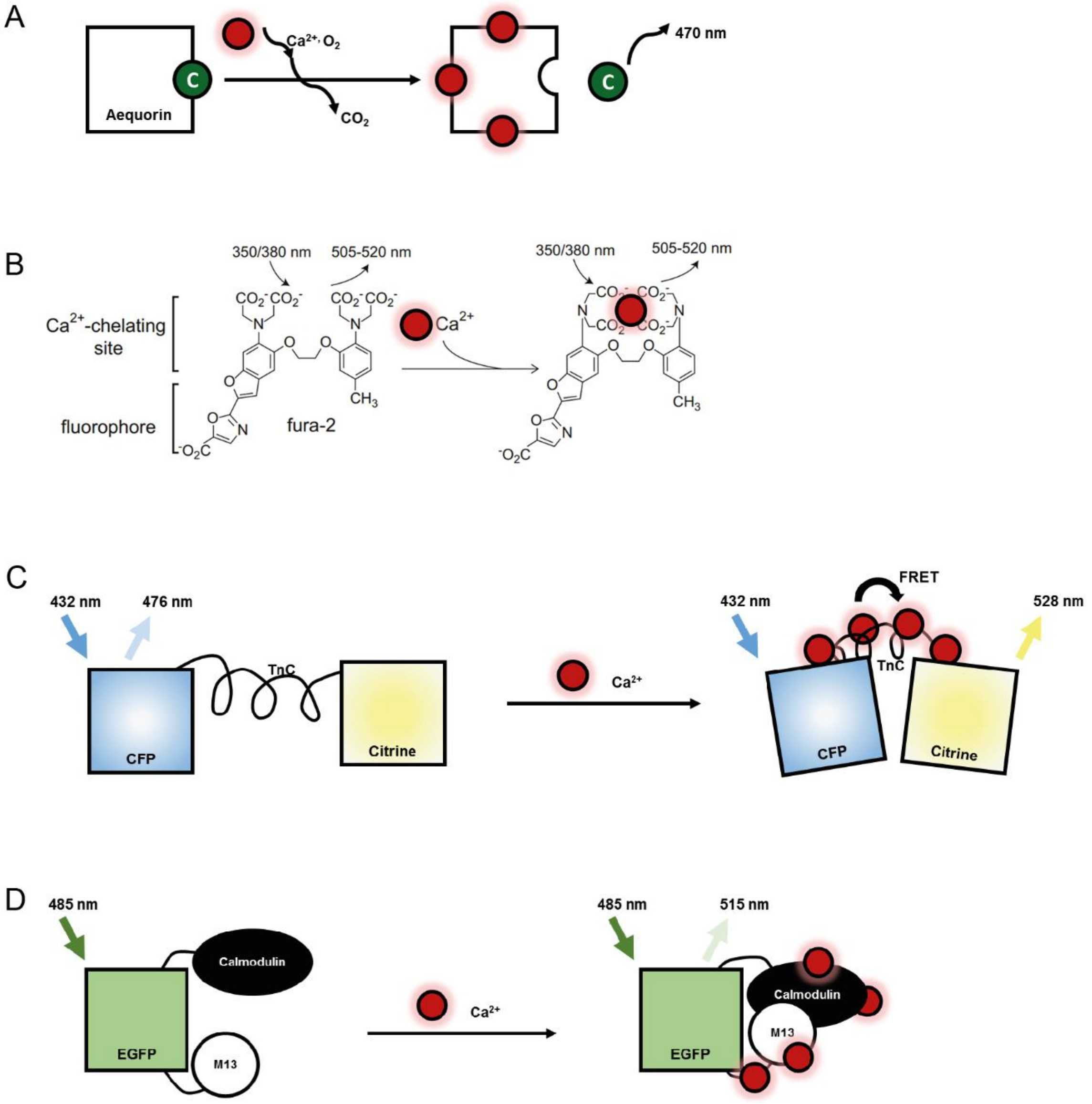

Figure 12: Calcium indicators.
(A) Bioluminescent protein. (B) Chemical calcium indicator. (C) FRET-based genetically encoded calcium indicator (GECI). (D) Single fluorophore genetically encoded calcium indicator (GECI) (adapted from Grienberger & Konnerth., 2012).

In the case of bioluminescent calcium-binding proteins, attachment of calcium to binding sites of bioluminescent proteins (e.g. aequorin) leads to a conformational change of the indicators and, as a consequence, oxidation of the prosthetic group coelenterazine to colenteramide with the emission at around 470 nm due to the relaxation of coelenteramide from an excited to its ground state (Figure 12A).

Fura-2 is an example of a fluorescent chemical (or synthetic) calcium indicator. It can be excited by ultraviolet light at around 350-380 nm and upon the binding of calcium, which further causes an intramolecular conformational change, increases emission between 505 and 520 nm (Figure 12B). These indicators have to be introduced into the cell at great expense and are therefore only of limited use[91].

In a further fundamental development, the coupling of calcium-binding proteins such as calmodulin and troponin to fluorescent proteins, for instance, GFP additionally could be expressed in a cell type-specific manner. Accordingly, two important types of genetically encoded calcium indicators (GECIs) were established: FRET-based GECI, a dual sensor system based on nonradiative energy transfer (Foerster resonance energy transfer) between a donor and an acceptor fluorophore that occurs in the distance within 10 nm and allows ratiometric measurements of intracellular calcium concentration[92]. An essential feature for the occurrence of FRET is the spectral overlap: the emission spectrum of the donor with shorter wavelength overlaps with the excitation of the acceptor fluorophore which displays a longer wavelength[93], generating a nanoscale ruler to visualize the conformational change. When Ca^{2+} binds to the calcium-binding motif, conformational changes in the structure brings the two fluorophores closer[94]. The ratio of the two fluorophores' signal is used as the read-out to quantify the calcium level (Figure 12C).

Instead of two fluorophores, a single fluorophore can be used on the basis of the indicator altering its signal intensity upon binding. The GCaMP family is widely in use as it has high signal-to-noise, dynamic range and response kinetics, however, a lack of reference baseline makes it unreliable in pathological conditions besides non-linear responses of the sensor to calcium (Figure 12D).

1.3.2.3 ATP sensor:

(a) Perceval and PercevalHR:

The Perceval family comprises genetically encoded biosensors of cellular ATP-to-ADP ratios that are a fusion protein comprising GlnK1 and a modified GFP. GlnK1 is a bacterial protein, member of the nitrogen regulatory protein (PII) family, involved in the synthesis of glutamine. It consists of three loops, which have nucleotide-binding sites, that bind either to ATP or ADP and thus induces a conformational change of its T-loop. The presence of Mg-ATP makes it highly compact while its absence favours a more flexible conformation. Binding of ADP or ATP alone does not cause T-loop closure[95,96].

To transfigure the structural change of Glnk1 into a fluorescent signal readout, a circularly permuted Fluorescent Protein (cpFP) was inserted into the T-loop of GlnK1, in between Tyr51 and Ile52, reported to be a high-affinity site for ATP as compared with ADP. Binding of each nucleotide generates a change in fluorescence of roughly 3-fold and 1.4-fold, respectively. Competitive binding makes it practical for ratiometric measurement. Instead of detecting the absolute concentration of ATP or ADP, it indicates the relative level of ATP-to-ADP. However, the low reaction rate constant (K_R) of 0.2 of the original construct QV5 diminishes the use of the sensor to detect the change under physiological condition. An optimized version named Perceval was then created which has faster kinetics with a K_R of 0.5 while maintaining the original properties of QV5.

For more widespread use of the sensor in mammalian cells, a further upgraded sensor - Perceval High Range (Perceval HR) (Figure 13A), was established accordingly. It senses the ATP-to-ADP ratio with a K_R of 3.5, which is seven times larger than its predecessor Perceval. Its ratio ranges from 0.4 to 40, making it suitable to sense the higher ATP concentration found in mammalian cells. Additionally, it shows two distinct excitation peaks which respond depending on which of the nucleotides is binding. The binding of ATP or ADP to the sensors increases the fluorescence at 500 or 420 nm, respectively. The ratio of these two wavelengths indicates the occupancy of PercevalHR by the different nucleotides[97-99]. Under physiological conditions, the sensors with high nucleotide affinities (n_H value ~ 1) are usually fully occupied either with ATP or ADP as the cytosolic concentrations of ATP and ADP are ranged within the hundreds of µM and several mM, respectively[99]. Since it is a competitive binding system, a spectral ratio of fluorescent signals is given instead of the absolute values, eliminating the possibility of misreading a difference in fluorescence driven by an artefact of different levels of sensor expression. The baseline and the change of signal are described to be independent of the total amount of sensor protein. Still, it has been correlated with the glucose supply, proving that the PercevalHR can be used to measure ATP-to-ADP fluctuations in a physiological context.

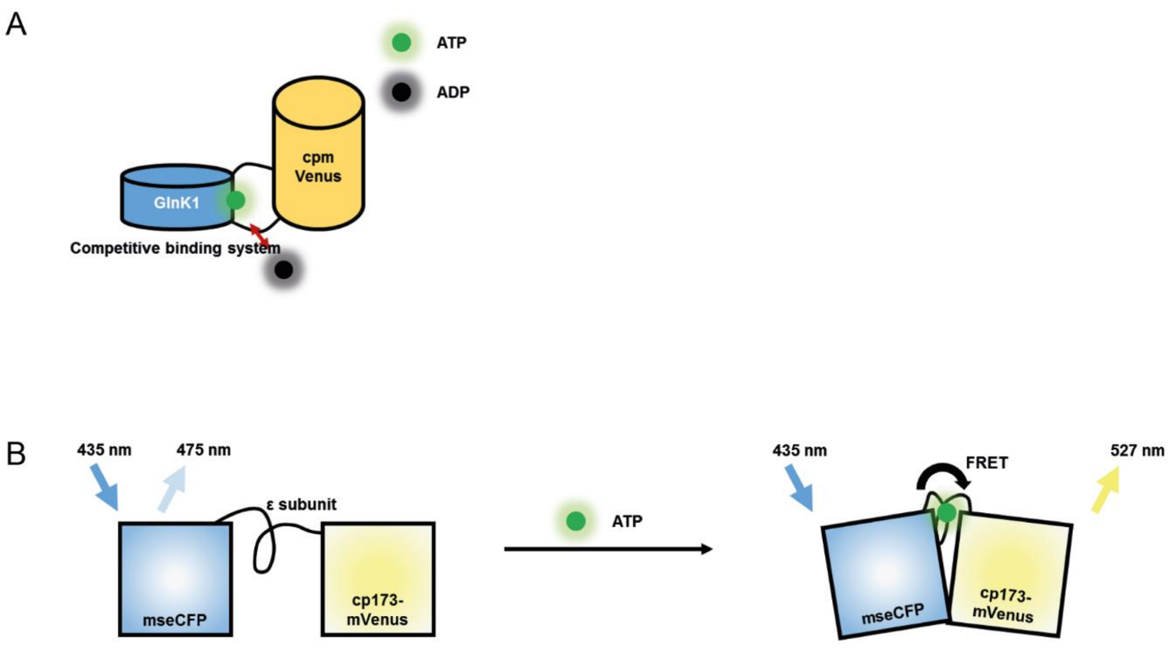

Figure 13: ATP sensors.
(A) PercevalHR sensor. Diagram of PercevalHR ATP: ADP sensing, Glnk1 is connected to CFP (mseCFP) with a competitive binding site which binds to either ATP or ADP[99]. (B) ATeam ATP sensor. Variants of CFP (mseCFP) and YFP (cp173-mVenus) are connected by the ε subunit of Bacillus subtilis F_0F_1-ATP synthase. In the absence of ATP (left), the extended and flexible conformation of the ε subunit separate the two fluorescent proteins, resulting in low FRET efficiency. In the presence of ATP (right), the ε subunit retracts to bring the fluorescent proteins closer, which increases FRET efficiency (adapted from Imamura *et al*., 2009).

(b) ATeam:

ATeam is a FRET-based ATP biosensor which was previously generated and implemented to measure ATP levels in HeLa and yeast cells[100,101,102]. It comprises mseCFP (a variant of CFP), mVenus (a variant of YFP) and an ATP sensing domain (ε subunit of F_0F_1-ATP synthase) (Figure 13B). The YFP-to-CFP emission ratio (527 nm/475 nm) is used as a readout for an estimation of the ATP concentration. An optimized version, AT1.03NL, has been reported to be suitable for assessing the ATP level at low temperature in *Drosophila melanogaster* and *Caenorhabditis elegans.*

(c) Quantitative evaluator of cellular energy (QUEEN):

A single fluorescent protein-based ATP sensor was used to measure the absolute ATP level. It comprises cpEGFP and an ATP sensing domain (ε subunit of F_0F_1-ATP synthase). Different variants have been designed for diverse applications. For instance, QUEEN-7μ shows high affinity for ATP in comparison to QUEEN-NA which has no affinity for ATP and can be used as a control. The ratio of the emission peaks taken from 2 distinct excitation wavelengths demonstrates the ATP level.

(d) iATPSnFRs:

A single fluorescent protein-based and single wavelength-based ATP sensor, iATPsnFRs comprises a fluorescent protein (circularly permuted-superfolded GFP, cpSFGFP) and the ε subunit of F_0F_1-ATP synthase which has been adapted to the aforementioned sensors. Unlike QUEEN, iATPSnFRs shows single wavelength-based behaviour with a narrow spectral bandwidth, which makes the sensors suitable for imaging experiments in combination with other sensors. In addition to intracellular ATP measurements, iATPSnFRs can sense cell surface ATP even though the extracellular ATP level is physiologically low, ranging from nanomolar to millimolar due to the hydrolysis of ATP by ectoATPases.

2. Experimental aims

Focal axonal degeneration (FAD) has been characterized as a novel form of axonal degeneration and represents a sequential process with the potential to recover in the early stages[1]. The subcellular and molecular mechanisms that induce FAD are only incompletely understood. Previous work suggests that mitochondria and their damage could be crucial contributors to the FAD process: Nikic *et al*. illustrated the presence of mitochondrial injury from the early phase of focal axonal degeneration (FAD) in both experimental and human neuroinflammatory lesions. Furthermore, they could show that inducing mitochondrial dysfunction with CCCP (a mitochondrial uncoupler) in healthy animals, axonal and mitochondrial pathology could be generated that resembled observations in MS models and patients[48,72,74].

In this thesis, we aimed to decipher how characteristics and consequences of mitochondrial pathology in neuroinflammatory lesions by answering the following questions with advanced two-photon microscopy techniques, biomolecular sensor, and targeted genetic manipulations in an animal model of MS:

(1) At what stage of the axon degeneration process are axonal energy deficits detected in acute and chronic neuroinflammatory lesions?

(2) At what stage of the axon degeneration process in neuroinflammatory lesions do we observe alterations of mitochondrial redox homeostasis and do they contribute to mitochondrial and axonal pathology?

(3) At what stage of the axon degeneration process in neuroinflammatory lesions do we observe alterations of mitochondrial calcium handling and do they contribute to mitochondrial and axonal pathology?

(4) How is the mitochondrial proteome changed in neuroinflammatory lesions, and can these alterations contribute to axonal energy deficits and degeneration?

3. Material and methods

3.1 Material

3.1.1 Surgery

Reagents and chemicals

Agarose	Sigma-Aldrich Chemie GmbH, Taufkirchen, Germany
Antagonist	
Revertor (5mg, atipamezole hydrochloride)	CP-pharma GmbH, Burgdorf, Germany
Naloxon (0.4mg, naloxone hydrochloride)	B.Braun AG, Melsungen, Germany
Flumazenil (0.1mg)	Hameln GmbH, Hameln, Germany
Bephanthen Augen – und Nasensalbe 5g (eye ointment)	Bayer AG, Leverkusen, Germany
Braunovidon Salbe 10% (Povidon iod)	B.Braun AG, Melsungen, Germany
Cutasept F Loesung 250 mL (disinfectant spray)	Bode Chemie GmbH & Co, Hamburg, Germany
Ethanol 70%	CLN GmbH, Niederhummel, Germany
Forene (Isoflurane)	CP-pharma GmbH, Burgdorf, Germany
Ketamine hydrochloride 10% (Ketamine)	Bela-Pharm GmbH, Vechta, Germany
MMF	
Fentanyl (0.05mg)	B.Braun AG, Melsungen, Germany
Midazolam (5mg)	Ratiopharm GmbH, Ulm, Germany
Cepetor (1mg, medetomidine hydrochloride)	CP-pharma GmbH, Burgdorf, Germany
Artificial mouse cerebrospinal fluid (aCSF)	
Solution A:	
8.66 g NaCl	Merck, Darmstadt, Germany
0.224 g KCl	Merck, Darmstadt, Germany
0.206 g $CaCl_2 \cdot 2H_2O$	Sigma-Aldrich Chemie GmbH, Taufkirchen, Germany
0.163 g $MgCl_2 \cdot 6H_2O$	
Solution B:	
0.214 g $Na_2HPO_4 \cdot {}_7H2O$	Merck, Darmstadt, Germany

0.027 g $NaH_2PO_4 \cdot H_2O$ d$H_2$0 ad 500 ml	Merck, Darmstadt, Germany
Xylariem 20 mg (Xylazine)	Serumwerk Bernburg AG, Bernburg, Germany
Tools and materials	
BD Plastipak Hypodermic luer slip syringe 1 ml	Becton, Dickinson&Co, Franklin Lakes, USA
Noyes Spring Scissors (Large spring scissors)	Fine Science Tools GmbH, Heidelberg, Germany
Vannas-Tübingen Spring Scissors (Small angled spring scissors)	
Dumont Mini Forceps – Inox Style 3 (Small forceps)	
Dumont Mini Forceps – Inox Style 5 (Small forceps, smaller tip than Inox style 3)	
Hypodermic Needles BD Microlance 3 30 Gauge (0.3 mm, yellow)	Becton, Dickinson&Co, Franklin Lakes, USA
Hypodermic Needles BD Microlance 3 23 Gauge (0.6 mm, blue)	
Ethicon Ethilon monofilament 6-0 size, 667H (superficial suture)	Johnson&Johnson Medical GmbH, Norderstedt, Germany
Sugi (absorbent triangles)	Kettenbach GmbH&Co KG, Eschenburg, Germany
Technical devices	
Olympus KL 1500 LCD (cold light source for stereomicroscopy)	Olympus Deutschland GmbH, Hamburg, Germany (Headquarter in Japan)
Olympus Stereo Microscope SZ51	
FST 250 Hot Bead Sterilizer (sterilizer for surgical instruments)	Fine Science Tools GmbH, Heidelberg, Germany
T/Pump (Heating pad)	Gaymar Industries, NY, USA Foredom Electric Co. Connecticut, USA

Spinal clamping device (spinal adaptor for a stereotaxic frame)	Narishige Inc., NY, USA
Small animal ventilator	Harvard apparatus Ltd, Cambridge, USA
Intratracheal cannula (1.0mm OD, 13 mm length)	

3.1.2 EAE induction

Reagents

Purified recombinant myelin oligodendrocyte glycoprotein (MOG, from *E. Coli*)	Stock solution, produced by AG Kerschensteiner
M. tuberculosis H37 RA	Sigma-Aldrich Chemie GmbH, Taufkirchen, Germany
Incomplete Freund Adjuvant (IFA)	
Pertussistoxin (PTX), from Bordetella pertussis, inactivated	
Tools and materials	
Hamilton 10 ml syringes	Hamilton
Hypodermic Needles BD Microlance 3 23 Gauge (0,6 mm, blue)	Becton, Dickinson&Co, Franklin Lakes, USA

3.1.3 Perfusion and immunohistochemistry

Reagents

PFA (paraformaldehyde), 4% in 1x PBS pH 7.4	Morphisto GmbH, Frankfurt a.M, Germany
Sucrose (30%)	Sigma-Aldrich Chemie GmbH, Taufkirchen, Germany
Sodium azide (0.1% in 1x PBS)	Sigma-Aldrich Chemie GmbH, Taufkirchen, Germany
Heparin-Natrium 25.000IE (Heparin sodium)	Ratiopharm GmbH, Ulm, Germany
10x PBS (phosphate buffered saline) pH 7.4	Sigma-Aldrich Chemie GmbH, Taufkirchen, Germany
Triton X-100	Invitrogen GmbH, Darmstadt, Germany

Tween20	
Tissue-Tek O.C.T (Cryoprotection)	Sakura Fintek Ltd, Tokyo, Japan
Vectashield Mounting Medium	Vector Laboratories Inc, Burlingame, USA
Antigen retrieval reagents: (1) Sodium Citrate Buffer (10mM Sodium Citrate, 0.05% Tween 20, pH 6.0) (2) EDTA Buffer (1mM EDTA, 0.05% Tween 20, pH 8.0) (3) Tris-EDTA Buffer (10mM Tris Base, 1mM EDTA Solution, 0.05% Tween 20, pH 9.0) (4) Tris-Buffer (10mM Tris Base, 0.05% Tween 20, pH 10)	Sigma-Aldrich Chemie GmbH, Taufkirchen, Germany
Blocking solution Fetal bovine serum (FBS) Gelatin from cold water fish skin Bovine serum albumin (BSA)	ThermoFisher Scientific, Waltham, USA Merck, Darmstadt, Germany Sigma-Aldrich Chemie GmbH, Taufkirchen, Germany
Antibodies and tracers	
Primary antibody RFP Idh3a Idh2 Mdh2 CS COX6a1 Pdp1 SLC16a1 Suclg2 SHDC	Novus Biologicals, Colorado, USA
Ndufv3 COX4i1	Abcam, Cambridge, United Kingdom

	Abgent, California, United States
Secondary antibody Goat-anti-rabbit AlexaFluor 488 Goat-anti-rabbit AlexaFluor 594 Goat-anti-rabbit AlexaFluor 647 Goat-anti-mouse AlexaFluor 488 Goat-anti-mouse AlexaFluor 594 Goat-anti-mouse AlexaFluor 647 Goat-anti-chicken AlexaFluor 488	Invitrogen GmbH, Darmstadt, Germany
Tracer DAPI NeuroTrace 640/660 fluorescent Nissl	Invitrogen GmbH, Darmstadt, Germany
Materials, tools and devices	
Microscope slides 76x26 mm	Gerhard Menzel Glasbearbeitungswerk GmbH, Braunschweig, Germany
Microscope cover slips 24x60 mm	
Tissue Tek Cryomold Standard, 25×20×5 mm	Agar Scientific, Essex, United Kingdom
Tissue Tek Cryomold Biopsy, 10×10×5 mm	
12-well cell culture plates	Becton, Dickinson and Company, Franklin Lakes, USA
24-well cell culture plates	
48-well cell culture plates	
Leica CM1850 cryostat	Leica Microsystems GmbH, Wetzlar, Germany
Vibratome 1000Plus	Leica Microsystems GmbH, Wetzlar, Germany

3.1.4 Viral labelling strategy

Virus

AAV-hSyn:eGFP-ires-Cre AAV-hSyn:Cre AAV-hSyn:GFP	University of Pennsylvania Vector Core, Philadelphia, USA

AAV-hSyn: eGFP-Cre AAV-CMV: CAG-FLEX	& produced in house (AG Kerschensteiner)
Virus production	
Chemicals	
Polyethylenimine (PEI) 1mg/mL, pH 7.0	Sigma-Aldrich Chemie GmbH, Taufkirchen, Germany
Polyethylene glycol (PEG) 8000 40% pH7.4	
Benzonase	
Iodixanol 60%	
Phenol Red	
Buffers	
NaCl/PBS-MK 1M (filtered) • 5.84 g NaCl • 0.0263 g $MgCl_2$ • 0.01491 g KCl add PBS 1x 100mL PBS-MK 1M (filtered) • 0.0263 g $MgCl_2$ • 0.01491 g KCl add PBS 1x 100mL	Sigma-Aldrich Chemie GmbH, Taufkirchen, Germany
100x Pluronic F-68 • Stock A – 0.1% P-F68 • Stock B – 0.01% P-F68 • Stock C – 0.001% P-F68 + NaCl 200mM	Invitrogen GmbH, Darmstadt, Germany
Formulation Buffer: Pluronic-F68 0.001% Lysis buffer pH 8.5 NaCl 150mM Tris-HCl 50mM	Sigma-Aldrich Chemie GmbH, Taufkirchen, Germany
Cell culture	

Dulbecco’s Modified Eagle Medium (DMEM)	Invitrogen GmbH, Darmstadt, Germany
Advanced Roswell Park Memorial Institute (aRPMI) Transfection Medium	
Fetal Bovine Serum (FBS)	
Penicillin/Streptomycin 10.000U	Sigma-Aldrich Chemie GmbH, Taufkirchen, Germany
HEK-293 cells	Provided by M.Goetz (AG Goetz), BMC, Munich
Plasmid pAD-Helper AAV-Capsid 9	University of Pennsylvania, Philadelphia, USA
DNA extraction Qiagen Plasmid Maxi Kit #12165	Qiagen GmbH, Hilden, Germany
Materials	
Membrane filters 0.22 µm	Merck Millipore, Darmstadt, Germany
Membrane filters 0.45 µm	
Conical tubes 50 mL	ThermoFisher Scientific, Waltham, USA
Petri-dish plates Ø15cm	
Quick-Seal polypropylene tube	Beckman Coulter Inc, Brea, USA
Hypodermic Needle-Pro 18G	B.Braun AG, Melsungen, Germany
Amicon Ultra Centrifugal filter	Merck Millipore, Darmstadt, Germany
Devices	
Heraeus Multifuge XCR	ThermoFisher Scientific, Waltham, USA
Optima L-90K UltraCentrifuge	Beckman Coulter Inc, Brea, USA

3.1.5 Imaging

Microscopes and objectives

Manual XY translation stage	Custom build, parts by Thorlabs Inc Newton (New Jersey), USA
FV1000 confocal system mounted on an upright BX61 microscope	Olympus Deutschland GmbH, Hamburg, Germany

10/0.4 water immersion objective x20/0.85 oil immersion objective x60/1.42 oil immersion objective	(Headquarter: Shinjuku City, Tokyo, Japan)
FV1000 MPE multiphoton microscope x25/1.05 water immersion objective Femtosecond pulsed Ti:Sapphire laser	
FV 1200 MPE-RS multiphoton microscope x25/1.05 water immersion objective Femtosecond-pulsed Ti:Sapphire laser	
MaiTai HP Titanium:sapphire laser	Newport/ Spectraphysics, Irvine, California, USA
Mai Tai HP-DS(eHP) Titanium:sapphire laser	

3.1.6 Software

Adobe Creative Suite CS6 (Photoshop, Illustrator)	Adobe Systems, Inc., San Jose, California, USA
ImageJ/ FIJI	General Public License http://rsbweb.nih.gov/ij/download.html
Graphpad Prism	GraphPad Software, La Jolla, California, USA
Microsoft Office (Powerpoint, Excel, Word)	Microsoft Corporation, Redmond, Washington, USA

3.2 Methods

Animals

All animals were bred and housed in our animal facilities under standard conditions with a maximum of 5 mice per cage and a 12-hours light/12-hours dark cycle. Food and water for mice were provided ad libitum. Female and male were equally distributed into control and experimental groups. All experimental procedures involving animals and their care were carried out in accordance with regulations of the relevant animal welfare acts and protocols approved by the respective regulatory office (Regierung von Oberbayern).

Cloning of transgenic constructs and generation of transgenic mouse lines

The Perceval GW1-HR plasmid was purchased from Addgene. The blunt end cloning strategy we adopted in short: GW1-Perceval-HR plasmid was digested with Xba1 and EcoRI enzymes, inserted into the Thy 1- vector cut beforehand with XhoI and dephosphorylated. Ligation and electroporation procedures were followed by minipreps of positively ampicillin selected E. coli cultures and advanced verifications of the correct plasmid orientation and enzyme digestions. The construct was transfected in HEK cells, and cytoplasmic expression was observed by live imaging at the confocal microscope. Maxipreps of the adequate cloning candidates were then carried out using Qiagen kits, and Thy1-Perceval-HR plasmid was linearized using PvuI and EcoRI restrictions enzymes.

The plasmid Twitch2B-pcDNA3 was kindly provided by Dr. Oliver Griesbeck (Max Planck Institute of Neurobiology, Martinsried, Germany). Twitch2b sensor was extracted using NotI restriction enzyme and inserted into the pCMV-myc-mito plasmid (Addgene) cut beforehand with NotI restriction enzyme and dephosphorylated. Positive cloning candidates of the Twitch 2b sensor targeted to mitochondria were then transfected in HEK-293 cells to verify expression in the right location and their toxicities. In brief, the medium of the cells was changed to calcium magnesium-free HBBS before performing live imaging at the confocal microscope. The functionality of the calcium sensor was tested with chemicals to identify the response of the sensors to the increased and decreased calcium level. After retesting the construct and its functional responsiveness by chemical application in HEK cells culture, maxipreps of the adequate cloning candidates were carried out using Qiagen kits, and the pCMV-myc-mito-Tw2b sequence was extracted using PmI and XbaI, blunted and inserted into the Thy 1- vector cut beforehand with XhoI, blunted and dephosphorylated. The Thy 1- mito-Twitch2b plasmid was linearized using ZraI and AflIII restrictions enzymes.

Sequencing of Thy 1- mito-Twitch2b and Thy1-Perceval-HR constructs were performed by Eurofins Scientific. The sample purity of the linearized DNA was determined using the ratio of absorbance at 260 nm and 280 nm. The concentration of the linearized DNA used for pronuclear injections was 45.2 ng/ul in 60 ul for Thy1-Perceval-HR (with a ratio A260/280 at 1.83) and 36.5 ng/ul in 120 ul (with a ratio A260/280 at 1.83) for Thy 1- mito-Twitch2b. The generation of the transgenic lines was conducted at the transgene facility of the Max Planck Institute for Molecular Cell Biology and Genetics in Dresden by standard pronuclear injections into pseudo-pregnant host mice.

Virus production and neonatal injection

The AAV-hSyn: DIO-GFP plasmid was initially incubated with SalI and XhoI at 37℃ for 1 hr to remove DIO-GFP, followed by incubating with BglII enzyme at 37℃ for another 1 hr to open the cut. GFP-ires-Cre fragment was cut from AAV-CMV-GFP-ires-Cre with BglII enzyme. Restriction ligation was performed with Quick Ligase (NEB) according to the manufacture's instruction. From AAV-hSyn: GFP-ires-Cre, GFP-ires was excised with BmgBI and the backbone was ligated with Quick Ligase to acquire AAV-hSyn: Cre plasmid. Construct with correct oriented insert was introduced to Stellar Competent cells (Takara Bio) and incubated overnight at 37˚C. Plasmid purification was further performed with Qiagen Plasmid Maxi Kit accordingly to the manufacturer's protocol.

AAV vector packaging was performed using human embryonic kidney 293 (HEK 293) cells. In general, HEK 293 cells were transfected with pAD-Helper, AAV-Capsid 9 and AAV-Construct (molar ratio 3:2:5 or 1:1:1) by RPMI: PEI incubation protocol. AAV vector was harvested from the supernatant with polyethylene glycol (PEG) solution and the cell pellets. Freeze-thaw cycles were performed to lyse the cells and residual DNA from the packaging was degraded by applying benzonase. Vectors were purified with iodixanol gradient procedure, concentrated by subsequent centrifugation and incubation with formulation buffer (Pluronic-F68 0.001% in saline PBS). The product was then further collected and stored in small aliquots in -80˚C. 3 µl of diluted AAV (genomic titer ~10^{12}) with 0.05% trypan blue was loaded into the injection syringe held by the stereotaxic manipulator. The naïve pups were anaesthetized with isoflurane and gently placed at the stage paralleled to the line between lambda and bregma. The ultrasonic machine was used to aim to the right ventricle.

Induction of experimental autoimmune encephalitis (EAE)

Adult animals were immunized subcutaneously with 250 µl of an emulsion containing 200 µg of purified recombinant MOG (N1-125) in complete Freund's adjuvant (containing 650 µg Mycobacterium tuberculosis; H37 RA, Sigma-Aldrich). The mice received intraperitoneal (i.p.) injections with 200 ng pertussis toxin at day 0 and 2. After immunization, mice were weighed daily, and neurological deficits were evaluated according to the following EAE score: 0, no clinical signs; 0.5, partial tail weakness; 1, tail paralysis; 1.5, gait instability or impaired righting ability; 2, hind limb paresis; 2.5, hind limb paresis with dragging of one foot; 3, total hind limb paralysis; 3.5, hind limb paralysis and forelimb paresis; 4, hind limb and forelimb paralysis; 5, death. The "onset" of disease was defined by the first day of neurological symptoms; "peak" as 2–3 days following clinical onset and "remission" as 7 days following the onset of EAE.

Surgery procedure

Mice were imaged at the peak of acute EAE (only animals with an EAE score ≥ 2.5 were included) and onset plus 22 days. For this purpose, mice were anaesthetized with medetomidine (0.5 mg/kg), midazolam (5.0 mg/kg), and fentanyl (0.05 mg/kg), placed on a heating pad, and then tracheotomized and intubated to minimize breathing when necessary. The dorsal spinal cord was surgically exposed as previously described[1]. In brief, the skin was disinfected and incised along the spinal column, the dorsal spinal cord was surgically exposed by performing a laminectomy and the opening was constantly superfused with artificial cerebrospinal fluid (aCSF). The vertebral column was then position-fixed on a spinal clamping device (Narishige STS-a) allowing controlled movement in x, y, z directions during the imaging session. A 3.5% agarose well was built up around the spinal opening and filled with aCSF. During the imaging sessions, animals were kept under constant anaesthesia, and their breathing and reflexes were controlled every 30 min.

In vivo imaging and images analysis

A BX61WI upright microscope (Olympus) with motorized nosepiece focus-drive, together with a custom-built, manual stage (Z deck from Prior) or a motorized in vivo bridge (Luigs-Neumann) was used. Mice were then imaged using Olympus FV1000 MPE or Olympus FV1200 resonant scanner equipped with a spectrally tunable Ti:sapphire laser (Spectra Physics/Newport) emitting femtosecond pulses of near-infrared light with a maximum power of 30mW at the back focal plane and a 25x/1.25 water-immersion objective (Olympus).

For experiments involving Thy 1- mito-Twitch2b × Thy 1-OFP3 mice, excitation wavelengths of 750 nm were applied to reveal axonal labelling and 840 nm for the calcium sensor. The latter in combination with emission filter systems collecting between 500-540 nm for the Cerulean channel and between 520-560 nm for eYFP or FRET channel. The two corresponding detectors used were non-descanned detector photomultiplier tubes (PMTs, Hamamatsu) and gallium arsenide phosphide (GaAsP).

For experiments involving Thy 1-PercevalHR mice, excitation wavelengths of 950 nm and 840 nm were applied. Emission signals were collected simultaneously with two photomultiplier tubes (Hamamatsu H7422) together with a 525/50 nm band-pass filter. Iodoacetic acid (IAA) 10 mM and Carbonyl cyanide m-chlorophenyl hydrazone (CCCP) 100 µM final concentration were added to the imaging solution aCSF for obtaining the baseline. Images were acquired using Olympus Fluoview 1000 or 1200 software.

Images were analyzed with FIJI (optimized ImageJ, http://fiji.sc/Fiji). Background intensities were measured and subtracted for every axon in every experiment to create a background mask, and pixel-by-pixel ratio was calculated from the mean over three regions of the same axon. For representative images, maximum intensity projections of image stacks were gamma-adjusted and processed with a despeckle filter using Photoshop software (Adobe).

Mitochondrial isolation

Mitochondrial isolated samples for mass spectrometry were obtained from 6- to 8-week-old male mice. Mito*Tag* mice and wild-type mice were anaesthetized with isoflurane and transcardially perfused with heparin in PBS. The lumbar spinal cord was dissected, weighed and homogenized with a Dounce glass homogenizer using three complete up and down cycles with A-type pestle in isolation buffer (IB) as described in Fecher, Trovo *et al.* 2019 The sample was transferred to a cell disruption vessel and processed with nitrogen cavitation at 800 psi and under stirring at 60 rpm for 10 min. Protease inhibitor was added to the resulting tissue fraction, and subcellular sediments were removed via two times centrifugation at 600g for 10 min. The resulting post-nuclear tissue fraction was filtered through a 30 µm cell strainer. For immunopurification (IP), the post-nuclear tissue fraction was diluted to a maximal concentration of 2mg tissue/ mL in immunopurification buffer (IPB) and 50µl microbeads coated with mouse IgG1 subtype antibody (Miltenyi Biotec) against GFP was added to the sample and incubated for 60 min at 4°C on the shaker. Magnetic-activated cell sorting (MACS) was applied to separate the microbead-coated mitochondria. The LS columns (Miltenyi Biotec) were placed in a magnetic QuadroMACS^{TM} separator (Miltenyi Biotec) and equilibrated with 3 mL IP buffer. The samples were applied to the column in repeating 3ml steps, followed by three times washing steps with IP buffer. The columns were then removed from the magnetic separator, and the microbead-coated mitochondria were gently flushed out with the plunger. Mitochondria were pelleted via centrifugation for 3 min with 12,000g at 4°C and washed twice with IB (without BSA and EDTA), and the pellets were immediately stored at -20°C for further experiments.

Protein amount determination

Protein concentration was determined using the BCA assay (Pierce BCA Protein Assay Kit; Thermo Fisher Scientific) according to the manufacturer’s instructions. BSA was used as the standard and sample buffer was used to correct for measurement alterations caused by detergent or BSA.

Sample preparation for mass spectrometry

Samples for mass spectrometry were obtained from 6- to 8-week-old male mice. Mitochondria were immunocaptured from the spinal cord according to the above-described protocol. Samples were lysed in a modified RIPA buffer (1% Triton X-100, 0.5% sodium deoxycholate, 0.1% SDS, 150 mM NaCl, 5 mM EDTA, 50 mM Tris–HCl, pH 8). Cell debris and undissolved material were removed by centrifugation for 10 min, at 16,000g, 4 °C. Protein concentrations were assessed using the BCA assay. A protein amount of 20 µg was further diluted 1:2 with water, and 50 mM $MgCl_2$ was added. $MgCl_2$ was added to a final concentration of 10 mM, and DNA/RNA was digested using 12.5U Benzonase (Sigma-Aldrich). Disulfide bonds were reduced by adding dithiothreitol (DTT) to a final concentration of 10 mM and incubation for 30 min at 37°C. Cysteine alkylation was performed by adding iodoacetamide (IAA) to a final concentration of 40 mM and incubation for 30 min at 24 °C in the dark. The alkylation step was quenched by adding 4 µL of 200 mM DTT.

Protein digestion was performed using the single-pot, solid phase, sample preparation (SP3) protocol (Hughes et al., 2019). Briefly, 10 µL of a 4 µg/µL bead slurry of Sera-Mag SpeedBeads A and B (GE Healthcare) were added to 20 µg of alkylated protein lysate. Protein binding to the magnetic beads was achieved by adding acetonitrile (ACN) to a final volume of 70% (v/v) and mixing at 1200 rpm at 24 °C for 30 min in a Thermomixer (Eppendorf, Germany). Magnetic beads were retained in a DynaMag-2 magnetic rack (Thermo Fisher Scientific, US) and the supernatant was discarded. Detergents were removed using four washing steps with 200 µL 80% (v/v) ethanol. Proteins were digested with 0.25 µg LysC (Promega) at 37°C for 3 hrs followed by a second digestion step with 0.25 µg trypsin (Promega) for 16 hrs at room temperature. Tubes were placed in a magnetic rack and peptides were transferred to 0.22 µm Costar Spin-X filter tubes (Corning) to remove remaining magnetic beads. Samples were dried by vacuum centrifugation. Finally, peptides were dissolved in 20 µL 0.1% (v/v) formic acid (FA). And the peptide concentration was estimated using the Qubit protein assay (Thermo Fisher).

Liquid chromatography-tandem mass spectrometry data acquisition

Samples were analyzed on an Easy nLC-1200 nano UHPLC (Thermo Fisher Scientific) coupled online via a Nanospray Flex electrospray ion source (Thermo Fisher Scientific) equipped with a column oven (Sonation) to Q-Exactive HF mass spectrometer (Thermo Fisher Scientific). An amount of 1.3 µg peptides was separated on self-packed C18 columns (300mm×75 µm, ReproSilPur 120 C18-AQ, 1.9 µm; Dr. Maisch) using a binary gradient of water (A) and acetonitrile (B) supplemented with 0.1% formic acid (gradient: 0 min., 2.4% B; 2 min., 4.8% B; 92 min., 24% B; 112 min., 35.2% B; 121 min., 60% B). Full mass spectrometry spectra were acquired at a resolution of 120,000 (automatic gain control (AGC) target: 3E+6). The 15 most intense peptide ions were chosen for fragmentation by higher-energy collisional dissociation (resolution: 15,000, isolation width: 1.6 m/z, AGC target: 1E+5, normalized collision energy (NCE): 26%). A dynamic exclusion of 120 s was applied for fragment ion spectra acquisition.

Liquid chromatography-tandem mass spectrometry data analysis

All proteins which were detected in > 50 % of the samples within one experimental group (EAE or control) were subjected to subsequent analysis. Missing values (NA) were not imputed. The raw label-free quantification (LFQ) values were $\log_2$-transformed. QQ plots were inspected to assess the skewness of the distribution of LFQ values. For subsequent analysis, LFQ values were treated as interval scale values.

To test the similarity of samples within the respective experimental group, principle component analysis (PCA) and correlation analysis were performed. To visualize the PCA results, the first two principle components (PC) were plotted and annotated with their (relative) explained variance. For correlation analysis, the correlation coefficients between all samples (regardless of the experimental group) were calculated according to Pearson. They were sample-wise standardized and the resulting z values colour-coded and shown in a heatmap. The matrix of z values was hierarchically clustered based on the Euclidean distances between the z values.

To test if a protein was differentially expressed between the EAE and control group, we calculated a student´s t-test and a fold change of the LFQ values between the experimental groups. To control for type I error inflation, a q value was derived from a permutation test. Here, a “t value” which was more extreme than the 5 % or 95 % quantile was considered as statistically significant ($q \leq 0.05$). To assess the effect size of the differential protein expression, we calculated the fold change (FC) between the LFQ values (in a logarithmic scale). A FC > 1.5 (upregulation) or FC < 1.5 (downregulation) was considered as biologically meaningful. To assess the relationship between the false-positive rates and the true positive rates depending on the fold change threshold, a receiver operating characteristic curve (ROC) was calculated. To interpret different FC thresholds, their distance to the cartesian origin of the ROC plot was calculated and plotted.

A protein was considered as a mitochondrial protein according to MitoCarta 2.0[103]. Likewise, the information to which mitochondrial respiratory chain complex a protein would belong to was derived from the MitoCarta database. To test if mitochondrial, non-mitochondrial proteins and proteins from different mitochondrial respiratory chain complexes were equally abundant, the LFQ values were standardized and visually inspected. Furthermore, a one-way analysis of variance was calculated to test for statistically significant differences. In order to control for the variance when calculating central tendencies, effect sizes (d) were calculated according to Cohen.

To better understand the functional patterns of EAE and healthy mitochondrial proteomes, a gene set enrichment analysis (GSEA) was performed. Proteins which are members of gene sets and showed the most extreme normalized enrichment score (NES), were further analysed. All analysis was done with R or Python.

Immunohistochemistry

Animals were anaesthetized with isoflurane and perfused transcardially with 5000 U/mL heparin in 1x phosphate-buffered saline (PBS) followed by 4% PFA in phosphate buffer (PB). Brain and spinal cord were dissected and post-fixed in 4% PFA overnight, dehydrated in 30% sucrose and embedded in Tissue-Tek® O.C.T.TM compound (Sakura Finetek Europ B.V., Netherlands) for cryo-cutting. 50 µm cryosections were permeabilized with 0.1-0.3% Triton-X 100 in 1x PBS for 10 min at RT on the shaker and blocked in blocking buffer containing 10% bovine serum albumin (BSA), 10% fetal bovine serum (FBS) and 10% fish gelatin for 1-2 hrs.

Antigen retrieval procedures were applied to unmask antigens and epitopes: sections were treated with either 10mM citrate buffer pH 6.0, 10mM EDTA buffer pH 8.0 or citrate-EDTA (10 mM citric acid, 2 mM EDTA and 0.05% Tween20) pH 6.2 for 10 min at RT followed by 30 min at 90˚C and 30 min at 4 ˚C. The tissue was further rinsed with 0.05% Tween20 in 1x PBS before proceeding the blocking procedure. Primary antibodies were incubated overnight at 4°C at a dilution of 1:400 (MCU, Mdh2, Idh3a, Idh2, CS, Pdp1, Sdhc, Suclg2, Slc16a1, Ndufv3, Cox6a1, Cox4i1) or 1:1000 (RFP and GFP, see manufacturer information in Chapter 3.1.3). Secondary antibodies (Alexa Flour® 488 and Alexa Flour® 594) were added at a dilution of 1:500 for 2 hrs at RT. Nuclei were counterstained with DAPI when necessary, and then the sections were mounted using Vectashield mounting medium (H-1000; Vector Laboratories). To perform double staining of mitochondrial markers with antibodies raised in the same species, Zenon Alexa Fluor 647 Rabbit IgG Labeling Kit (Z25308; Thermo Fisher Scientific) was applied according to the manufacturer's instructions: 1 µg of rabbit anti-Idh2 antibody was incubated with 10 µl of component A and stopped with 10 µl of component B after 5 min incubation. Sections were incubated with Zeno complex after incubation 2 hrs with secondary antibody followed by extensive washing. The sections were then washed three times in 1x PBS for 5 min and further mounted using Vectashield mounting medium (H-1000; Vector Laboratories).

Confocal imaging and image processing

Immunostained samples were imaged with an Olympus Fluoview (FV1000) confocal system mounted on an upright BX61 microscope stand (Olympus). The system was equipped with ×4/0.28 N.A. air, ×10/0.4 N.A. air, ×20/0.85 N.A. oil and ×60/1.42 N.A. oil immersion objectives. Images were obtained using standard filter sets and processed with Fiji. For representative figures, different channels of image series were pseudo-colour-coded using the “screen” function in Adobe Photoshop. Contrast and brightness were equally adjusted across the entire image. Immunofluorescence staining on Thy 1- MitoTag-RFP tissues were acquired with the same settings and were adjusted with the same processing parameters. In non-quantitative panels, gamma was adjusted nonlinearly to enhance the visibility of low-intensity objects. Figures were assembled in Adobe Illustrator.

Statistics

Statistical analysis was performed using Microsoft excel software and GraphPad Prism (GraphPad Software, Version 7.0, La Jolla, USA). Sample sizes were chosen according to previous in vivo imaging studies of spinal axons described in Nikic *et al.*, 2011. Normality of distribution was assessed with the Shapiro-Wilk test. When normal distribution was confirmed, t-test was applied for two groups comparison, and one-way ANOVA followed by Tukey’s posthoc comparison was used for more than two groups. Where normal distribution could not be confirmed, Kruskal–Wallis test followed by Dunn’s multiple comparisons test or Mann–Whitney U test was used. Obtained p-values were stated as significance levels in the figure legends (**** $P<0.0001$, *** $P<0.001$; **$P<0.01$; *$P<0.05$).

4. Result

4.1 The axonal ATP-to-ADP ratio in acute neuroinflammatory lesions

Multiple lines of evidence suggest that energy deficiency is one of the crucial features in MS lesions. It is a well-known theory that energy deficiency leads to ionic imbalance and intracellular Ca^{2+} accumulation, eventually damages the axonal transport and causes axonal degeneration. Demyelinated axons are presumably more vulnerable to the energy deficits given the higher energy demand required to keep up ionic homeostasis and maintain the impulse transmission in both noninflammatory and inflammatory contexts[49,104]. Cellular energy status, therefore, has become an important aspect to understand the contribution of mitochondria to the pathogenesis of inflammatory neurodegeneration.

4.1.1 Generation of PercevalHR mouse line

Based on the hypothesis of mitochondria damage could causing axonal energy crises, we aimed to investigate whether axonal energy levels are altered in acute inflammatory lesions. The ATP-to-ADP ratio is a critical parameter of a cell´s energy status and can be detected by using a genetically-encoded ratiometric biosensor. PercevalHR is a competitive binding system with two distinct excitation wavelengths. ATP binding increases the fluorescence at 500 nm excitation, while ADP increases the fluorescence at 420 nm excitation and the ratio between both indicates the ATP-to-ADP level. These characteristics make it spectrally compatible for multichannel imaging either *in vitro* or *in vivo* (see chapter 1.3.2.3).

After verifying the functionality of the Perceval sensor in HEK-293 cells, Thy1-PercevalHR mice were generated by standard pronuclear injection of linearized Thy1-PercevalHR DNA at the transgene facility of the Max Planck Institute for Molecular Cell Biology and Genetics, Dresden (see chapter 3.2). Seven founder lines were generated, and five of them further subjected to screening. Three of them, lines 06, 17 and 20, were exceptionally bright in spinal cord axons and were chosen for functional characterization. Thy 1- PercevalHR-20 displayed dense expression (approximately 90% of neurons are labelled), including in dorsal root ganglia (Figure 14, left column). However, the sensor was not responsive to the pharmacological application of oxidative phosphorylation inhibitors (such as iodoacetic acid and carbonyl cyanide 3-chlorophenylhydrazone) *in vivo* (data not shown).

Thy 1-PercevalHR-17 line presented fulgent expression in both the CNS and PNS (Figures 14, middle column), especially in the neuromuscular junction (NMJ). Sensor expression in Thy 1- PercevalHR-17 was brighter in comparison with Thy 1- PercevalHR-06 and Thy 1-PercevalHR-20, which makes it better suited for neurodevelopmental study. Thy 1-PercevalHR-17 was tested with iodoacetic acid *in vivo* and was nicely responsive to the pharmacological inhibition (data not shown).

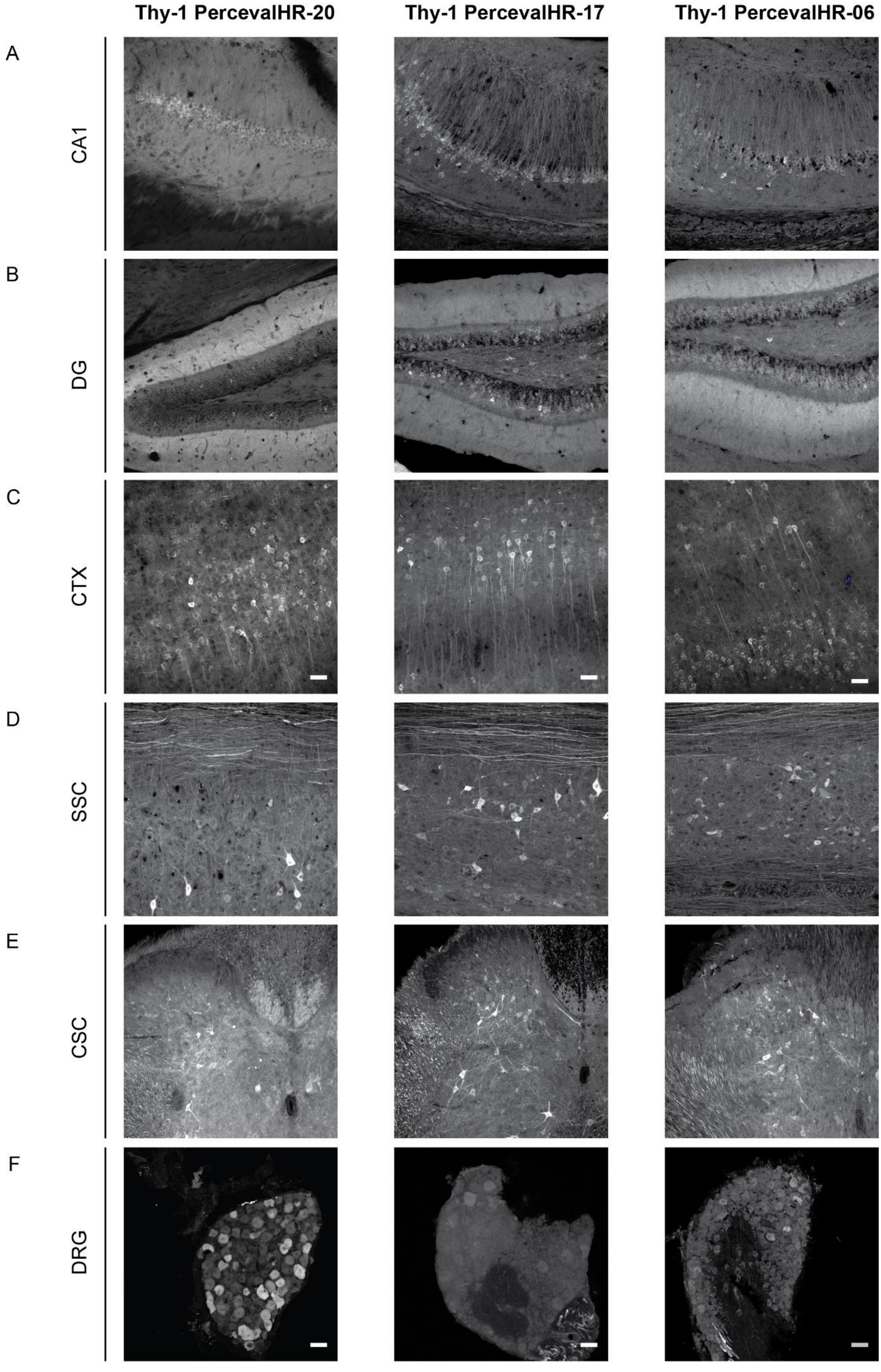
Thy-1 PercevalHR-20
Thy-1 PercevalHR-17
Thy-1 PercevalHR-06
A
CA1
B
DG
C
CTX
D
SSC
E
CSC
F
DRG

Figure 14: *In situ* characterization of Thy 1-PercevalHR-20, Thy 1- PercevalHR-17 and Thy 1- PercevalHR-06.
(A-F) Low magnification images show the GFP labelling of PercevalHR sensor in the brain and spinal cord of Thy 1-PercevalHR-20 (left column), Thy 1- PercevalHR-17 (middle column) and Thy 1- PercevalHR-06 (right column) including CA1 (A), DG (B) cortex (C), sagittal (D) and transverse (E) sections of the spinal cord and DRG (F). Scale bar = 50 µm

Thy 1- PercevalHR-06 revealed sparse labelling of axons in the dorsal hemisection, making it better suited for *in vivo* imaging in the spinal cord, allowing to distinguish single axons more clearly (Figure 14, right column).

In vivo functional characterization was performed with pharmacological application of 10 mM iodoacetic acid (IAA), a glyceraldehyde-3-dehydrogenase inhibitor, to block the glycolysis pathway[99]. Upon IAA application on the spinal cord of Thy 1- PercevalHR-6 mice, the peak of the emission spectrum shifted from 930 - 960 nm to 810 - 840 nm. It indicates the depletion of ATP from its binding site on the sensor, suggesting that the ATP-to-ADP ratio was decreased (Figure 15).

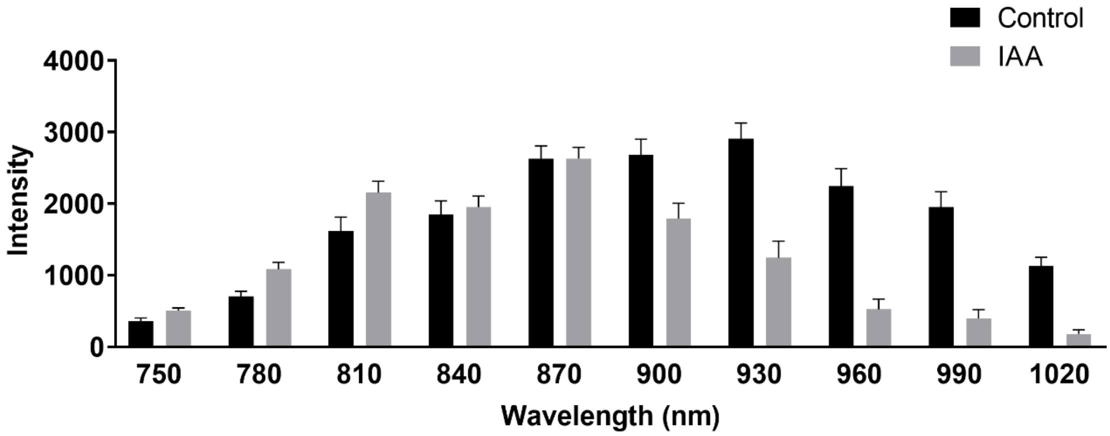

Figure 15: Thy 1- PercevalHR-06 *in vivo* characterization
The fluorescence emission spectrum from 750 nm to 1020 nm, showing a left shift which dictates the decreased ATP: ADP (ATP-to-ADP) following the application of 10 mM IAA. Tested in n = 3 animals per condition. Presented as mean ± s.e.m.

Based on its bright expression, sparse labelling, and sensitivity to detect changes in ATP-to-ADP ratio, the line Thy 1- PercevalHR-06 was selected to perform our EAE experiments.

4.1.2 ATP-to-ADP ratio decreases in spinal cord axons in acute EAE lesions

To determine whether axonal ATP-to-ADP ratio are changed in EAE, we induced EAE in Thy 1- PercevalHR-06 mice. Immunized mice generally showed first clinical symptoms with noticeable weight loss around eleven days after the initial MOG immunization. We then imaged the acute lesions in spinal cord axons at the peak of disease (two to three days after onset of the disease) and quantified the ATP and ADP levels in axons passing through the lesions. As compared to axons from healthy animals (normalized to the average value of control group: 1.00 ± 0.03), we revealed a significantly reduced ATP-to-ADP ratio (stage 0: 0.59 ± 0.02, stage 1: 0.53 ± 0.02, stage 2: 0.41 ± 0.03, mean ± s.e.m.) in axons from all stages of FAD within acute EAE lesions (Figure 16). However, we did not find changes in the ATP-to-ADP ratio in the axons from the dorsal roots, which are located far from lesions (0.82 ± 0.02 vs control: 1.00 ± 0.03).

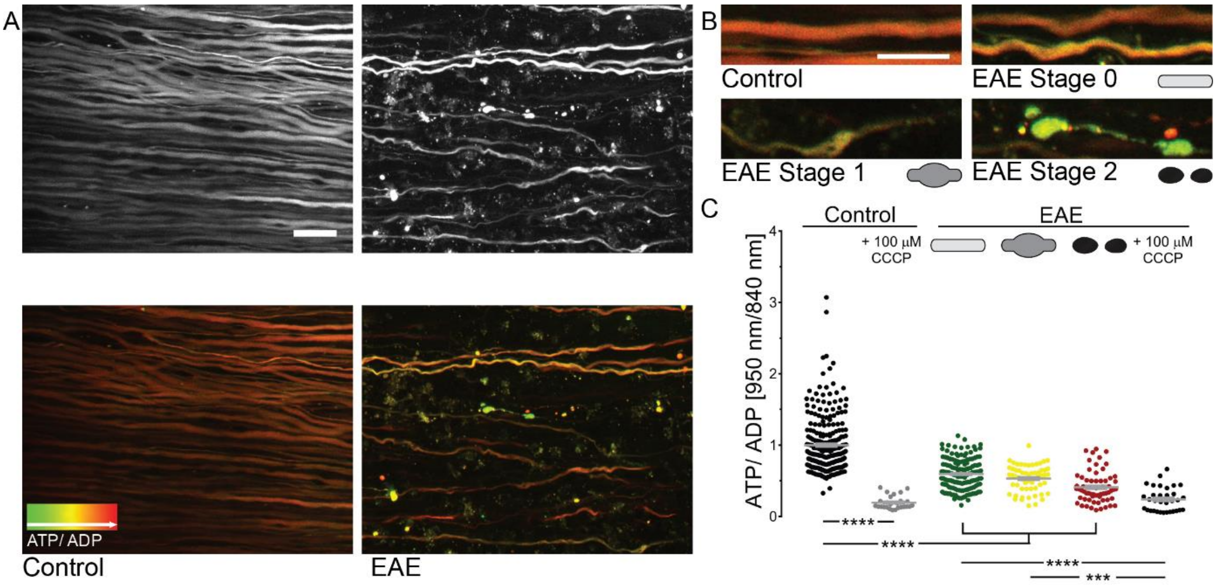

Figure 16: Reduction of ATP-to-ADP ratio in spinal axons occurs in the early stage of FAD of acute EAE.
(A) *In vivo* multiphoton maximum intensity projection of spinal cord axons of healthy (left) and EAE (peak of disease, right) in Thy 1-PercevalHR-6 mice. Top: grayscale images. Bottom: Pseudocolored (950 nm/840 nm) images for axonal ATP-to-ADP ratio in red and green, respectively. (B) Ratiometric projection images showing ATP-to-ADP level in healthy axons and normal-appearing (stage 0), swollen (stage 1), and fragmented (stage 2) axons in acute EAE lesions. (C) ATP-to-ADP ratio of single axons (950 nm/ 840 nm channel ratio normalized to the

mean of control axons) in the healthy spinal cord and different focal axonal degeneration stages in EAE (before and after application of 100 µM CCCP, respectively). Tested per animal in n = 6 control and n = 4 EAE mice. Kruskal-Wallis followed by Dunn's multiple comparison test were used to compare control versus EAE stages 0–2, control + CCCP and EAE + CCCP, respectively). Presented as mean ± s.e.m. Scale bars in (A) = 25 µm, and in (B) = 10 µm. ****, $p < 0.0001$.

To rule out any impact of differential pH values in the EAE environment on the fluorescent proteins, we applied either IAA (data not shown) or Carbonyl cyanide m-chlorophenyl hydrazine (CCCP), which is a mitochondrial oxidative phosphorylation uncoupler, in control and EAE mice to deplete the bindings of ATP to the sensors. In EAE, the ATP-to-ADP ratio of different stages significantly decreased to the level of CCCP-incubated control axons after applying CCCP. This data indicated that the observed change in ATP-to-ADP in EAE lesions was not a consequence of altered pH on the PercevalHR sensor (Figure 16C).

4.1.3 The decrease in the axonal ATP-to-ADP ratio persists in chronic neuroinflammatory lesions

To further investigate how axonal energy deficits evolve, we imaged animals at a later time point 22 days after onset of acute EAE. Similar to the acute lesions, we detected an overall homogeneous decrease in ATP-to-ADP ratio in axons undergoing all stages (stage 0: 0.69 ± 0.01, stage 1: 0.65 ± 0.01, stage 2: 0.41 ± 0.03, mean ± s.e.m.) of FAD in the lesions (Figure 17).

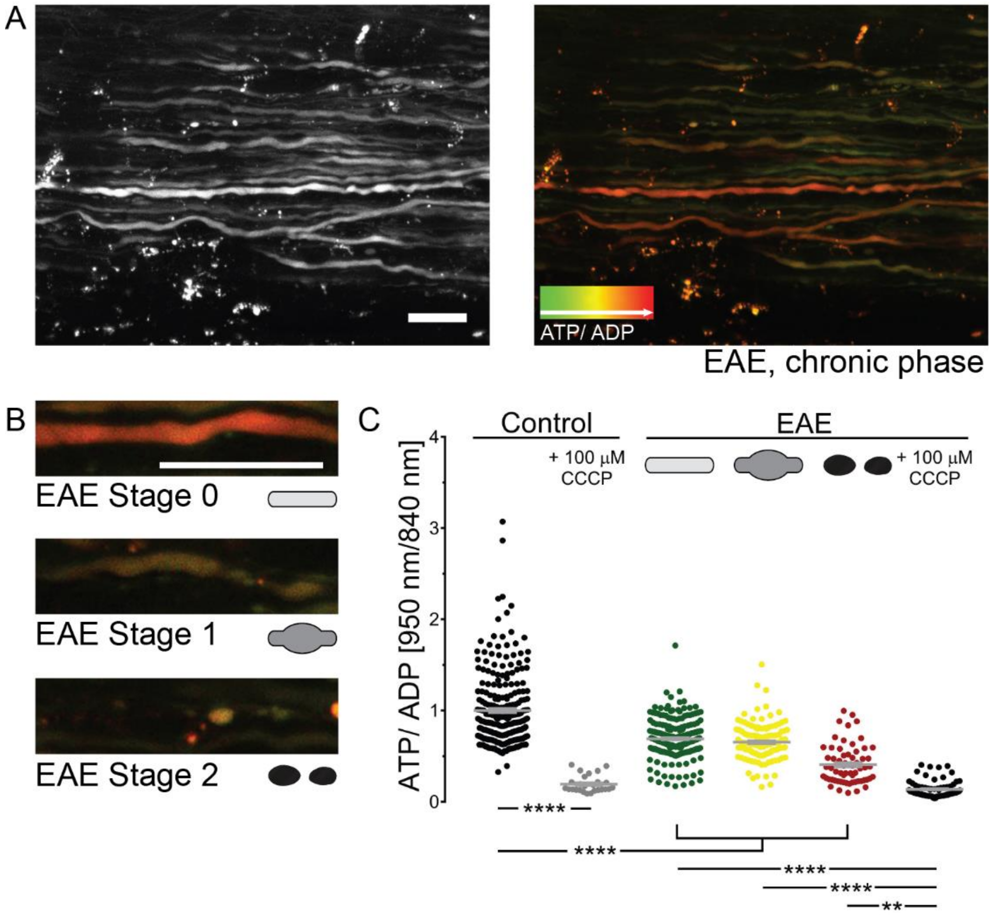

Figure 17: Reduction of ATP-to-ADP ratio in spinal cord axons persists to a chronic phase in acute EAE.

(A) *In vivo* multiphoton maximum intensity projection of spinal cord axons from the chronic phase of EAE (22 days after onset) in Thy 1-PercevalHR-6 mice. Left: grayscale image. Right: Pseudocolored (950 nm/840 nm) images for axonal ATP-to-ADP ratio in red and green, respectively. (B) Ratiometric projection images showing ATP-to-ADP level in normal-appearing (stage 0), swollen (stage 1), and fragmented (stage 2) axons in acute EAE chronic lesions. (C) ATP-to-ADP ratio of single axons (950 nm/ 840 nm channel ratio normalized to the mean of control axons) in the healthy spinal cord (same data set as Figure 16) and different focal axonal degeneration stages in chronic EAE (before and after application of 100 µM CCCP, respectively). Tested per animal in n = 6 control and n = 6 EAE mice. Kruskal-Wallis followed by Dunn's multiple comparison test were used to compare control versus EAE stages 0–2, control + CCCP and EAE + CCCP, respectively). Scale bars in (A) = 25 µm, and in (B) = 10 µm. **, $p < 0.01$; ****, $p < 0.0001$.

Our results show that there is a global decrease in the ATP-to-ADP ratio in spinal cord axons in neuroinflammatory lesions that persists into the chronic stage.

4.2 The role of mitochondrial oxidation in acute neuroinflammatory lesions

Mitochondrial ROS are produced at the electron transport on the inner mitochondrial membrane during the process of oxidative phosphorylation (OXPHOS). The release of electrons from OXPHOS leads to a partial reduction of oxygen to form superoxide, which plays a crucial role in regulating signalling pathways in physiological conditions but can become deleterious in pathological circumstances. In our previous work, Thy 1- Mito-Grx1-roGFP2 mice were generated to assess the mitochondrial redox signal in neurons[66]. These studies showed that time-lapse imaging could be used to monitor changes of the mitochondrial redox potential in laser axotomy and mechanical pin injury models[66,105].

4.2.1 Mitochondrial oxidation occurs only at the end stage of FAD

As one of the important features of focal axonal degeneration (FAD), mitochondrial damage was recapitulated through applying ROS or RNS to the healthy spinal cord[1], suggesting that reactive species might drive the pathological cascade that results in FAD. To identify whether abnormal mitochondrial ROS levels correlate to different stages of FAD in acute EAE, Dr. Giuseppe Locatelli has performed the EAE induction and imaged the mitochondrial redox potential in individual spinal axons using Thy 1- Mito-Grx1-roGFP2 × Thy 1- OFP 3 mice, which gives better temporal and spatial resolution in axonal mitochondria[66]. The morphology of mitochondria was monitored by measuring their shape factor defined by the length of a given mitochondrion divided by its width. As compared to healthy controls, the shape factor of mitochondria decreased gradually in axons in all stages of FAD (Figure 18A) (control: 6.66 ± 0.20, stage 0: 4.55 ± 0.16, stage 1: 3.65 ± 0.15, stage 2: 1.50 ± 0.10, mean ± s.e.m.). It correlates to the severity of axonal pathology, transitioning from an elongated shape in healthy controls to a swollen shape in EAE axons. The mitochondrial redox level was indicated by the ratio of emission after excitation at 405 nm over 488 nm. We found an increase of mitochondrial oxidation only in stage 2 EAE axons that were already fragmented (Figure 18B; control: 0.34 ± 0.01, stage 0: 0.30 ± 0.01, stage 1: 0.33 ± 0.02, stage 2: 0.67 ± 0.03, mean ± s.e.m.).

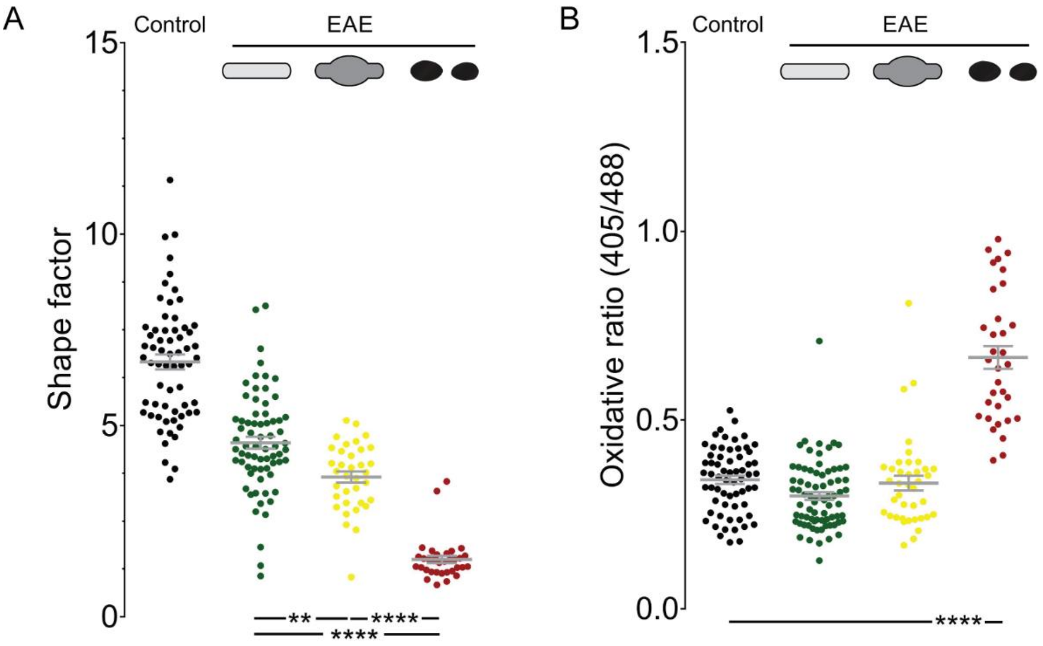

Figure 18: Mitochondrial redox levels are only altered at the end stage of FAD.
(a) Quantification of mitochondrial shape factor measured *in vivo* in the spinal cord in Thy 1-Mito-Grx1-roGFP2 × Thy 1- OFP3 mice. (b) Quantification of axonal mitochondrial redox levels. Tested per animal in n = 6 control and n = 7 EAE mice. - Tested per animal in n = 6 control and n = 6 EAE mice. One-way ANOVA followed by Tukey's multiple comparison test were used. Presented as mean ± s.e.m. **, $p < 0.01$; ****, $p < 0.0001$.

Overall, these results suggest that mitochondrial ROS is not the initial mediator in the pathogenesis of acute EAE, and oxidation is probably not a prerequisite for the morphological changes of mitochondria.

4.2.2 Genetically targeting of mitochondrial oxidation does not prevent mitochondrial or axonal pathology

To investigate whether counteracting oxidative stress could prevent mitochondrial pathology in the acute EAE, Dr. Giuseppe Locatelli genetically overexpressed manganese superoxide dismutase (MnSOD or SOD2) by crossing Thy 1- Mito-Grx1-roGFP2 × Thy 1-

OFP3 to MnSOD overexpressing line[106]. MnSOD is a member of the superoxide dismutase family, which detoxifies oxygen-free radicals. Data from previous work in our group has shown that transgenic overexpression of MnSOD in laser transected axons can prevent mitochondrial oxidation[66]. We could, however, neither prevent the mitochondrial oxidation nor rescue the morphological changes of mitochondria in acute EAE lesions (Figure 19). These results support our previous data and strongly suggests that mitochondrial and axonal damage in neuroinflammatory lesions are not driven by mitochondrial oxidation.

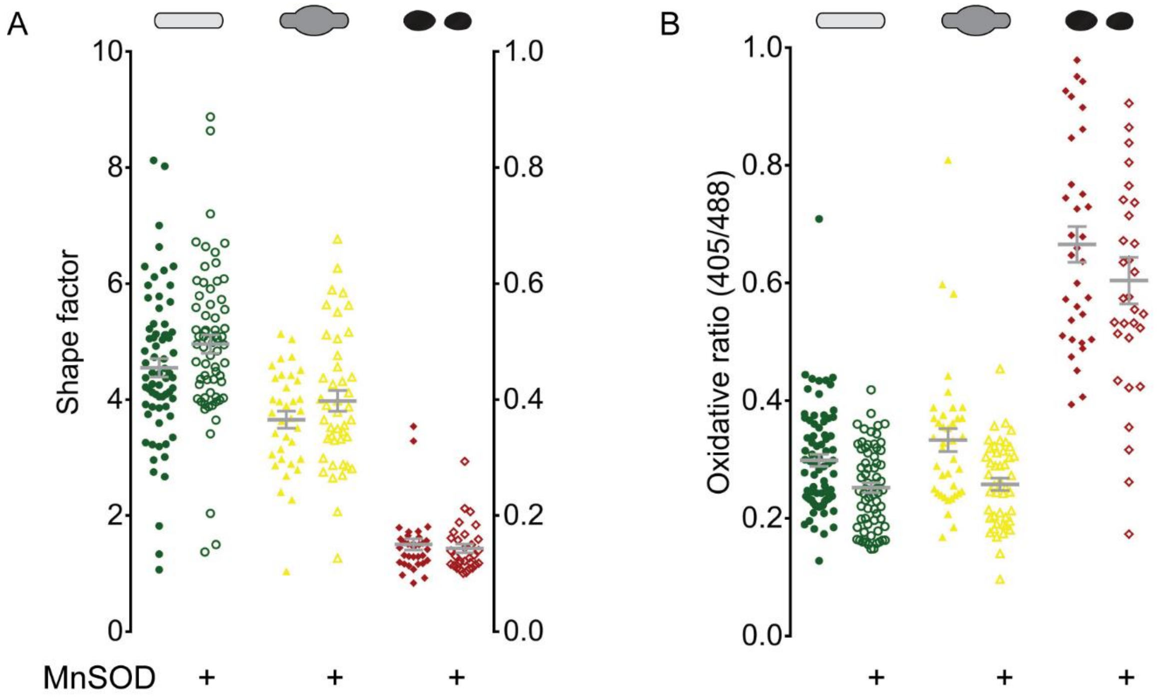

Figure 19: Mitochondrial oxidation at the late stage and structural alterations are not rescued by overexpression of MnSOD.
(A) Quantification of mitochondrial shape factor measured *in vivo* in the spinal cord of control and EAE Thy 1- Mito-Grx1-roGFP2 × Thy 1- OFP3 × MnSOD mice. (B) Quantification of axonal mitochondrial redox levels in control and EAE Thy 1- Mito-Grx1-roGFP2 × Thy 1- OFP3 × MnSOD mice. Tested per animal in n = 6 control and n = 6 EAE mice. Paired t-test was used to compare MnSOD (+) and MnSOD (-) in each stage. Presented as mean ± s.e.m.

4.3 The role of mitochondrial calcium homeostasis in neuroinflammatory lesions

Previous work has shown that the blockage of axonal calcium influx and genetic interference with cyclophilin D[107] prevented mitochondrial and axonal pathology in the paradigm of laser axotomy. Calcium, as a critical ion with multi-fold features, has been proved to be a predominant driver in the pathogenesis of FAD[108]. The results published by our group have indicated that the accumulation of cytoplasmic calcium that can enter from the extracellular space could determine the fate of FAD. However, the involvements of increased mitochondrial calcium in MS or MS models remained hazy. In this context, we wondered whether mitochondria contribute to FAD by acting as intracellular calcium stores that can both buffer and release calcium.

4.3.1 Generation of Thy 1- MitoTwitch2b mouse line

To study the involvement of mitochondrial calcium in the process of immune-mediated axon degeneration, Dr. Delphine Theodorou and Dr. Giuseppe Locatelli established an *in vivo* imaging approach based on the transgenic expression of a genetically encoded ratiometric calcium indicator in neuronal mitochondria. To create Thy 1- MitoTwitch2b mouse lines, the plasmid Twitch2B-pcDNA3 was kindly provided by Dr. Oliver Griesbeck (Max Planck Institute of Neurobiology, Martinsried, Germany). It encodes Twitch2B, which consists of mCerulean3, a low-calcium-affinity toad-fish Troponin C-minimal domain linker (1 functional EF-hand) and cpVenusCD[109]. Positive cloning candidates were tested for the functionality with chemicals to investigate the response of the sensors to the increased and decreased calcium level. The generation of the Thy 1- MitoTwitch2b mouse line was performed at the transgene facility of the Max Planck Institute for Molecular Cell Biology and Genetics, Dresden by standard pronuclear injections into pseudo-pregnant host mice. Further details in a schematic representation of Thy 1- MitoTwitch2b construct, the generation procedures and the *in situ* morphological characterization from 15 founder lines were elaborately described in Dr. Delphine Theodorou's thesis.

4.3.2 Mitochondrial calcium overload occurs only at the end stage of FAD

Calcium is one of the essential regulators of cellular function. Mitochondria act as a hub of intracellular calcium signalling and participate in a wide range of cellular processes as aforementioned. We, therefore, investigated whether mitochondrial calcium levels are altered in axons that pass through acute neuroinflammatory lesions. For this purpose, Dr. Giuseppe Locatelli and I induced EAE in Thy 1- MitoTwitch2b mice and imaged axonal mitochondria to determine their morphology and calcium levels ($[Ca^{2+}]_{Mito}$) at the peak of disease. Mitochondria stayed mostly elongated in healthy axons but revealed a rounded-up shape in EAE axons (Figure 20A, B), similar to our previous observations (Figures 18 and 19). The shape factor changed from 9.15 (± 0.25) in the control group to 5.69 (± 0.35) in stage 0, 3.86 (± 0.18) in stage 1, and 2.10 (± 0.10) in stage 2 axons in acute EAE lesions. Previous work has shown an increase of cytoplasmic calcium levels in a substantial fraction of axons in the early stages of FAD. We, however, only observed the elevation of mitochondrial calcium in stage 2 axons (Figure 20C) with a normalized mean value 1.54 ± 0.08 in acute inflammatory lesions as compared to control axons with 1.00 ± 0.02.

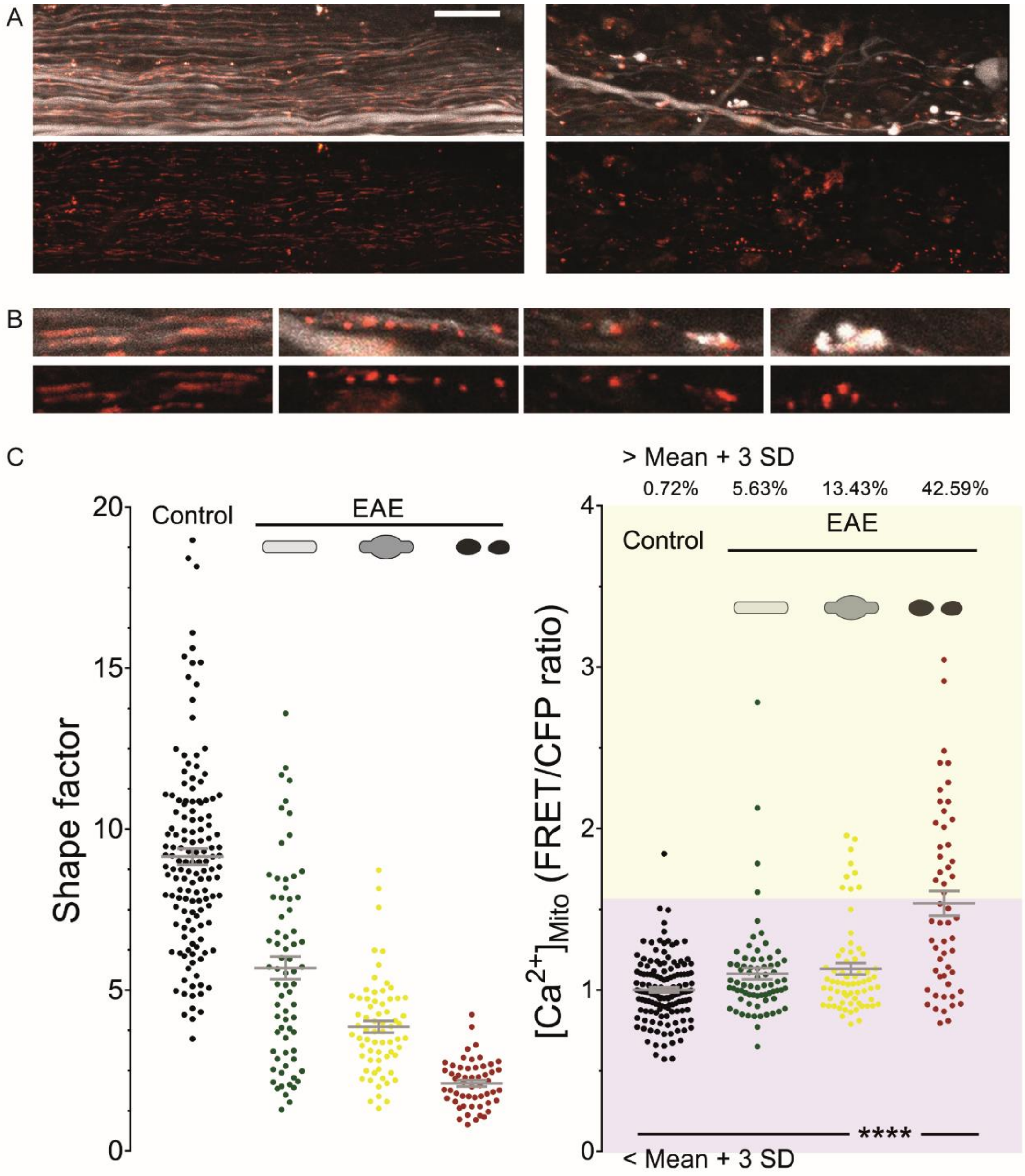

Figure 20: The rise in mitochondrial calcium is found in the late stage of FAD in acute EAE. (A) *In vivo* multiphoton maximum intensity projection of spinal cord axons of healthy (left) and EAE (peak of disease, right) in Thy 1- MitoTwitch2b × Thy 1- OFP3 mice. Top: pseudocoloured images of YFP channel. Bottom: pseudocolour-coded for mitochondrial calcium signal ($[Ca^{2+}]_{Mito}$) in the red overlay to grayscale axonal labelling. (B) Projection images showing $[Ca^{2+}]_{Mito}$ in healthy axons and normal-appearing (stage 0), swollen (stage 1), and fragmented (stage 2) axons in acute EAE lesions (axons in grayscale). (C) Quantification of mitochondrial shape factor measured *in vivo* in the spinal cord in Thy 1- MitoTwitch2b × Thy 1- OFP3 mice (left). Graph shows mean ± s.e.m., $[Ca^{2+}]_{Mito}$ of each axon (YFP/CFP channel ratio normalized to the mean of control axons) in the healthy spinal cord and at different stages of FAD (right). Percentages show the proportion of axons with increased $[Ca^{2+}]_{Mito}$ > control mean + 3 SD. Graphs are shown as mean ± s.e.m. Tested per animal in n = 10 control and n = 11 EAE mice. One-way ANOVA followed by Tukey's posthoc was used for comparison

of control versus EAE stages 0–2). ****, $p < 0.0001$

Compared to approximately 43% of stage 2 axons are categorized as high $[Ca^{2+}]_{Mito}$, the proportion of high $[Ca^{2+}]_{Mito}$ axons in early stages remains comparable to healthy control. Only a small fraction of was identified as high $[Ca^{2+}]_{Mito}$ axons (5.63% of stage 0 and 13.43% of stage 1 axons). When we further correlated the degree of axonal pathology and the calcium level in every single mitochondrion inside the spinal axons, we indeed observed the elevated calcium in a certain proportion of axonal mitochondria with 1.20 ± 0.02 in stage 0; 1.11 ± 0.02 in stage 1 and 1.51 ± 0.05 in stage 2 compared 0.99 ± 0.01 in healthy control (Figure 21). However, in all stages, the relative proportion of affected mitochondria is very small, making it unlikely that mitochondrial calcium is the primary driver of axonal pathology in the initial stages of FAD in the acute EAE.

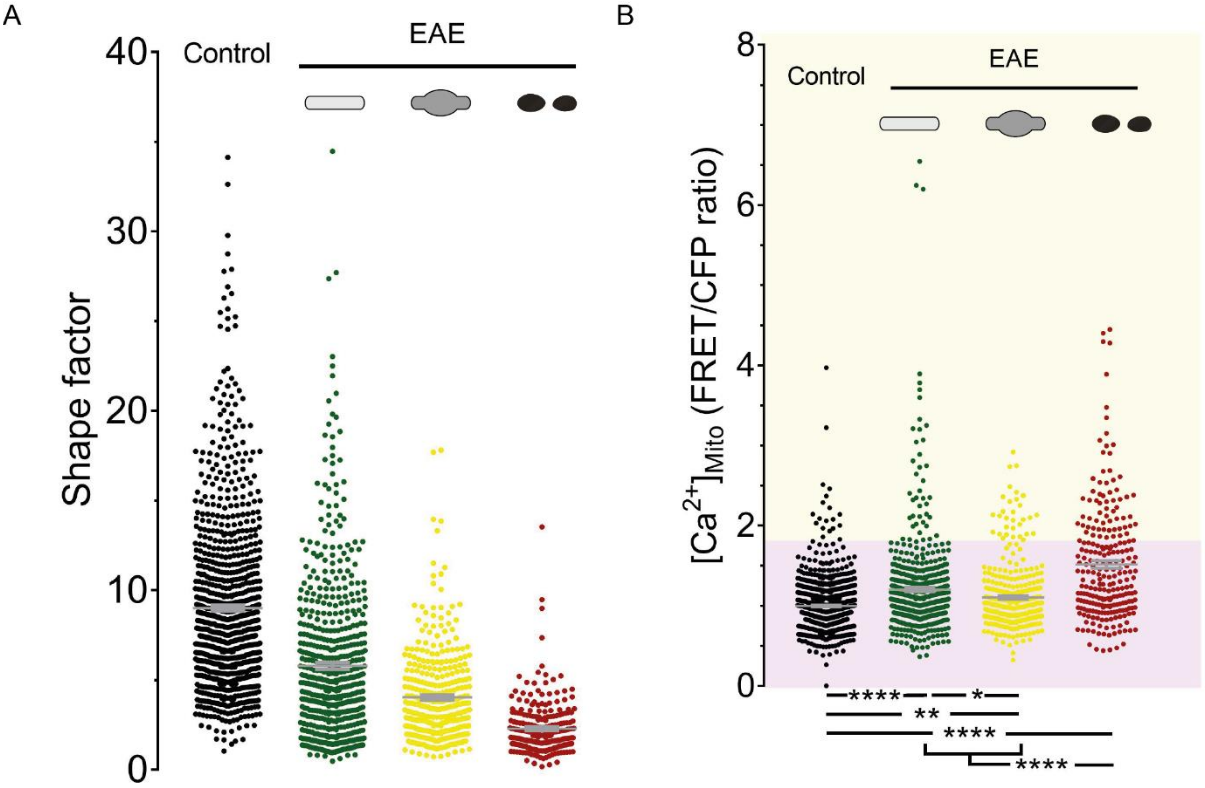

Figure 21: Single mitochondrion showed elevated mitochondrial calcium in different stages of FAD.
(A) Quantification of single mitochondrial shape factor measured *in vivo* in the spinal cord in

Thy 1- MitoTwitch2b × Thy 1- OFP3 mice. (B) $[Ca^{2+}]_{Mito}$ of each mitochondrion (YFP/CFP channel ratio normalized to the mean of control mitochondria) in the healthy spinal cord and at different stages of FAD. Graphs are shown as mean ± s.e.m. Tested per animal in n = 10 control and n = 11 EAE mice. One-way ANOVA followed by Tukey's posthoc was used for comparison of control versus EAE stages 0–2). *, $p < 0.05$; **, $p< 0.001$; ****, $p < 0.0001$.

4.3.3 Genetic targeting of mitochondrial calcium regulation does not prevent mitochondrial or axonal pathology

We next explored whether molecular manipulations of mitochondrial calcium handling can affect mitochondrial pathology in neuroinflammatory lesions. We first targeted the mitochondrial permeability transition (mPT) which describes an increase in the permeability of the membrane of mitochondria. A key player regulating the opening of permeability transition pore (mPTP) is cyclophilin D (CypD) which is inhibited by cyclosporin A (CsA) and as a result, blocks the opening of the mPTP. The inhibition results in a delay of mitochondrial swelling and improved retention capacity of mitochondrial calcium [107,110]. CypD, a product of the *Ppif* gene, is a vital chaperone protein that mediates the formation and opening of the mitochondrial permeability transition pore (mPTP) following the mitochondrial calcium overload[111], leads to the release of cytochrome c from the mitochondrial matrix and eventually causes the programmed cell death. Studies have shown that mitochondria isolated from *Ppif* homozygous knockout mice are resistant to swelling and permeability transition *in vitro.* The stability of these mitochondria against calcium overload is significantly increased[18].

Data shown from previous work proved that the deletion of cyclophilin D could mitigate the mitochondrial pathology in a laser axotomy model using Thy 1- Mito-Grx1-roGFP2 × cyclophilin $D^{-/-}$ mice[66]. Based on the observation that swollen mitochondria resulted from the calcium-induced opening of the mPTP[107], suggesting that cytoplasmic calcium accumulations might correlate with increased mitochondrial calcium, we sought to decrypt how genetic manipulation of *Ppif* influences axonal degeneration in acute neuroinflammatory lesions. To achieve that, we crossed the *Ppif* knockout mouse line to Thy 1- YFP mouse line to access the axonal labelling and induced acute EAE.

We characterized the distribution of axonal damage stages in the lumbar spinal cord within acute lesions (Figure 22). In the *Ppif*$^{/-}$ group, surprisingly, there was no significant difference in normal-appearing (stage 0) (*Ppif*$^{-/-}$: 40.67 ± 3.43 % vs *Ppif*$^{+/-}$: 35.51 ± 1.1 %), swollen (stage 1) (*Ppif*$^{-/-}$: 44.9 ± 4.85 % vs *Ppif*$^{+/-}$: 46.09 ± 1.29 %) and fragmented (stage 2) axons (*Ppif*$^{-/-}$: 14.43 ± 1.51 % vs *Ppif*$^{+/-}$: 18.41 ± 0.3 %). This data suggested that the deletion of *Ppif* has no apparent protective effect on axonal morphology in acute EAE lesions, at least on the morphological basis.

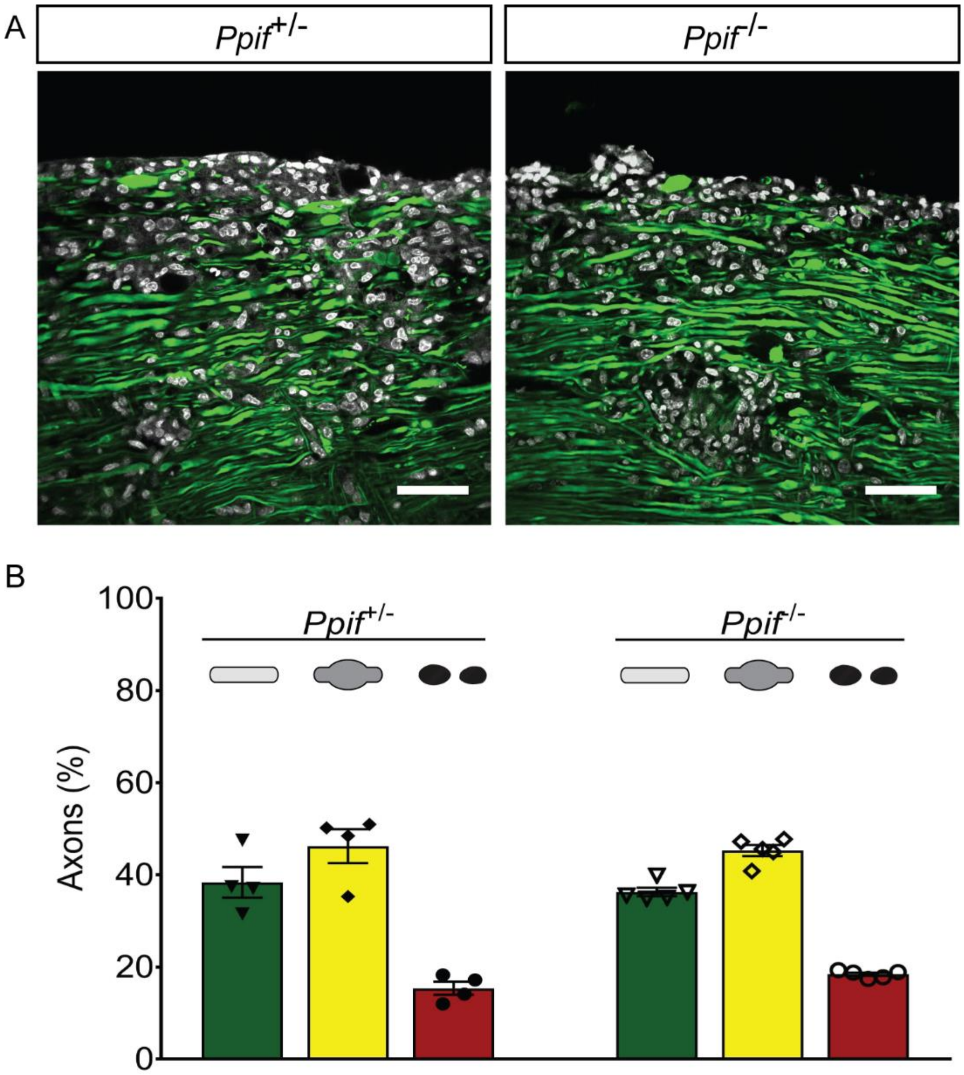

Figure 22: Axonal damage in acute EAE lesions in *Ppif*$^{-/-}$ animals.
(A) Substack projections of the lumbar spinal cord in a control animal *Ppif*$^{+/-}$ (left) and a *Ppif*$^{-/-}$ (right) mouse at the peak of disease. The lesion border was defined by the presence of infiltrating cells counterstained with neurotrace marker. Pseudocoloured code: axons are labelled in green; neurotrace marker in grayscale. (B) Distribution of axonal stages at the peak of disease in *Ppif*$^{-/-}$ and their littermate control *Ppif*$^{+/-}$. Graphs are shown as mean ± s.e.m. Tested per animal in n = 4 *Ppif*$^{+/-}$ and n = 5 *Ppif*$^{-/-}$ mice. Chi-square test (χ^2=0.2538, p=0.6144).

Following above, we further targeted mitochondrial calcium uniporters (MCU) which are recognized as unique high affinity (Kd ≤2 nM) calcium channels located at the inner membrane of mitochondria. They conduct calcium with high selectivity and acts as key molecules allowing the rapid accumulation of calcium across the inner membrane of mitochondria.

To delineate whether $[Ca^{2+}]_{Mito}$ in different stages of FAD is altered in MCU deleted mice, we adopted a MCU floxed mouse model: Mcu^{tm1a} × ACTB: FLPe[112]. In this model, MCU is conditionally deleted with the expression of Cre recombinase. To address the universal expression of Cre in both neuronal somata and cytosol, we neonatally injected two viruses intraventricularly: i) AAV9-*hSyn*: EGFP.Cre (working titer ~ 10^{12}) and ii) AAV9-*CAG*: FLEX (working titer ~ 10^{12}). Neurons labelled in GFP, therefore, were considered as MCU deleted. We then characterized the efficiency of the viral-driven deletion by immunostaining. First, we stained MCU on sagittal sections of the spinal cord to evaluate the GFP-labeled axons (region of interest) However, axonal labelling was too dim despite using an anti-GFP antibody to amplify the signal. We were unable to conclude whether MCU was effectively knocked out in spinal cord axons. We further focused on the grey matter to assess if MCU in neuronal somata were deleted. Indeed, we observed that a majority of GFP^{positive}-neurons lacked MCU expression in spinal cord grey matter (Figure 23A) and DRGs (Figure 23B). In ongoing experiments, we now use this approach to assess whether interfering with mitochondrial calcium uptake can affect mitochondrial and axonal pathology in EAE.

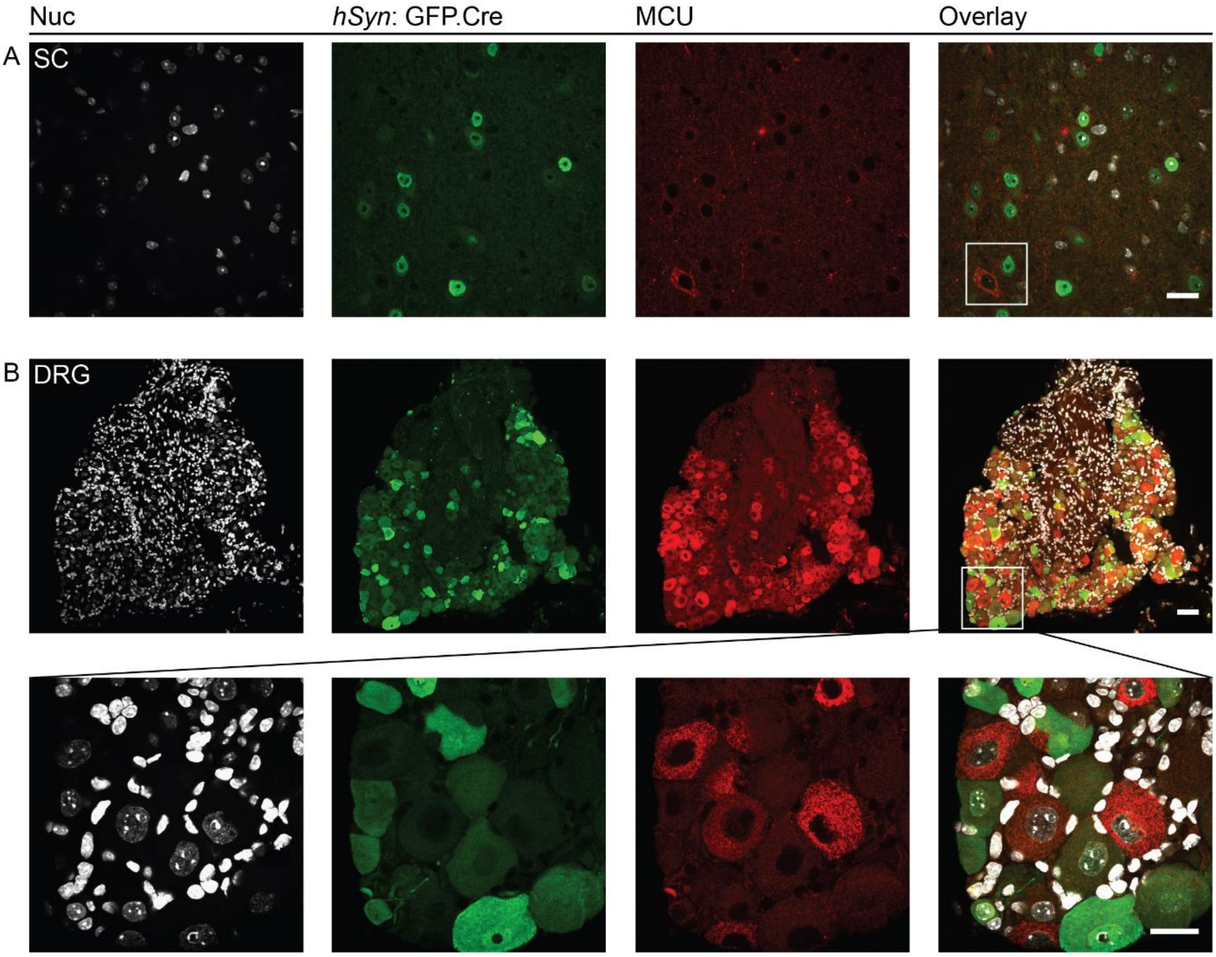

Figure 23: MCU expression pattern in viral-driven $\mathrm{MCU}^{FL/FL}$ spinal cord and DRG.
(A) Substack image from the lumbar spinal cord of *hSyn*: Cre/ $\mathrm{Mcu}^{FL/FL}$ mice. Scale bar = 50µm (B) Low (upper row, scale bar = 50µm) and high (lower row, scale bar = 25µm) magnification images of DRG neurons. In (A) and (B) MCU was stained with anti-MCU antibody (red), neurons with anti-GFP antibody and nuclei were counterstained with DAPI (grey).

4.4 Proteomic profiling of acute EAE-inflamed mitochondria in spinal cord axons

Previously, we have shown a diffused energy deficit in acute and chronic inflammatory axons which is presumably as a consequence of the mitochondrial defects based on the idea of their core function is to produce the ATP meeting the energy demand. In this section, we aimed to establish a proteomic profile to understand of which proteins are changed in neuroinflammatory lesions and whether these proteins mechanistically contribute to axonal energy deficits and degeneration.

4.4.1 Virally-driven labelling of neuronal mitochondria in CNS

To explore whether mitochondrial proteins crucial for certain functions, including redox-reactions, ATP production and transport/regulation of metabolites in and out of mitochondria, are changed in acute EAE, we applied a mass spectrometry-based approach using a cell-specific mitochondrial reporter line: MitoTag mouse[112].

This mouse line expresses GFP targeted to the outer membrane of mitochondria in a Cre-dependent manner. To drive the universal expression of GFP to the OMM in neuronal mitochondria, we performed neonatal-intraventricular injection on postnatal day-3 pups with AAV9.hSyn: iCre. We then *in situ* characterized the virally-driven GFP expression in the brain and spinal cord to validate the virus transduction efficiency (Figure 24).

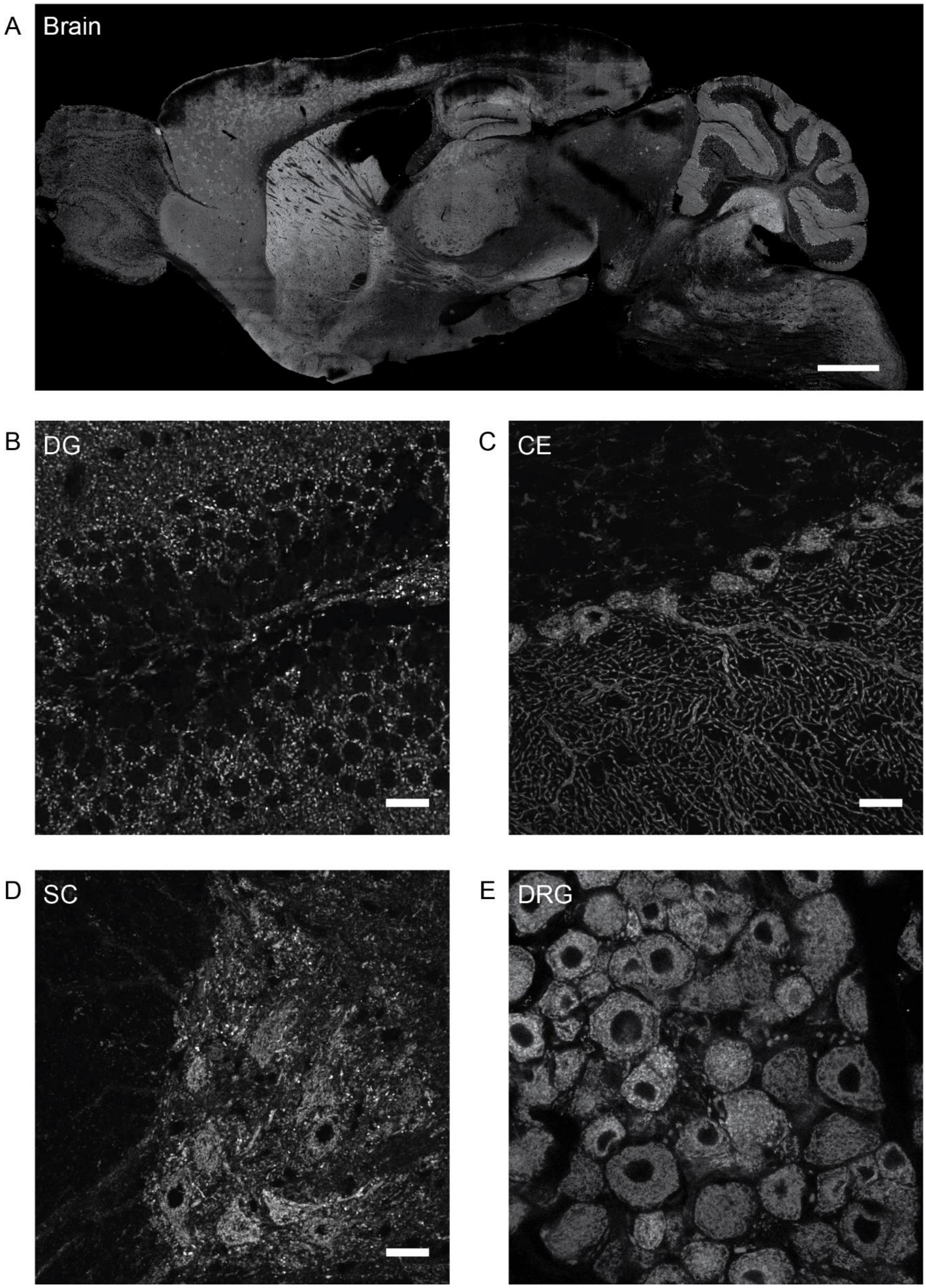

Figure 24: MitoTag neurons express viral-driven GFP to OMM in CNS.
Images of GFP expression driven by Cre under the human synapsin promoter, AAV9-hSyn:iCre, in virally transduced MitoTag mouse. (A) Overview image of the sagittal brain. Scale bar = 1500 µm. High magnification images of (B) dentate gyrus and (C) cerebellum. (D-E) High

magnification images in the transverse spinal cord and DRG. Scale bar = 20 µm.

This approach resulted in a bright expression of virus-driven GFP labelling throughout CNS regions, making it a valuable tool for the analysis of neuronal mitochondria in neuroinflammatory CNS lesions.

4.4.2 Mass-Spectrometry based proteomic analysis

We induced EAE in virus-injected MitoTag mice and performed mitochondrial isolation at the peak of disease. To specifically isolate GFP-tagged mitochondria, we used an optimized immunocapture protocol, established as described by Fecher *et al.*, 2019. This reference study established that following this approach the majority of GFP-captured objects were isolated mitochondria with well-preserved ultrastructure, as compared to the crude mitochondrial fraction (CMF), which contained not only mitochondria but also myelin debris. The samples were subsequently sent to our collaborator Prof. Dr. Stefan Lichtenthaler for mass spectrometry measurements.

4.4.3 Proteomic profile of neuronal mitochondria in inflammatory lesions of acute EAE

The establishment of proteomic profiling of inflamed mitochondria in acute EAE spinal cord was done in collaboration with Dr. Stephan Müller and Daniel Engels to determine differentially regulated proteins and their corresponding pathways.

At least five biological replicates of lumbar spinal cords were sampled for both healthy controls and acute EAE. After the initial data clean-up, a principle component analysis (PCA) and correlation analysis with unsupervised cluster analysis were performed to determine the similarity among the EAE and healthy control groups, respectively. PC1, which accounts for 52.6 % of the variance in the data, segregated EAE from control animals. This means that the immunocapture of samples was reproducibly prepared. The heatmap (correlation matrix) was presented combined with the unsupervised clustering which assembles samples based on the similarity of their expression pattern to identify if sample proteomes were similarly composed. Overall, samples within an experimental group showed a higher correlation than samples in-between groups. (Figure 25). As a result, all samples were included for further analysis.

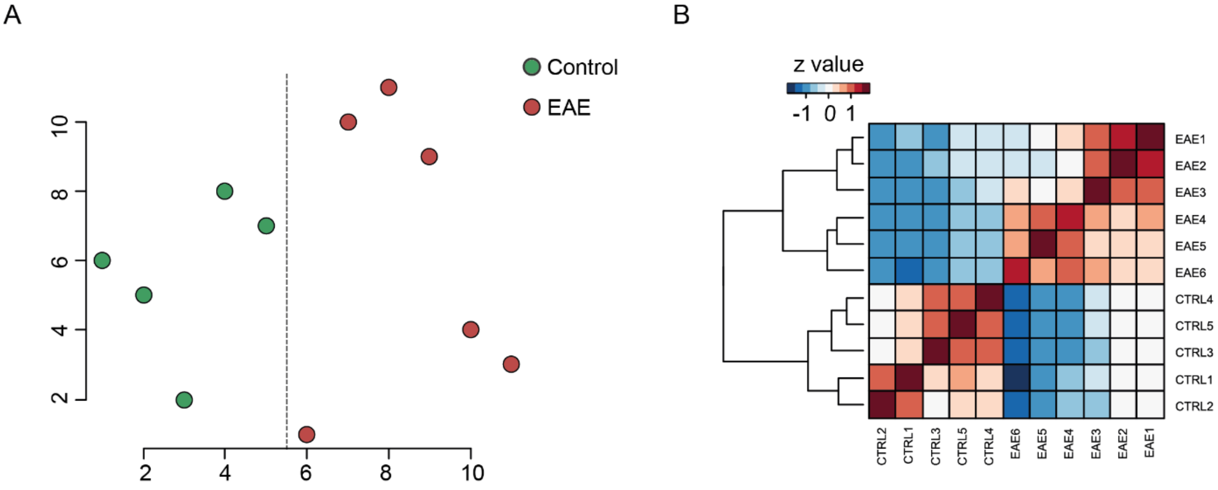

Figure 25: Quality control for experimental group sample similarity.
(A) The similarity of control and EAE samples was evaluated by principle component analysis (PCA). Principle component 1 (PC1, x axis), which accounted for 52% of the overall variance, could segregate EAE from control samples. (B) Correlation analysis of control and EAE samples displayed a good in-between sample correlation within both groups and a robust difference between samples from different groups. Row-wise normalized and colour-coded Pearson correlation coefficient.

Overall, 2,733 proteins were identified. Among those, 773 were classified as mitochondrial proteins according to the MitoCarta 2.0 database. The MitoCarta 2.0 database is an inventory of 1158 proteins with the integrated information from 6 genome-scale datasets of mitochondrial localization. This revealed that our study has a 66.8% coverage of MitoCarta annotated proteins. These mitochondrial proteins were selected for further analyses.

As expected, standardized $\log_2$ (LFQ) revealed strong enrichment of mitochondrial proteins in contrast to non-mitochondrial proteins ($d = -0.7$, $p < 0.001$). Proteins from different respiratory chain complexes were equally presented in EAE and control samples ($p = 0.669$, two-way ANOVA, Figure 26).

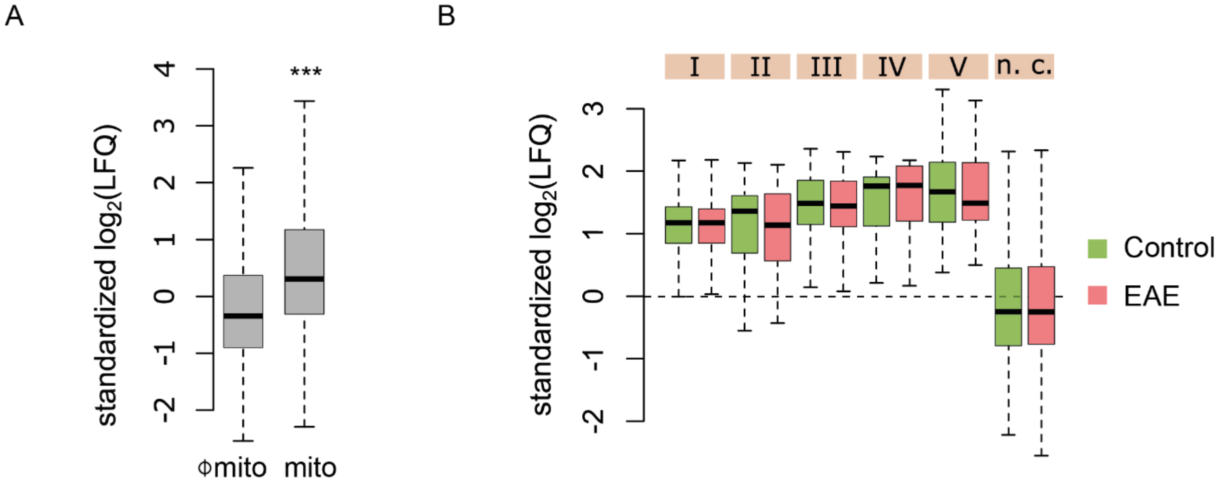

Figure 26: The abundance of mitochondrial proteins and mitochondrial respiratory chain complex (MRCC) proteins.
(A) Mitochondrial proteins in immunocaptured samples are significantly more abundant in comparison to non-mitochondrial proteins. (B) The abundance of MRCC proteins was higher than non-complex proteins and there was no difference in protein abundance compared between the control and EAE group (group: complex interaction, p = 0.147, two-way ANOVA).

Among the 773 mitochondrial proteins, 27 were differentially expressed (Figure 27, indicated in red, $\log_2$ (FC) > $|\log_2(1.5)|$ and q value ≤ 0.05), as shown in the volcano plot.

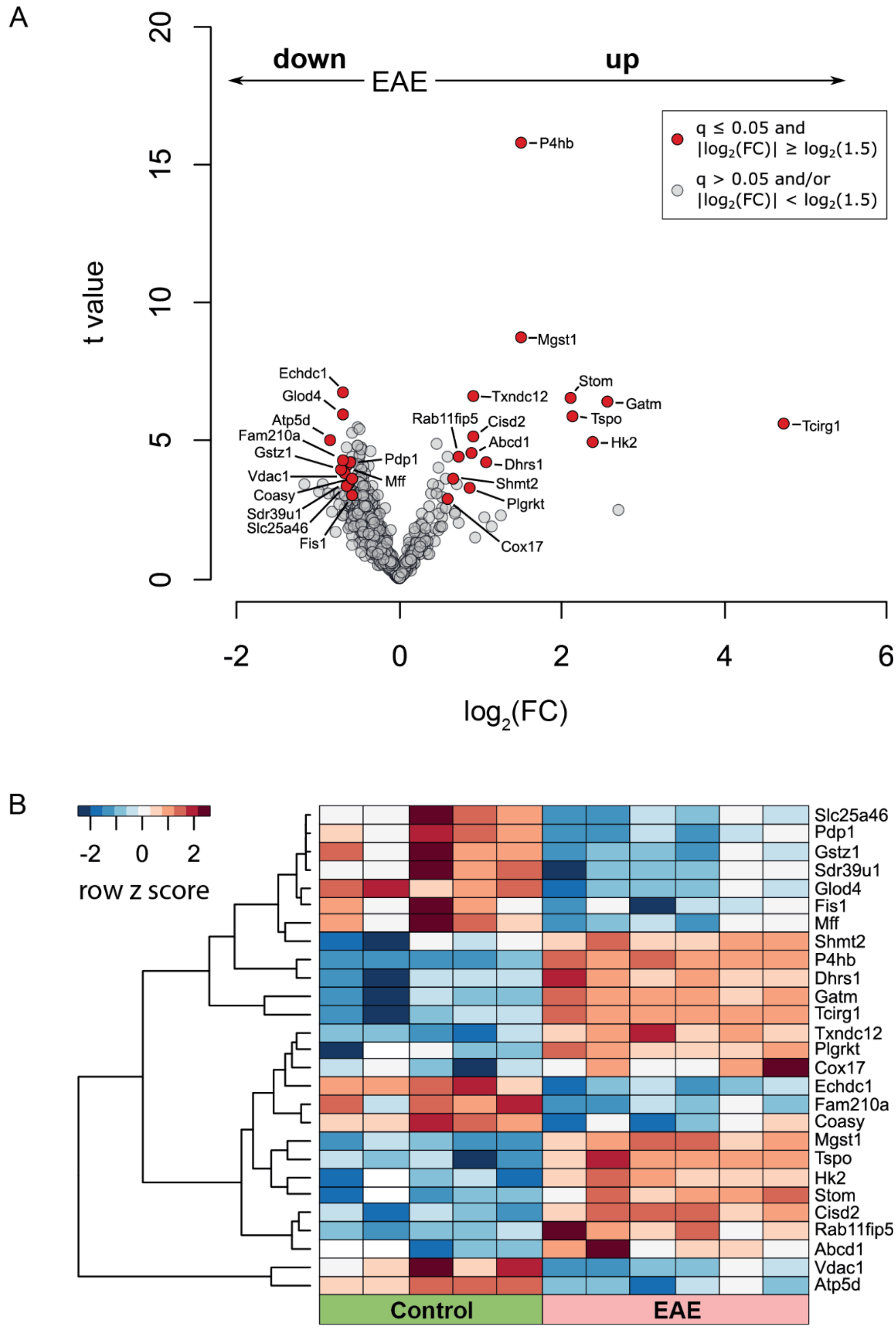

Figure 27: Proteomic profiling of neuronal mitochondria in the spinal cord of mice with acute EAE.

(A) Volcano plot shows the comparison of neuronal mitochondrial proteomes between healthy control and acute EAE groups (FDR ≤ 0.05, permutation-based t-statistics, iteration = 50,000 randomizations, n ≥ 3 quantifications). All dots represent the MitoCarta annotated proteins; red circles represent proteins with FDR ≤ 0.05. FC, fold change. (B) Matrix analysis of significantly enriched-MitoCarta annotated proteins reveals the up- and downregulated pattern in colors.

Next, we performed a gene set enrichment analysis (GSEA) to find proteins which form functional molecular clusters based on previously published information that could explain the contribution of mitochondria to EAE-specific axonal degeneration. The relative enrichment of annotations of Reactome pathways within the $\log_2$(FC)-ranked list of proteins was analyzed. In brief, all detected proteins were ranked according to their $\log_2$ (FC) and assigned to the respective gene sets (pathways). The density of proteins which are in a gene set (pathway) was compared to a simulated distribution which was acquired by repeating the analysis with randomly sampled gene sets of matching sizes. An enrichment score (ES) was calculated and normalized to the size of each pathway displaying the enrichment level without being affected by the cluster size of each pathway in the list. Positive and negative ES values represent enrichment degree from the top and the bottom of the list, respectively. Significance of enriched pathways was assessed by the difference of actual distribution and simulated distribution at the median rank.

We detected four significantly downregulated and two upregulated pathways (Figure 28A). We investigated all proteins enlisted in 4 significantly downregulated pathways and found the majority of the proteins associated with “Complex I biogenesis” and “Respiratory electron transport” are concordant with “Respiratory electron transport and ATP synthesis”. To validate whether annotated proteins enlisted in these significantly regulated pathways were indeed altered in the notion of protein expression in EAE as our proteomic profiling showed, 10 enriched candidates were selected based on literature and antibody availability for quantitative and qualitative analysis even though only a few proteins reached the criteria ($\log_2$ (FC) $> \left| \log_2(1.5) \right|$ and q value ≤ 0.05) and were considered as significantly regulated. The proteins of each significantly enriched gene set (pathways) were depicted separately (Figure 28B, C).

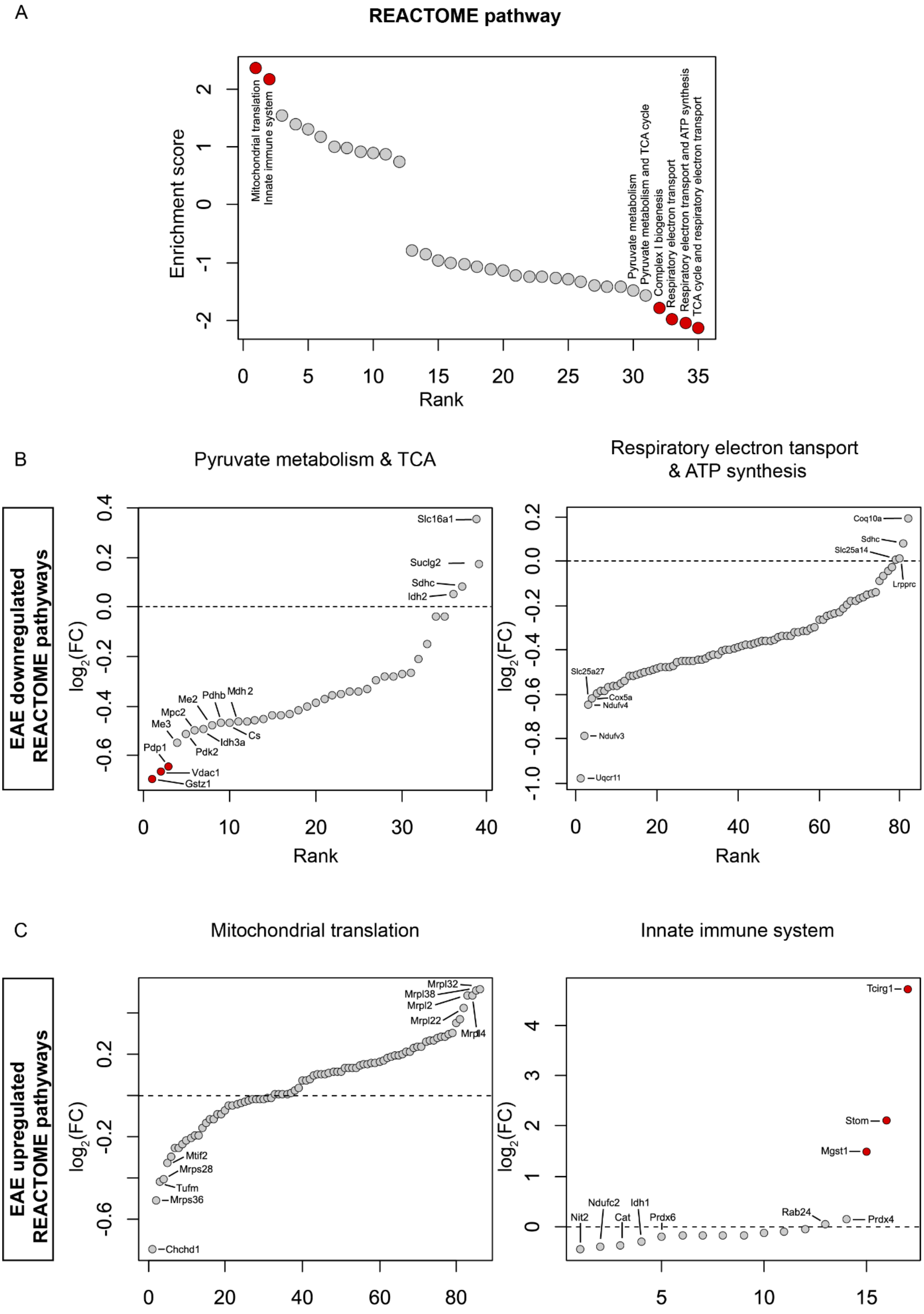

Figure 28: Leading edge analysis.
(A) Enriched pathways were ranked based on the enrichment score according to leading edge

analysis. Differentially regulated pathways were labelled in red ($q \leq 0.05$, derived from FDR corrected and permutation-based t statistics). (B) Chosen downregulated pathways and (C) upregulated pathways, and each annotated protein was ranked based on the $\log_2$(FC) values. Significantly enriched proteins were labelled in red.

4.4.4 Histological analysis of TCA cycle component expression in neuroinflammation

First, we tested these antibodies in tissue from virus-injected MitoTag mice. We confirmed 2 candidates were stained and subcellularly colocalized in mitochondria. To achieve homogeneous labelling of mitochondria in neurons, we used Thy 1- MitoTag-RFPH mice in which the neuronal mitochondria are transgenically labelled in RFP. From immunohistochemistry in the lumbar spinal cord of Thy 1- MitoTag-RFPH, we observed a substantial reduction of Idh3a in EAE neuronal somata with normalized mean fluorescence intensity (MFI): 0.39 ± 0.03 compared to control: 1.00 ± 0.12 (Figure 29A, B) and Mdh2 with normalized MFI: 0.23 ± 0.05 compared to control: 0.99 ± 0.08 (Figure 29C, D). Both Idh3a and Mdh2 are enlisted in the TCA cycle and involved in the pathway “Pyruvate metabolism and TCA”. The loss of these TCA cycle components is likely to impair the function of the respiratory chain and thus is expected to lead to reduced mitochondrial ATP production. These results can thus provide a molecular explanation for the universal energy deficits we observed in inflamed spinal cord axons.

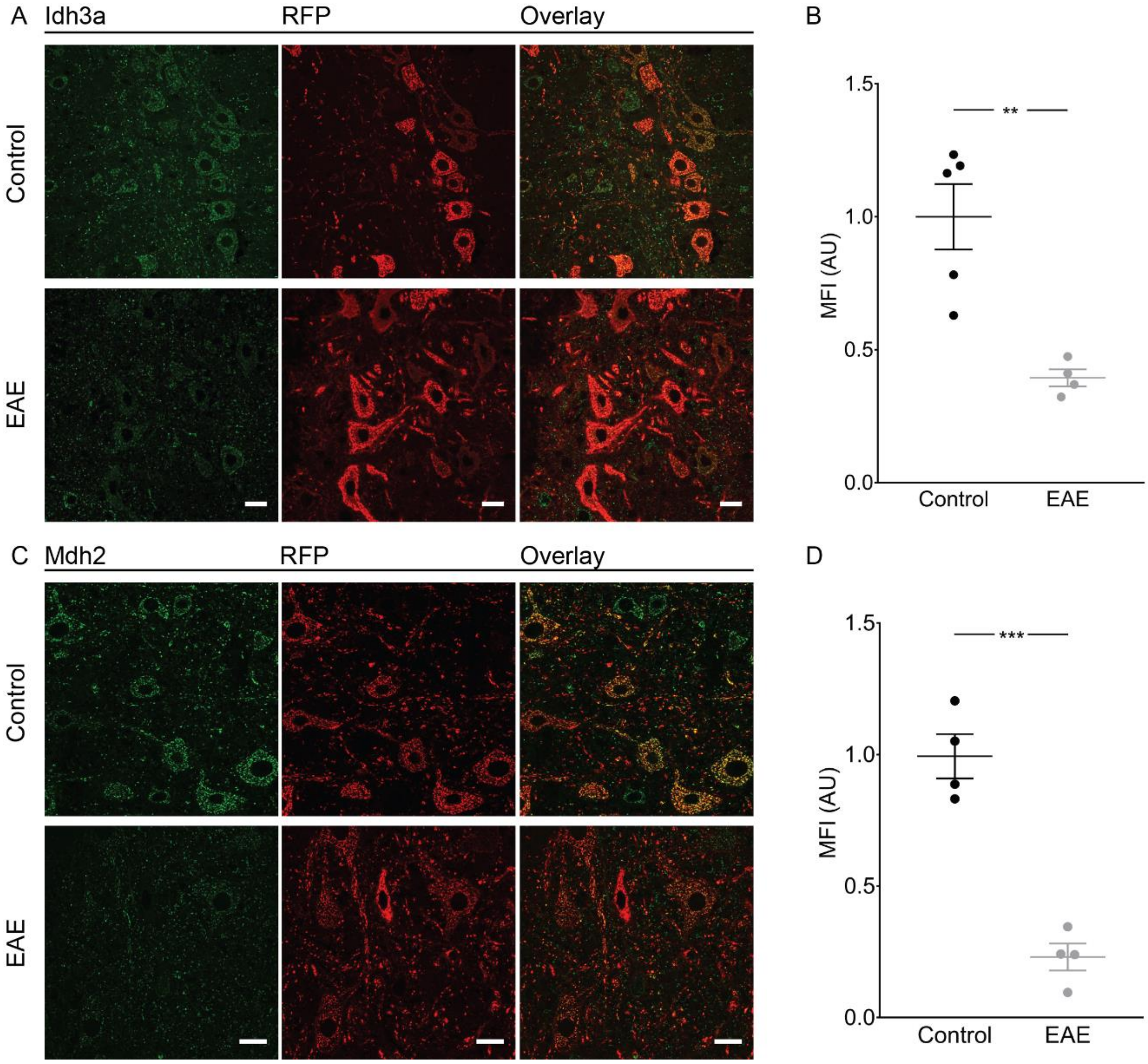

Figure 29: Reduction of protein expression in acute EAE spinal cord
(A) Immunohistochemical staining of Idh3a (green) in lumbar spinal cord sections of healthy and acute EAE mice colocalized with transgenic labelling of neuronal mitochondria (red). (B) Mean fluorescence intensity (MFI) of each group is plotted by the animal. (C) Immunohistochemical staining of Mdh2 (green) in lumbar spinal cord sections of healthy and acute EAE mice colocalized with transgenic labelling of neuronal mitochondria (red). (D) Mean fluorescence intensity of each group is plotted by the animal. MFI of the neuronal cytoplasmic region was subtracted to the nuclear region and normalized to average MFI of control. Two-tailed Student's t-test was used, $p = 0.0002$. Tested per animal in $n = 4$-5 control and $n = 4$ EAE mice. Presented as mean ± s.e.m. Scale bars in (A) and (C) = 25 µm, **, $p < 0.01$; ***, $p < 0.001$.

5. Discussion

5.1 Key findings:

Here, we applied *in vivo* two-photon microscopy together with the use of transgenic animals expressing ratiometric sensors, virus-driven genetic alterations, and mass spectrometry proteomic analysis to identify the mechanisms and consequences of mitochondrial pathology in an animal model of MS. Our results have allowed us to draw the following conclusions:

- We revealed a widespread axonal energy deficit in acute inflammatory lesions using a new approach for *in vivo* monitoring of the axonal ATP-to-ADP ratio and found that deficits persist to the chronic phase.
- The energy deficits in inflamed spinal cord axons are neither driven by mitochondrial oxidation nor by calcium overload. Mitochondrial redox imaging indicates that oxidation only occurs at the end stage of FAD. Genetic targeting of the mitochondrial enzyme MnSOD, the principal superoxide scavenger, neither prevents mitochondrial oxidation nor axonal pathology. Likewise, mitochondrial calcium imaging shows that calcium overload occurs only at the end stage of FAD and the molecular manipulation of mitochondrial calcium release by genetically targeting PPIF does not prevent the alterations in mitochondrial morphology and axonal pathology.
- Using a recently established mitochondrial isolation approach, we determined the proteomic profile of GFP-tagged neuronal mitochondria from spinal cord axons and identified differentially regulated proteins and pathways involved in the pathogenesis of EAE. Our data reveals explicitly early alterations in the components of the TCA cycle and suggests that depletion of specific TCA cycle enzymes contributes to mitochondrial dysfunction and axonal energy deficits in neuroinflammatory lesions.

5.2 Widespread energy failure in focal axonal degeneration reinforces the roles of mitochondrial pathology in the pathogenesis of EAE and MS

A previous *in vivo* study from our group has described that mitochondrial damage occurs early during focal axonal degeneration in EAE[1], but the detailed mechanisms of how mitochondrial dysfunction participates in the pathogenesis of FAD has not been thoroughly explored. Of importance are the function of mitochondria in energy production and impairment of their capacities to generate ATP presumably leads to disastrous outcomes.

We attempted to investigate axonal energy status by detecting the ATP-to-ADP ratio in the context of acute and chronic neuroinflammation. To measure this ratio *in vivo,* we used a genetically-encoded biosensor, PercevalHR, with a detectable range fitting the concentration of mammalian cells[99]. The transfer of the phosphoryl group of adenosine triphosphate (ATP), which is the principal metabolite, drives a variety of metabolic reactions, serving as a regulatory modification. Adenosine diphosphate (ADP) is another metabolite in the process of the energy generation; it regulates ATP-dependent enzymes and thus, is considered as a dual system. The ATP-to-ADP ratio is therefore used as a central indicator for monitoring the energy status of a cell, as it is proportional to cellular energy status and phosphorylation potential, profiling the mitochondria function as a readout of energy metabolism[113,114].

Taking advantage of our *in vivo* imaging setup and the newly generated Thy-1 PercevalHR mouse line with stable sensor expression in neurons, we were able to measure the ATP-to-ADP ratio in spinal cord axons in both healthy and diseased conditions. We identified a widespread change of cellular energy with a significant reduction of ATP-to-ADP ratio in all stages of FAD in both acute (peak of disease, Figure 16) and chronic (later time point, Figure 17) inflammatory lesions. This phenomenon was not observed in dorsal roots which are considered as outside the lesion cores, suggesting that energy deficits occur locally in neurons.

Our finding that axonal energy deficits are widespread in acute inflammatory lesions is compatible with previous reports from our group that show that mitochondrial pathology is present in normal-appearing, swollen and fragmented axons in neuroinflammatory lesions. Our data strongly implies that the damaged mitochondria lead to the imbalance of decreased capacity of ATP production together with the excessive energy demand of neurons and their demyelinated axons. A vicious loop occurs when the neurons fail to rebalance the energy supply and demand. This is in line with several studies which have shown the defects of the mitochondrial respiratory chain. For example, loss of cytochrome c oxidase (COX) from complex IV presents in Pattern III multiple sclerosis lesions which are found in early relapsing-remitting multiple sclerosis subtypes characterized by the early loss of myelin-associated glycoprotein (MAG) and cyclic nucleotide phosphodiesterase (CNPase)[72,115].

In addition to white matter pathology, increasing evidence points out that the distribution of neurons with respiratory dysfunction is not restricted to the areas of myelin loss, but also can be found in grey matter in MS patients, indicating a dispersed pattern. Microarray analysis on postmortem non-lesion motor cortex from progressive MS patients demonstrated a significant decrease in gene expression related to oxidative phosphorylation, with the lower activity of complex I and III found in the mitochondria-enriched fraction from MS cortex[48,116]. Subsequently, it was shown that a deficiency of complex IV of the mitochondrial respiratory chain in chronic active lesions in progressive MS correlates with axonal transport deficits seen by the accumulation of amyloid precursor protein and non-phosphorylated neurofilament (SMI-32)[73,74].

One concern about our findings is the pH bias in the PercevalHR signal as the sensor itself is pH-sensitive like many other ratiometric biosensors such as gCaMP and GECO calcium sensors[117,118] and the HyPer hydrogen peroxide sensor[119]. To eliminate the potential pH artefacts due to the acidosis in EAE lesions[120], we calibrated the signals in the PercevalHR

ADP-saturated state by depleting the bindings of ATP to the sensors. The ADP-saturated state was acquired at the end of the experiment by applying either glycolysis inhibitor IAA or mitochondrial uncoupler CCCP[99]. The ATP-to-ADP ratio of CCCP-incubated EAE axons dropped to a level comparable to that observed in CCCP-incubated control axons suggesting that PercevalHR signals in inflammatory lesions indeed primarily reflected a reduced ATP-to-ADP and did not result from a locally altered pH.

Overall, our data helps scientists better understand the axonal energy metabolism in acute neuroinflammation and further addresses other long-standing questions: (i) which molecules are evidently responsible for inadequate ATP supply in EAE and MS? (ii) Can therapies aimed at ameliorating the mitochondrial energetics protect neurons and thereby delay the disease progression of EAE and MS? In addition to what we observed in our *in vivo* data, organelle-specific monitoring is needed further to decrypt the dynamics of ATP-to-ADP in different intracellular compartments since mitochondria control the energy production in cells. This could be achieved by fusing the probe to a mitochondrial targeting sequence or a localized mitochondrial protein.

5.3 Mitochondrial oxidation is unlikely to be a major driver of axonal degeneration in acute neuroinflammatory lesions

The need to better understand the physiological and pathological roles of oxidants has pushed scientists to generate new tools to visualize their actions *in vivo*. It has been postulated that redox signalling joins calcium and kinase signalling in regulating cellular processes and at the same time causes or exacerbates pathological responses through inflicting damage or inducing mutations[121,122]. Newly invented tools have been used to study defined redox pairs in real-time and in a compartment-specific way[123]. The utilization of redox-sensitive GFP[87,88] and the further generation of enzyme-coupled roGFP variants[85,124] have moved the *in vivo* observation off the limits of temporal and spatial restrictions.

In our study, we explored whether mitochondrial oxidation driven by intrinsic sources (by-products of OXPHOS) or extrinsic sources (infiltrating immune cells) occurs during axonal degeneration in EAE[1]. We crossed Thy 1- Mito-Grx1-roGFP2[66] to Thy-1 OFP mice and used *in vivo* imaging to evaluate the mitochondrial GSH/GSSG signals in spinal cord axons. It is crucial to understand at which stage of FAD excessive mitochondrial oxidation occurs as it could be a cause or a consequence of the axonal pathology.

We revealed a progressive change of mitochondrial morphology which resembled the findings in previous work from our group[66] but did not observe an increase of oxidation level in the early stage of FAD in acute inflammation (Figure 18). Oxidative damage happens when ROS is not efficiently eliminated due to excessive production or decreased activities of antioxidant enzymes[125,126]. Our *in vivo* results imply that mitochondrial oxidation is secondary to the FAD in acute EAE, and thus occurs only at the late stage of the degeneration process which is not diminished by transgenically overexpressing antioxidants. These findings elucidate that before coming to the irreversible point of accumulated oxidation stress, the scavengers possibly remain abundant and functional to defend the cells from severe oxidative damage. Besides, neither mitochondrial redox state nor morphological changes of mitochondrial shape were rescued in mice transgenically overexpressing MnSOD (SOD2)[127] which reinforces that the mitochondrial oxidation is neither a prerequisite for the mitochondrial pathology nor for the axonal pathology in acute EAE (Figure 19).

Unchanged oxidation levels detected in the early stages of FAD could result from the reduced ATP-to-ADP ratio referred to be insufficient energy production due to mitochondrial dysfunction in acute inflammatory lesions. Electrons leaking from complex I and III, the major sites at respiratory complexes for ROS production[31,128] causes the partial reduction of oxygen to form superoxides which are subsequently dismutated by dismutases and exclusively transported to the mitochondrial matrix and intermembrane space. However, little is known concerning whether defects at complex I and III are pathologically relevant to the change of mitochondrial oxidation as multiple factors might be in interference[31].

One concern about the findings in our study is that the steady detection of ROS which tends to be short-lasting has been a technical challenge. Previous work from our group has shown that the generation of Thy1- Mito-Grx1-roGFP2 animals facilitates to dissect i*n vivo* the comprehensive information of redox signals. With confocal ratiometric imaging approach, the problem of low temporal resolution was partially circumnavigated. The sensor we applied, Grx1-roGFP2, specifically senses the ratio of a chemically defined pair: reduced and oxidized glutathione (GSH/GSSG) which also means that it does not entirely reflect the entire oxidation status of a given subcellular compartment[129]. Apart from Grx, additional redox pairs like thioredoxin (Trx) and peroxiredoxin (Prx), comprising cysteine residues in the active sites[130], could also be used for ROS detection. For this purpose, the sensor roGFP2-Orp1 was generated as a parallel tool[124]. However, in a previous study in our group, this H_2O_2 sensor was not effectively expressed in mammalian neurons. Furthermore, whether the signal we observed was primarily released from intrinsic source neurons or it was the contribution of exogenous ROS derived from inflammatory cells could not be differentially detected with our sensor which appears to be another limitation.

5.4 Mitochondrial calcium release is unlikely to be a major driver of axonal degeneration in acute neuroinflammatory lesions

In vivo calcium measurement has been well established in our group with the use of Thy 1- CerTN-L15 transgenic animals, which showed bright expression of the CerTN-L15 sensor in a large subset of neurons[131]. On the basis of troponin C and linked to two fluorophores, Cerulean and Citrine, it produces FRET signal following a conformational change induced by calcium-binding. With this particular linker, troponin C, CerTN-L15 has been reported to be independent of the cellular interactions and to respond linearly to elevated cytosolic calcium levels within the physiological range[132].

Improving the sensitivity of genetically encoded calcium indicators (GECI) has been the focus of engineering to resolve calcium fluctuations in the nanomolar range. Twitch-2B, a revised version of Twitch sensors, contains the brighter donor ECFP and a codon-diversified variant of YFP named cpVenusCD, as well as an extended linker. It has a higher signal-to-noise ratio as compared to other genetically encoded FRET indicators. In addition to stronger signals, Twitch-2B-measurements are stable over time, suggesting it can be employed for chronic imaging[109].

In our study, we used a novel transgenic line, Thy 1- MitoTwitch2b animals, to intravitally decipher the dynamic alterations of mitochondrial calcium in acute EAE. Under physiological conditions, the Ca^{2+} influx into mitochondria from the cytosol is in small-scale, especially in comparison with cytosolic extrusion mechanisms[133]. Previous work from our group has shown that cytoplasmic calcium accumulations could predict the fate of axons in the context of neuroinflammation[108]. However, this accumulation is not a “point of no return”, as calcium levels in a certain proportion of swollen axons recover over time along with the morphological changes. This suggests there is a “window of opportunity” under the sustained stress in a neuroinflammatory lesion[134]. In this paradigm, the source of accumulated calcium in the axons is the extracellular space. This is based on the fact that removal of extracellular calcium by incubating the spinal cord with a calcium chelator, EGTA, normalized the abnormal intraaxonal calcium levels. The endoplasmic reticulum (ER), primary storage of intracellular calcium does not play a role, since its depletion did not occur in the early stages of FAD[108].

As a second intracellular reservoir of calcium, mitochondria could be critical mediators in the early stage of FAD. In the context of the acute neuroinflammation, we indeed observed the morphological changes of mitochondria were presented from early to late stages of axonal damages. However, a substantial number of axons with elevated mitochondrial Ca^{2+} only appeared at the end stage of FAD which indicates that the release of mitochondrial calcium into the cytosol is unlikely to explain the early alterations of cytosolic calcium in acute EAE[108] (Figure 20). Thus, the alterations of mitochondrial calcium observed at the late stage of axon degeneration are most likely the downstream result of FAD rather than as the key driver.

To further mechanistically address the relation of mitochondrial calcium and axonal degeneration in neuroinflammatory lesions, we in parallel investigated whether genetic deletion of *Ppif* could effectively protect the axons within the lesions from FAD in acute EAE.

Previous studies have shown that when large amounts of Ca^{2+} accumulate in the mitochondrial matrix, it interacts with cyclophilin D, a product of the *Ppif* gene and a PTP component which was characterized as a target for cyclosporine A, a PTP inhibitor. This interaction further induces the formation and the opening of the permeability transition pore (PTP) which is additionally modulated by, for example, reactive oxygen species (ROS)[135]. The crucial role of cyclophilin D plays in the process of calcium signalling pathways in pathological condition was determined by genetic ablation of cyclophilin D: isolated mitochondria from *Ppif* null mice showed larger calcium buffering capacity. They were resistant to the calcium overload-induced activation of PT[18]. At the same time, cardiac-specific transgenic mice overexpressing cyclophilin D displayed mitochondrial swellings and a higher incidence of spontaneous cell death[18]. The transient opening of the mPTP can occur and allow free calcium to flow across the membrane under physiological conditions.

On the contrary, the continuous opening under pathological conditions leads to the swellings of mitochondria – eventually leading to a ruptured membrane and collapsed membrane potential as well as the further release of intermembrane components such as cytochrome c. The latter ultimately leads to cell death[136]. While protective effects of *Ppif* deletion had been previously described in EAE models[137], in our study, no measurable protection in terms of the differential number of swollen or fragmented axons within the active lesions was observed in homogenous knockout mice (*Ppif*$^{-/-}$) in comparison with heterogeneous knockout mice (*Ppif*$^{+/-}$) (Figure 22). This is consistent with the aforementioned results from our *in vivo* data showing only a late alteration of mitochondrial calcium in acute inflammatory lesions.

On the contrary to the release of mitochondrial calcium through mPTP, mitochondrial Ca^{2+} uptake occurs in response to a substantial rise in cytosolic calcium and drives into unfavourable processes[138] via mitochondrial calcium uniporter. These processes, often accompanied by oxidative stress, are well explored in ischemia models with massive accumulation of glutamate, an excitatory neurotransmitter[139,140]. To further explore the roles of mitochondrial calcium in the context of neuroinflammation, we adopted a floxed mouse model: Mcu^{tm1a} × ACTB: FLPe and are currently studying whether the deletion of MCU could present a protection against the axonal pathology in neuroinflammatory lesions. Intriguingly, calcium influx through MCU is considered to be the principal regulator for calcium uptake which further initiates the formation and the opening of mPTP[141]. Evidence demonstrated that opening of mPTP was abolished in mitochondria isolated from MCU transgenic KO when exposed to high exogenous calcium[142]. Additionally, MCU inhibitors have as well been reported to protect isolated hepatocytes from hypoxia in vitro[89] and to reduce cerebral and cardiac ischemia-reperfusion injury *in vivo*[143]. Further functional assessment to directly measure axonal $[Ca^{2+}]_{Mito}$, under the condition of MCU deletion, would be appealing to see whether there is a neuroprotective effect in acute EAE (Figure 23).

Physiologically, the increase in intra-mitochondrial calcium results from a complex combination of various processes. The inner membrane of mitochondria strictly regulates the passage of calcium by MCU to maintain the high membrane potential required for ATP synthesis[144]. Intra-mitochondrial calcium usually remains low but rises dramatically from 0.1 to 10 μM when the cytosolic calcium is massively increased in response to extrinsic stimuli. The ion channels redistribute along the axons followed by the excessive sodium influxes, flips the directionality of the sodium-calcium exchanger (NCLX), leads to an increase in intra-mitochondrial calcium[49]. This points to calcium regulation as an essential topic in the field. Possible downstream mechanisms as a response to increased axonal calcium and its effect on survival include activation of calcium-dependent proteases, the calcium-induced secondary influx of ions and a disruption of the function of crucial organelles, for example, mitochondrial ATP production[145,146].

To conclude, our results indicate that mitochondrial calcium release is unlikely to be an early event in the pathogenesis of FAD, and the genetic manipulation of main calcium channels on the outer membrane of mitochondria does not affect the progression of axonal degeneration in neuroinflammatory lesions either.

5.5 Investigation of mitochondrial proteins involved in energy failure in the acute EAE

Changes to the mitochondrial proteome are emerging as major pathological substrates in many disease models (metabolic disease and cancer, for instance). Researchers have been profiling size and complexity, as well as the extent of dual localization[147], diversity of different tissues and functional capacities. In our study, we aimed at establishing a comprehensive neuronal mitochondrial proteome profile which hopefully allows us to systemically assess the complexity and the function of this organelle during axonal damage in neuroinflammatory lesions. Studies related to mitochondrial respiratory chain complex deficiency have sprung up in MS research, evidencing damage and potential compromise of the capacity for ATP production in neuronal mitochondria. The energy failure emerged as a consequence coming together with the increased energy demand in demyelinated axons, a typical pathological hallmark in MS. This reinforces the hypothesis that mitochondria indeed play a pivotal role in the pathogenesis of the disease. Another evidence from a global transcript profiling of postmortem tissues from MS brains has also demonstrated that mRNA levels of 26 neuron-specific mitochondrial genes and activities of respiratory complex I and III were reduced[48] - which again strengthens the vital role of mitochondria in MS.

In the following section, we would like to discuss some exciting insights of mitochondrial proteins gained from our survey in the acute EAE. To better show how this organelle takes part in such a complex model, the specific isolation of neuronal mitochondria was combined with a mass-spectrometry-based method for comprehensive proteome analysis. Functional interpretation of the candidates correlated to specific biological processes or molecular functions in our study was explored according to the Gene Ontology (GO) annotation. We, therefore, compared the individual annotated genes in the experimental dataset to the reference dataset in a gene set enrichment analysis (GSEA)[148]. Enrichment analysis of biological pathways by KEGG, Panther or Wiki Pathways (http://www.webgestalt.org/) were performed in a similar way (Data not shown) to validate the functional assignment of our results. Differentially up- or downregulated proteins in relation to certain pathways were determined in acute EAE compared to healthy control to assess the alterations in mitochondrial proteome composition and better understand how they affect the function of mitochondria. TCA and OXPHOS, two obvious differentially regulated pathways, were identified in line with our *in vivo* dataset, illustrating the widespread axonal energy deficits observed in EAE lesions[149-151] (Figure 28).

When interpreting the results of our proteomic analysis, some limitations of our experimental approach have to be considered, in particular, neuroinflammatory lesion reflects a complex environment with alterations in different invading and CNS-resident cell populations. We indeed observed a subset of enriched proteins (i) associated with other subcellular compartments such as ER according to GO annotations and (ii) some mitochondrial proteins which have been reported to be highly expressed in different cell populations. These imply that proteins from several cell types or subcellular compartments were very likely probed along with neuronal mitochondrial proteins when we performed immunocapture. In order to control key results for these experimental limitations and to avoid misinterpretation of the results, relatively conservative criteria were implemented. From the validation experiments, two differentially expressed proteins, Idh3a and Mdh2, were further confirmed by immunohistochemistry staining (Figure 29).

Isocitrate dehydrogenase [NAD] subunit alpha, mitochondrial (IDH3α) is an enzyme encoded by the *IDH3A* and involved in the TCA cycle. It catalyzes the decarboxylation of isocitrate into alpha-ketoglutarate and generates NADH used for ATP production. It was revealed that the loss of Idh3a causes a reduced level of alpha-ketoglutarate that results in the synaptic transmission deficits through an ATP-independent pathway[152]. Another identified missense mutation in *IDH3A* was reported to be a cause of retinal degeneration phenotype in mice[153]. Malate dehydrogenase, mitochondrial (Mdh2), another important enzyme encoded by the *MDH2* gene in TCA cycle, catalyzes the reversible oxidation of malate to oxaloacetate which is accompanied by the transfer of NAD^+ to NADH and further fed into the oxidative phosphorylation (OXPHOS) to produce ATP. Evidence from an *in vitro* model consisting of OPC primary cultures from rat cerebrum incubated with CSF from MS or neuromyelitis optica (NMO) patients have shown downregulation in genes involved in glucose metabolism, including *Mdh2*[153].

To the extent of their function as key elements which are highly related to ATP production, we have shown a significant reduction in expression levels of Idh3a and Mdh2 by proteomics that could be confirmed by immunostaining. These results thus indicate that early alterations of TCA cycle function could be the prime drivers of energy failure in acute neuroinflammatory lesions. To identify whether reduced levels of these proteins could also be seen in MS tissue, we are currently collaborating with Dr. Doron Merkler (Université de Genève) to explore the expression pattern of Idh3a and Mdh2 in human MS lesions. It would be further interesting to investigate the bioenergetics of isolated mitochondria by measuring the oxygen consumption rates (OCR) in the presence of different respiratory substrates such as pyruvate–malate and succinate–rotenone[154]. Thereby one could determine the efficiency of OXPHOS, the capacity of mitochondrial substrate oxidation, and elucidate the association of OXPHOS and glycolysis in acute EAE.

Furthermore, it would be important to investigate the coordination among mitochondria from different cell types[155]. Based on the proof of glia sensing neuronal metabolic needs, the function of the astrocyte-neuron lactate shuttle (ANLSH)[156] indicates the possibility of astrocytic mitochondria to chaperone energy as a regular basis in healthy conditions and to regulate metabolism correspondingly by transferring metabolites to neurons for further oxidation and energy production. Additional investigations on how mitochondria mediate the energy flow in glia-axon metabolic interactions could bring another point of view in the field of neuroinflammation [157,158].

Taken together, our proteomic data, bioinformatics analysis and histological confirmation provide new insights into the molecular alterations that are induced in neuronal mitochondria in acute neuroinflammatory lesions and suggest a critical role of TCA cycle enzymes in the induction of axonal energy deficits.

5.6 Concluding remarks

The contribution of mitochondria to disease pathogenesis and pathology has recently moved into the focus of multiple sclerosis research. This study aimed to better understand the role of mitochondria during immune-mediated axon degeneration in a mouse model of MS. We first revealed an extensive reduction of ATP-to-ADP ratio in EAE spinal cord axons, indicating a widespread energy deficit that persisted in chronic lesions stages. Furthermore, results from our *in vivo* imaging experiments however overruled the hypothesis that mitochondrial reactive species and calcium were the prime drivers in the initiation of axonal degeneration as elevated mitochondrial redox and calcium levels were only observed at the end stage of the axonal degeneration process. To reveal alternative substrates of mitochondrial pathology, we profiled neuronal mitochondrial proteins in the inflamed spinal cord using a cell-type-specific mitochondrial tagging approach[112]. Our results show that members of the TCA cycle and in particular the enzymes Idh3 and Mdh2 are prominently depleted in neuronal mitochondria exposed to neuroinflammatory lesions. These molecular alterations likely contribute to the axonal energy deficits we observed in neuroinflammatory lesions and could thus represent potential therapeutic targets for counteracting metabolic disturbances in MS.

6. References

1 Nikic, I. *et al.* A reversible form of axon damage in experimental autoimmune encephalomyelitis and multiple sclerosis. *Nat Med* **17**, 495-499, doi:10.1038/nm.2324 (2011).

2 Lublin, F. History of modern multiple sclerosis therapy. *J Neurol* **252 Suppl 3**, iii3-iii9, doi:10.1007/s00415-005-2010-6 (2005).

3 Filippi, M. *et al.* Multiple sclerosis. *Nat Rev Dis Primers* **4**, 43, doi:10.1038/s41572-018-0041-4 (2018).

4 Compston, A. & Coles, A. Multiple sclerosis. *Lancet* **372**, 1502-1517, doi:10.1016/S0140-6736(08)61620-7 (2008).

5 Thompson, A. J. *et al.* Diagnosis of multiple sclerosis: 2017 revisions of the McDonald criteria. *Lancet Neurol* **17**, 162-173, doi:10.1016/S1474-4422(17)30470-2 (2018).

6 Petersen, G., Wittmann, R., Arndt, V. & Gopffarth, D. [Epidemiology of multiple sclerosis in Germany: regional differences and drug prescription in the claims data of the statutory health insurance]. *Nervenarzt* **85**, 990-998, doi:10.1007/s00115-014-4097-4 (2014).

7 Orton, S. M. *et al.* Sex ratio of multiple sclerosis in Canada: a longitudinal study. *Lancet Neurol* **5**, 932-936, doi:10.1016/S1474-4422(06)70581-6 (2006).

8 Gale, C. R. & Martyn, C. N. Migrant studies in multiple sclerosis. *Prog Neurobiol* **47**, 425-448 (1995).

9 Compston, A. & Coles, A. Multiple sclerosis. *Lancet* **359**, 1221-1231, doi:10.1016/S0140-6736(02)08220-X (2002).

10 Poser, C. M. Viking voyages: the origin of multiple sclerosis? An essay in medical history. *Acta Neurol Scand Suppl* **161**, 11-22, doi:10.1111/j.1600-0404.1995.tb05852.x (1995).

11 Poser, C. M. Prevalence of multiple sclerosis. *Ann Neurol* **32**, 716-717; author reply 718-719, doi:10.1002/ana.410320520 (1992).

12 Barcellos, L. F. *et al.* Heterogeneity at the HLA-DRB1 locus and risk for multiple sclerosis. *Hum Mol Genet* **15**, 2813-2824, doi:10.1093/hmg/ddl223 (2006).

13 Dyment, D. A., Ebers, G. C. & Sadovnick, A. D. Genetics of multiple sclerosis. *Lancet Neurol* **3**, 104-110, doi:10.1016/s1474-4422(03)00663-x (2004).

14 International Multiple Sclerosis Genetics, C. Multiple sclerosis genomic map implicates peripheral immune cells and microglia in susceptibility. *Science* **365**, doi:10.1126/science.aav7188 (2019).

15 Levin, L. I., Munger, K. L., O'Reilly, E. J., Falk, K. I. & Ascherio, A. Primary infection with the Epstein-Barr virus and risk of multiple sclerosis. *Ann Neurol* **67**, 824-830, doi:10.1002/ana.21978 (2010).

16 Lunemann, J. D. *et al.* EBNA1-specific T cells from patients with multiple sclerosis cross react with myelin antigens and co-produce IFN-gamma and IL-2. *J Exp Med* **205**, 1763-1773, doi:10.1084/jem.20072397 (2008).

17 Mora, J. R., Iwata, M. & von Andrian, U. H. Vitamin effects on the immune system: vitamins A and D take centre stage. *Nat Rev Immunol* **8**, 685-698, doi:10.1038/nri2378 (2008).

18 Baines, C. P. *et al.* Loss of cyclophilin D reveals a critical role for mitochondrial permeability transition in cell death. *Nature* **434**, 658-662, doi:10.1038/nature03434 (2005).

19 Simpson, S., Jr. *et al.* Higher 25-hydroxyvitamin D is associated with lower relapse risk

in multiple sclerosis. *Ann Neurol* **68**, 193-203, doi:10.1002/ana.22043 (2010).

20 May, E., Asadullah, K. & Zugel, U. Immunoregulation through 1,25-dihydroxyvitamin D3 and its analogs. *Curr Drug Targets Inflamm Allergy* **3**, 377-393, doi:10.2174/1568010042634596 (2004).

21 McLaughlin, L. *et al.* Vitamin D for the treatment of multiple sclerosis: a meta-analysis. *J Neurol* **265**, 2893-2905, doi:10.1007/s00415-018-9074-6 (2018).

22 McDonald, W. I. *et al.* Recommended diagnostic criteria for multiple sclerosis: guidelines from the International Panel on the diagnosis of multiple sclerosis. *Ann Neurol* **50**, 121-127, doi:10.1002/ana.1032 (2001).

23 Lublin, F. D. New multiple sclerosis phenotypic classification. *Eur Neurol* **72 Suppl 1**, 1-5, doi:10.1159/000367614 (2014).

24 Lublin, F. D. *et al.* Defining the clinical course of multiple sclerosis: the 2013 revisions. *Neurology* **83**, 278-286, doi:10.1212/WNL.0000000000000560 (2014).

25 Tintore, M. & Montalban, X. The optic nerve should be included as one of the typical CNS regions for establishing dissemination in space when diagnosing MS - No. *Mult Scler* **24**, 123-125, doi:10.1177/1352458517729451 (2018).

26 Tintore, M., Vidal-Jordana, A. & Sastre-Garriga, J. Treatment of multiple sclerosis - success from bench to bedside. *Nat Rev Neurol* **15**, 53-58, doi:10.1038/s41582-018-0082-z (2019).

27 Cohen, J. A. *et al.* Alemtuzumab versus interferon beta 1a as first-line treatment for patients with relapsing-remitting multiple sclerosis: a randomised controlled phase 3 trial. *Lancet* **380**, 1819-1828, doi:10.1016/S0140-6736(12)61769-3 (2012).

28 Coles, A. J. *et al.* Alemtuzumab for patients with relapsing multiple sclerosis after disease-modifying therapy: a randomised controlled phase 3 trial. *Lancet* **380**, 1829-1839, doi:10.1016/S0140-6736(12)61768-1 (2012).

29 Ruck, T. *et al.* Vitiligo after alemtuzumab treatment: Secondary autoimmunity is not all about B cells. *Neurology* **91**, e2233-e2237, doi:10.1212/WNL.0000000000006648 (2018).

30 Barkhof, F. *et al.* Onset of clinical and MRI efficacy of ocrelizumab in relapsing multiple sclerosis. *Neurology* **93**, e1778-e1786, doi:10.1212/WNL.0000000000008189 (2019).

31 Murphy, M. P. How mitochondria produce reactive oxygen species. *Biochem J* **417**, 1-13, doi:10.1042/BJ20081386 (2009).

32 Pelletier, D. & Hafler, D. A. Fingolimod for multiple sclerosis. *N Engl J Med* **366**, 339-347, doi:10.1056/NEJMct1101691 (2012).

33 Kappos, L. *et al.* Siponimod versus placebo in secondary progressive multiple sclerosis (EXPAND): a double-blind, randomised, phase 3 study. *Lancet* **391**, 1263-1273, doi:10.1016/S0140-6736(18)30475-6 (2018).

34 Pelz, A. *et al.* S1P receptor antagonists fingolimod and siponimod do not improve the outcome of experimental autoimmune myasthenia gravis mice after disease onset. *Eur J Immunol* **48**, 498-508, doi:10.1002/eji.201747187 (2018).

35 Fox, R. J. *et al.* Phase 2 Trial of Ibudilast in Progressive Multiple Sclerosis. *N Engl J Med* **379**, 846-855, doi:10.1056/NEJMoa1803583 (2018).

36 Schumacher, A.-M., Mahler, C. & Kerschensteiner, M. Pathology and Pathogenesis of Progressive Multiple Sclerosis: Concepts and Controversies. *Neurology International Open* **01**, E171-E181, doi:10.1055/s-0043-106704 (2017).

37 Rubin, R. "Smoldering" Brain Lesions Might Signal Severe Multiple Sclerosis. *JAMA* **322**, 1133, doi:10.1001/jama.2019.14344 (2019).

38 Frischer, J. M. *et al.* The relation between inflammation and neurodegeneration in

multiple sclerosis brains. *Brain* **132**, 1175-1189, doi:10.1093/brain/awp070 (2009).

39 Frischer, J. M. *et al.* Clinical and pathological insights into the dynamic nature of the white matter multiple sclerosis plaque. *Ann Neurol* **78**, 710-721, doi:10.1002/ana.24497 (2015).

40 Barnett, M. H. & Prineas, J. W. Relapsing and remitting multiple sclerosis: pathology of the newly forming lesion. *Ann Neurol* **55**, 458-468, doi:10.1002/ana.20016 (2004).

41 Steinman, L., Martin, R., Bernard, C., Conlon, P. & Oksenberg, J. R. Multiple sclerosis: deeper understanding of its pathogenesis reveals new targets for therapy. *Annu Rev Neurosci* **25**, 491-505, doi:10.1146/annurev.neuro.25.112701.142913 (2002).

42 Hemmer, B., Kerschensteiner, M. & Korn, T. Role of the innate and adaptive immune responses in the course of multiple sclerosis. *Lancet Neurol* **14**, 406-419, doi:10.1016/S1474-4422(14)70305-9 (2015).

43 Korn, T. & Kallies, A. T cell responses in the central nervous system. *Nat Rev Immunol* **17**, 179-194, doi:10.1038/nri.2016.144 (2017).

44 Haider, L. *et al.* Multiple sclerosis deep grey matter: the relation between demyelination, neurodegeneration, inflammation and iron. *J Neurol Neurosurg Psychiatry* **85**, 1386-1395, doi:10.1136/jnnp-2014-307712 (2014).

45 Sorbara, C. D. *et al.* Pervasive axonal transport deficits in multiple sclerosis models. *Neuron* **84**, 1183-1190, doi:10.1016/j.neuron.2014.11.006 (2014).

46 Trapp, B. D. & Stys, P. K. Virtual hypoxia and chronic necrosis of demyelinated axons in multiple sclerosis. *Lancet Neurol* **8**, 280-291, doi:10.1016/S1474-4422(09)70043-2 (2009).

47 Stys, P. K. Axonal degeneration in multiple sclerosis: is it time for neuroprotective strategies? *Ann Neurol* **55**, 601-603, doi:10.1002/ana.20082 (2004).

48 Dutta, R. *et al.* Mitochondrial dysfunction as a cause of axonal degeneration in multiple sclerosis patients. *Ann Neurol* **59**, 478-489, doi:10.1002/ana.20736 (2006).

49 Waxman, S. G. Axonal conduction and injury in multiple sclerosis: the role of sodium channels. *Nat Rev Neurosci* **7**, 932-941, doi:10.1038/nrn2023 (2006).

50 Rivers, T. M., Sprunt, D. H. & Berry, G. P. Observations on Attempts to Produce Acute Disseminated Encephalomyelitis in Monkeys. *J Exp Med* **58**, 39-53, doi:10.1084/jem.58.1.39 (1933).

51 Rivers, T. M. & Schwentker, F. F. Encephalomyelitis Accompanied by Myelin Destruction Experimentally Produced in Monkeys. *J Exp Med* **61**, 689-702, doi:10.1084/jem.61.5.689 (1935).

52 Ransohoff, R. M. Animal models of multiple sclerosis: the good, the bad and the bottom line. *Nat Neurosci* **15**, 1074-1077, doi:10.1038/nn.3168 (2012).

53 Kabat, E. A., Wolf, A. & Bezer, A. E. The Rapid Production of Acute Disseminated Encephalomyelitis in Rhesus Monkeys by Injection of Heterologous and Homologous Brain Tissue with Adjuvants. *J Exp Med* **85**, 117-130, doi:10.1084/jem.85.1.117 (1947).

54 Steinman, L. Assessment of animal models for MS and demyelinating disease in the design of rational therapy. *Neuron* **24**, 511-514, doi:10.1016/s0896-6273(00)81107-1 (1999).

55 Stromnes, I. M. & Goverman, J. M. Active induction of experimental allergic encephalomyelitis. *Nat Protoc* **1**, 1810-1819, doi:10.1038/nprot.2006.285 (2006).

56 Jones, M. V. *et al.* Behavioral and pathological outcomes in MOG 35-55 experimental autoimmune encephalomyelitis. *J Neuroimmunol* **199**, 83-93, doi:10.1016/j.jneuroim.2008.05.013 (2008).

57 Krishnamoorthy, G. *et al.* Myelin-specific T cells also recognize neuronal autoantigen in a transgenic mouse model of multiple sclerosis. *Nat Med* **15**, 626-632,

doi:10.1038/nm.1975 (2009).

58 Stromnes, I. M. & Goverman, J. M. Passive induction of experimental allergic encephalomyelitis. *Nat Protoc* **1**, 1952-1960, doi:10.1038/nprot.2006.284 (2006).

59 Anderson, S. *et al.* Sequence and organization of the human mitochondrial genome. *Nature* **290**, 457-465, doi:10.1038/290457a0 (1981).

60 Macreadie, I. G. *et al.* Biogenesis of mitochondria: the mitochondrial gene (aap1) coding for mitochondrial ATPase subunit 8 in Saccharomyces cerevisiae. *Nucleic Acids Res* **11**, 4435-4451, doi:10.1093/nar/11.13.4435 (1983).

61 Chomyn, A. *et al.* URF6, last unidentified reading frame of human mtDNA, codes for an NADH dehydrogenase subunit. *Science* **234**, 614-618, doi:10.1126/science.3764430 (1986).

62 Carafoli, E. The calcium-signalling saga: tap water and protein crystals. *Nat Rev Mol Cell Biol* **4**, 326-332, doi:10.1038/nrm1073 (2003).

63 Gincel, D., Zaid, H. & Shoshan-Barmatz, V. Calcium binding and translocation by the voltage-dependent anion channel: a possible regulatory mechanism in mitochondrial function. *Biochem J* **358**, 147-155, doi:10.1042/0264-6021:3580147 (2001).

64 Kirichok, Y., Krapivinsky, G. & Clapham, D. E. The mitochondrial calcium uniporter is a highly selective ion channel. *Nature* **427**, 360-364, doi:10.1038/nature02246 (2004).

65 Shoshan-Barmatz, V. & Gincel, D. The voltage-dependent anion channel: characterization, modulation, and role in mitochondrial function in cell life and death. *Cell Biochem Biophys* **39**, 279-292, doi:10.1385/CBB:39:3:279 (2003).

66 Breckwoldt, M. O. *et al.* Multiparametric optical analysis of mitochondrial redox signals during neuronal physiology and pathology in vivo. *Nat Med* **20**, 555-560, doi:10.1038/nm.3520 (2014).

67 Giacomello, M., Pyakurel, A., Glytsou, C. & Scorrano, L. The cell biology of mitochondrial membrane dynamics. *Nat Rev Mol Cell Biol* **21**, 204-224, doi:10.1038/s41580-020-0210-7 (2020).

68 Sies, H. & Jones, D. P. Reactive oxygen species (ROS) as pleiotropic physiological signalling agents. *Nat Rev Mol Cell Biol*, doi:10.1038/s41580-020-0230-3 (2020).

69 Bristow, E. A., Griffiths, P. G., Andrews, R. M., Johnson, M. A. & Turnbull, D. M. The distribution of mitochondrial activity in relation to optic nerve structure. *Arch Ophthalmol* **120**, 791-796, doi:10.1001/archopht.120.6.791 (2002).

70 Barron, M. J., Griffiths, P., Turnbull, D. M., Bates, D. & Nichols, P. The distributions of mitochondria and sodium channels reflect the specific energy requirements and conduction properties of the human optic nerve head. *Br J Ophthalmol* **88**, 286-290, doi:10.1136/bjo.2003.027664 (2004).

71 DiMauro, S., Schon, E. A., Carelli, V. & Hirano, M. The clinical maze of mitochondrial neurology. *Nat Rev Neurol* **9**, 429-444, doi:10.1038/nrneurol.2013.126 (2013).

72 Mahad, D., Ziabreva, I., Lassmann, H. & Turnbull, D. Mitochondrial defects in acute multiple sclerosis lesions. *Brain* **131**, 1722-1735, doi:10.1093/brain/awn105 (2008).

73 Mahad, D. J. *et al.* Detection of cytochrome c oxidase activity and mitochondrial proteins in single cells. *J Neurosci Methods* **184**, 310-319, doi:10.1016/j.jneumeth.2009.08.020 (2009).

74 Mahad, D. J. *et al.* Mitochondrial changes within axons in multiple sclerosis. *Brain* **132**, 1161-1174, doi:10.1093/brain/awp046 (2009).

75 Campbell, G. R. *et al.* Mitochondrial DNA deletions and neurodegeneration in multiple sclerosis. *Ann Neurol* **69**, 481-492, doi:10.1002/ana.22109 (2011).

76 Mahad, D. H., Trapp, B. D. & Lassmann, H. Pathological mechanisms in progressive multiple sclerosis. *Lancet Neurol* **14**, 183-193, doi:10.1016/S1474-4422(14)70256-X

(2015).

77 Cahalan, M. D., Parker, I., Wei, S. H. & Miller, M. J. Two-photon tissue imaging: seeing the immune system in a fresh light. *Nat Rev Immunol* **2**, 872-880, doi:10.1038/nri935 (2002).

78 Denk, W., Strickler, J. H. & Webb, W. W. Two-photon laser scanning fluorescence microscopy. *Science* **248**, 73-76, doi:10.1126/science.2321027 (1990).

79 Helmchen, F. & Denk, W. Deep tissue two-photon microscopy. *Nat Methods* **2**, 932-940, doi:10.1038/nmeth818 (2005).

80 Misgeld, T. & Kerschensteiner, M. In vivo imaging of the diseased nervous system. *Nat Rev Neurosci* **7**, 449-463, doi:10.1038/nrn1905 (2006).

81 Pfrieger, F. W. & Slezak, M. Genetic approaches to study glial cells in the rodent brain. *Glia* **60**, 681-701, doi:10.1002/glia.22283 (2012).

82 Feng, G. *et al.* Imaging neuronal subsets in transgenic mice expressing multiple spectral variants of GFP. *Neuron* **28**, 41-51, doi:10.1016/s0896-6273(00)00084-2 (2000).

83 Misgeld, T., Kerschensteiner, M., Bareyre, F. M., Burgess, R. W. & Lichtman, J. W. Imaging axonal transport of mitochondria in vivo. *Nat Methods* **4**, 559-561, doi:10.1038/nmeth1055 (2007).

84 Kleele, T. *et al.* An assay to image neuronal microtubule dynamics in mice. *Nat Commun* **5**, 4827, doi:10.1038/ncomms5827 (2014).

85 Gutscher, M. *et al.* Real-time imaging of the intracellular glutathione redox potential. *Nat Methods* **5**, 553-559, doi:10.1038/nmeth.1212 (2008).

86 Tantama, M., Hung, Y. P. & Yellen, G. Imaging intracellular pH in live cells with a genetically encoded red fluorescent protein sensor. *J Am Chem Soc* **133**, 10034-10037, doi:10.1021/ja202902d (2011).

87 Dooley, C. T. *et al.* Imaging dynamic redox changes in mammalian cells with green fluorescent protein indicators. *J Biol Chem* **279**, 22284-22293, doi:10.1074/jbc.M312847200 (2004).

88 Hanson, G. T. *et al.* Investigating mitochondrial redox potential with redox-sensitive green fluorescent protein indicators. *J Biol Chem* **279**, 13044-13053, doi:10.1074/jbc.M312846200 (2004).

89 Schwarzlander, M., Fricker, M. D. & Sweetlove, L. J. Monitoring the in vivo redox state of plant mitochondria: effect of respiratory inhibitors, abiotic stress and assessment of recovery from oxidative challenge. *Biochim Biophys Acta* **1787**, 468-475, doi:10.1016/j.bbabio.2009.01.020 (2009).

90 Roma, L. P. *et al.* Dynamic measurements of mitochondrial hydrogen peroxide concentration and glutathione redox state in rat pancreatic beta-cells using ratiometric fluorescent proteins: confounding effects of pH with HyPer but not roGFP1. *Biochem J* **441**, 971-978, doi:10.1042/BJ20111770 (2012).

91 Grienberger, C. & Konnerth, A. Imaging calcium in neurons. *Neuron* **73**, 862-885, doi:10.1016/j.neuron.2012.02.011 (2012).

92 Garaschuk, O., Griesbeck, O. & Konnerth, A. Troponin C-based biosensors: a new family of genetically encoded indicators for in vivo calcium imaging in the nervous system. *Cell Calcium* **42**, 351-361, doi:10.1016/j.ceca.2007.02.011 (2007).

93 Jares-Erijman, E. A. & Jovin, T. M. FRET imaging. *Nat Biotechnol* **21**, 1387-1395, doi:10.1038/nbt896 (2003).

94 Miyawaki, A. *et al.* Fluorescent indicators for Ca2+ based on green fluorescent proteins and calmodulin. *Nature* **388**, 882-887, doi:10.1038/42264 (1997).

95 Yildiz, I., Gao, X., Harris, T. K. & Raymo, F. M. Fluorescence resonance energy transfer in quantum dot-protein kinase assemblies. *J Biomed Biotechnol* **2007**, 18081,

doi:10.1155/2007/18081 (2007).

96 Yildiz, O., Kalthoff, C., Raunser, S. & Kuhlbrandt, W. Structure of GlnK1 with bound effectors indicates regulatory mechanism for ammonia uptake. *EMBO J* **26**, 589-599, doi:10.1038/sj.emboj.7601492 (2007).

97 Morikofer-Zwez, S. & Walter, P. Binding of ADP to rat liver cytosolic proteins and its influence on the ratio of free ATP/free ADP. *Biochem J* **259**, 117-124, doi:10.1042/bj2590117 (1989).

98 Meglasson, M. D., Smith, K. M., Nelson, D. & Erecinska, M. alpha-Glycerophosphate shuttle in a clonal beta-cell line. *Am J Physiol* **256**, E173-178, doi:10.1152/ajpendo.1989.256.1.E173 (1989).

99 Tantama, M., Martinez-Francois, J. R., Mongeon, R. & Yellen, G. Imaging energy status in live cells with a fluorescent biosensor of the intracellular ATP-to-ADP ratio. *Nat Commun* **4**, 2550, doi:10.1038/ncomms3550 (2013).

100 Imamura, H. & Noji, H. [Imaging of intracellular ATP using novel fluorescent probes]. *Tanpakushitsu Kakusan Koso* **54**, 1937-1944 (2009).

101 Imamura, H. *et al.* Visualization of ATP levels inside single living cells with fluorescence resonance energy transfer-based genetically encoded indicators. *Proc Natl Acad Sci U S A* **106**, 15651-15656, doi:10.1073/pnas.0904764106 (2009).

102 Bermejo, C., Haerizadeh, F., Takanaga, H., Chermak, D. & Frommer, W. B. Optical sensors for measuring dynamic changes of cytosolic metabolite levels in yeast. *Nat Protoc* **6**, 1806-1817, doi:10.1038/nprot.2011.391 (2011).

103 Calvo, S. E., Clauser, K. R. & Mootha, V. K. MitoCarta2.0: an updated inventory of mammalian mitochondrial proteins. *Nucleic Acids Res* **44**, D1251-1257, doi:10.1093/nar/gkv1003 (2016).

104 Andrews, H. *et al.* Increased axonal mitochondrial activity as an adaptation to myelin deficiency in the Shiverer mouse. *J Neurosci Res* **83**, 1533-1539, doi:10.1002/jnr.20842 (2006).

105 Kerschensteiner, M., Schwab, M. E., Lichtman, J. W. & Misgeld, T. In vivo imaging of axonal degeneration and regeneration in the injured spinal cord. *Nat Med* **11**, 572-577, doi:10.1038/nm1229 (2005).

106 Keller, J. N. *et al.* Mitochondrial manganese superoxide dismutase prevents neural apoptosis and reduces ischemic brain injury: suppression of peroxynitrite production, lipid peroxidation, and mitochondrial dysfunction. *J Neurosci* **18**, 687-697 (1998).

107 Schinzel, A. C. *et al.* Cyclophilin D is a component of mitochondrial permeability transition and mediates neuronal cell death after focal cerebral ischemia. *Proc Natl Acad Sci U S A* **102**, 12005-12010, doi:10.1073/pnas.0505294102 (2005).

108 Witte, M. E. *et al.* Calcium Influx through Plasma-Membrane Nanoruptures Drives Axon Degeneration in a Model of Multiple Sclerosis. *Neuron* **101**, 615-624 e615, doi:10.1016/j.neuron.2018.12.023 (2019).

109 Thestrup, T. *et al.* Optimized ratiometric calcium sensors for functional in vivo imaging of neurons and T lymphocytes. *Nat Methods* **11**, 175-182, doi:10.1038/nmeth.2773 (2014).

110 Barrientos, S. A. *et al.* Axonal degeneration is mediated by the mitochondrial permeability transition pore. *J Neurosci* **31**, 966-978, doi:10.1523/JNEUROSCI.4065-10.2011 (2011).

111 Giorgio, V. *et al.* Dimers of mitochondrial ATP synthase form the permeability transition pore. *Proc Natl Acad Sci U S A* **110**, 5887-5892, doi:10.1073/pnas.1217823110 (2013).

112 Fecher, C. *et al.* Cell-type-specific profiling of brain mitochondria reveals functional and molecular diversity. *Nat Neurosci* **22**, 1731-1742, doi:10.1038/s41593-019-0479-z

(2019).

113 Veech, R. L., Lawson, J. W., Cornell, N. W. & Krebs, H. A. Cytosolic phosphorylation potential. *J Biol Chem* **254**, 6538-6547 (1979).

114 Metallo, C. M. & Vander Heiden, M. G. Understanding metabolic regulation and its influence on cell physiology. *Mol Cell* **49**, 388-398, doi:10.1016/j.molcel.2013.01.018 (2013).

115 Lucchinetti, C. *et al.* Heterogeneity of multiple sclerosis lesions: implications for the pathogenesis of demyelination. *Ann Neurol* **47**, 707-717, doi:10.1002/1531-8249(200006)47:6<707::aid-ana3>3.0.co;2-q (2000).

116 Dutta, R. & Trapp, B. D. [Pathology and definition of multiple sclerosis]. *Rev Prat* **56**, 1293-1298 (2006).

117 Akerboom, J. *et al.* Optimization of a GCaMP calcium indicator for neural activity imaging. *J Neurosci* **32**, 13819-13840, doi:10.1523/JNEUROSCI.2601-12.2012 (2012).

118 Zhao, Y. *et al.* An expanded palette of genetically encoded Ca(2)(+) indicators. *Science* **333**, 1888-1891, doi:10.1126/science.1208592 (2011).

119 Belousov, V. V. *et al.* Genetically encoded fluorescent indicator for intracellular hydrogen peroxide. *Nat Methods* **3**, 281-286, doi:10.1038/nmeth866 (2006).

120 Friese, M. A. *et al.* Acid-sensing ion channel-1 contributes to axonal degeneration in autoimmune inflammation of the central nervous system. *Nat Med* **13**, 1483-1489, doi:10.1038/nm1668 (2007).

121 Houstis, N., Rosen, E. D. & Lander, E. S. Reactive oxygen species have a causal role in multiple forms of insulin resistance. *Nature* **440**, 944-948, doi:10.1038/nature04634 (2006).

122 Lin, M. T. & Beal, M. F. Mitochondrial dysfunction and oxidative stress in neurodegenerative diseases. *Nature* **443**, 787-795, doi:10.1038/nature05292 (2006).

123 Herrmann, J. M. & Dick, T. P. Redox Biology on the rise. *Biol Chem* **393**, 999-1004, doi:10.1515/hsz-2012-0111 (2012).

124 Gutscher, M. *et al.* Proximity-based protein thiol oxidation by H2O2-scavenging peroxidases. *J Biol Chem* **284**, 31532-31540, doi:10.1074/jbc.M109.059246 (2009).

125 Wang, Y., Branicky, R., Noe, A. & Hekimi, S. Superoxide dismutases: Dual roles in controlling ROS damage and regulating ROS signaling. *J Cell Biol* **217**, 1915-1928, doi:10.1083/jcb.201708007 (2018).

126 Holmstrom, K. M. & Finkel, T. Cellular mechanisms and physiological consequences of redox-dependent signalling. *Nat Rev Mol Cell Biol* **15**, 411-421, doi:10.1038/nrm3801 (2014).

127 Miriyala, S. *et al.* Manganese superoxide dismutase, MnSOD and its mimics. *Biochim Biophys Acta* **1822**, 794-814, doi:10.1016/j.bbadis.2011.12.002 (2012).

128 Chouchani, E. T. *et al.* Ischaemic accumulation of succinate controls reperfusion injury through mitochondrial ROS. *Nature* **515**, 431-435, doi:10.1038/nature13909 (2014).

129 Albrecht, S. C., Barata, A. G., Grosshans, J., Teleman, A. A. & Dick, T. P. In vivo mapping of hydrogen peroxide and oxidized glutathione reveals chemical and regional specificity of redox homeostasis. *Cell Metab* **14**, 819-829, doi:10.1016/j.cmet.2011.10.010 (2011).

130 Winterbourn, C. C. Reconciling the chemistry and biology of reactive oxygen species. *Nat Chem Biol* **4**, 278-286, doi:10.1038/nchembio.85 (2008).

131 Heim, N. *et al.* Improved calcium imaging in transgenic mice expressing a troponin C-based biosensor. *Nat Methods* **4**, 127-129, doi:10.1038/nmeth1009 (2007).

132 Direnberger, S. *et al.* Biocompatibility of a genetically encoded calcium indicator in a transgenic mouse model. *Nat Commun* **3**, 1031, doi:10.1038/ncomms2035 (2012).

133 Kamer, K. J. & Mootha, V. K. The molecular era of the mitochondrial calcium uniporter. *Nat Rev Mol Cell Biol* **16**, 545-553, doi:10.1038/nrm4039 (2015).

134 Williams, P. R. *et al.* A recoverable state of axon injury persists for hours after spinal cord contusion in vivo. *Nat Commun* **5**, 5683, doi:10.1038/ncomms6683 (2014).

135 Zorov, D. B., Filburn, C. R., Klotz, L. O., Zweier, J. L. & Sollott, S. J. Reactive oxygen species (ROS)-induced ROS release: a new phenomenon accompanying induction of the mitochondrial permeability transition in cardiac myocytes. *J Exp Med* **192**, 1001-1014, doi:10.1084/jem.192.7.1001 (2000).

136 Crompton, M. The mitochondrial permeability transition pore and its role in cell death. *Biochem J* **341 (Pt 2)**, 233-249 (1999).

137 Forte, M. *et al.* Cyclophilin D inactivation protects axons in experimental autoimmune encephalomyelitis, an animal model of multiple sclerosis. *Proc Natl Acad Sci U S A* **104**, 7558-7563, doi:10.1073/pnas.0702228104 (2007).

138 Nicholls, D. G. & Crompton, M. Mitochondrial calcium transport. *FEBS Lett* **111**, 261-268, doi:10.1016/0014-5793(80)80806-4 (1980).

139 Szatkowski, M. & Attwell, D. Triggering and execution of neuronal death in brain ischaemia: two phases of glutamate release by different mechanisms. *Trends Neurosci* **17**, 359-365, doi:10.1016/0166-2236(94)90040-x (1994).

140 Choi, K. T., Chung, J. K., Kwak, C. S. & Kim, H. K. Effect of hypocapnia on extracellular glutamate and glycine concentrations during peri-ischemic period in the rabbit hippocampus. *J Korean Med Sci* **9**, 394-401, doi:10.3346/jkms.1994.9.5.394 (1994).

141 Rizzuto, R., De Stefani, D., Raffaello, A. & Mammucari, C. Mitochondria as sensors and regulators of calcium signalling. *Nat Rev Mol Cell Biol* **13**, 566-578, doi:10.1038/nrm3412 (2012).

142 Pan, X. *et al.* The physiological role of mitochondrial calcium revealed by mice lacking the mitochondrial calcium uniporter. *Nat Cell Biol* **15**, 1464-1472, doi:10.1038/ncb2868 (2013).

143 Zhao, Q. *et al.* The role of the mitochondrial calcium uniporter in cerebral ischemia/reperfusion injury in rats involves regulation of mitochondrial energy metabolism. *Mol Med Rep* **7**, 1073-1080, doi:10.3892/mmr.2013.1321 (2013).

144 Giorgi, C., Marchi, S. & Pinton, P. The machineries, regulation and cellular functions of mitochondrial calcium. *Nat Rev Mol Cell Biol* **19**, 713-730, doi:10.1038/s41580-018-0052-8 (2018).

145 Bano, D. & Ankarcrona, M. Beyond the critical point: An overview of excitotoxicity, calcium overload and the downstream consequences. *Neurosci Lett* **663**, 79-85, doi:10.1016/j.neulet.2017.08.048 (2018).

146 Friese, M. A., Schattling, B. & Fugger, L. Mechanisms of neurodegeneration and axonal dysfunction in multiple sclerosis. *Nat Rev Neurol* **10**, 225-238, doi:10.1038/nrneurol.2014.37 (2014).

147 Yogev, O. & Pines, O. Dual targeting of mitochondrial proteins: mechanism, regulation and function. *Biochim Biophys Acta* **1808**, 1012-1020, doi:10.1016/j.bbamem.2010.07.004 (2011).

148 Subramanian, A. *et al.* Gene set enrichment analysis: a knowledge-based approach for interpreting genome-wide expression profiles. *Proc Natl Acad Sci U S A* **102**, 15545-15550, doi:10.1073/pnas.0506580102 (2005).

149 Curtis, R. K., Oresic, M. & Vidal-Puig, A. Pathways to the analysis of microarray data. *Trends Biotechnol* **23**, 429-435, doi:10.1016/j.tibtech.2005.05.011 (2005).

150 Jassal, B. *et al.* The reactome pathway knowledgebase. *Nucleic Acids Res* **48**, D498-

D503, doi:10.1093/nar/gkz1031 (2020).

151 Werner, T. Bioinformatics applications for pathway analysis of microarray data. *Curr Opin Biotechnol* **19**, 50-54, doi:10.1016/j.copbio.2007.11.005 (2008).

152 Ugur, B. *et al.* The Krebs Cycle Enzyme Isocitrate Dehydrogenase 3A Couples Mitochondrial Metabolism to Synaptic Transmission. *Cell Rep* **21**, 3794-3806, doi:10.1016/j.celrep.2017.12.005 (2017).

153 Findlay, A. S. *et al.* Mouse Idh3a mutations cause retinal degeneration and reduced mitochondrial function. *Dis Model Mech* **11**, doi:10.1242/dmm.036426 (2018).

154 Divakaruni, A. S., Paradyse, A., Ferrick, D. A., Murphy, A. N. & Jastroch, M. Analysis and interpretation of microplate-based oxygen consumption and pH data. *Methods Enzymol* **547**, 309-354, doi:10.1016/B978-0-12-801415-8.00016-3 (2014).

155 Stobart, J. L. & Anderson, C. M. Multifunctional role of astrocytes as gatekeepers of neuronal energy supply. *Front Cell Neurosci* **7**, 38, doi:10.3389/fncel.2013.00038 (2013).

156 Pellerin, L. & Magistretti, P. J. Glutamate uptake into astrocytes stimulates aerobic glycolysis: a mechanism coupling neuronal activity to glucose utilization. *Proc Natl Acad Sci U S A* **91**, 10625-10629, doi:10.1073/pnas.91.22.10625 (1994).

157 Mathur, D., Lopez-Rodas, G., Casanova, B. & Marti, M. B. Perturbed glucose metabolism: insights into multiple sclerosis pathogenesis. *Front Neurol* **5**, 250, doi:10.3389/fneur.2014.00250 (2014).

158 Senanayake, V. K., Jin, W., Mochizuki, A., Chitou, B. & Goodenowe, D. B. Metabolic dysfunctions in multiple sclerosis: implications as to causation, early detection, and treatment, a case control study. *BMC Neurol* **15**, 154, doi:10.1186/s12883-015-0411-4 (2015).

Acknowledgement

I am here at the end of my PhD life but just at the beginning of my scientific career, with tons of appreciation, I want to show my gratitude to my supervisors: Prof. Dr. Martin Kerschensteiner and Prof. Dr. Thomas Misgeld. Thank you for giving me the opportunity to work on a fascinating project, for your patient guidance, constructive support, and encouragement. Your ambitions, hardworking attitude and passion for science were so inspiring to me. Thank you to Prof. Dr. Mikael Simons and Dr. Fabiana Perocchi for your support and valuable comments as members of my thesis committee.

LIFE HAS NEVER BEEN EASY! But my life is definitely easier with these people around: I am so lucky to spend my first-abroad years working in two fantastic labs, with many brilliant colleagues, friends inside and outside the lab. Countless long-evenings with coffee-experiments-beer-discussions; weekend/night out for food hunting, GoT sessions and gin tasting; (gradually increased levels in terms of walking time and difficulty) hiking tours; short trips to different countries/cities; clubbing after imaging or vice versa, all of these memories have become nutrition nourishing my routine life.

Special thanks to Beppe and Delph, being my mentors teaching me all I need to know in the lab. Thanks to my labbies: Paula, for all the help and suggestions (even when you are on maternity leave, miss you and your warm hug); Ole, for sharing the bench (our territory :P) and the time working/chatting in the dark 2-P room; Daniel, for your help on all-kind in general, particularly as a translator and a mental health consultant; Arek, for sharing long-evenings in the lab; Minh, for always answering the questions and the emergency call even when you were on-call in the ER; Anja, Berni, Bianca, Dana, Manuela, Monika, Nebi, Petra and Yvonne, things wouldn’t be done if not for your help. People from my extended office in the small lab, thank you for the fun time we had (too drunk to remember what exactly we did, shh). Thanks to all the members from AG Kerschensteiner, AG Misgeld, AG Bareyre and two amazing institutes.

Of course, I am blessed to be here pursuing my dream because of you, my parents and family back in Taiwan, with your love, caring and endless support. To my friends in Taiwan and all over the world, thank you for being there for me. You are the reason that I could be me.

“Fear of doing something is reason enough to do it”. I do not know what will be my next, but I do know I will stay brave and strong to face the challenges with great passion and knowledge I have learned from these years in Munich.

List of publications

Marta Joana Costa Jordão, Roman Sankowski, Stefanie M. Brendecke1, Sagar, Giuseppe Locatelli, **Yi-Heng Tai**, Tuan Leng Tay, Eva Schramm, Stephan Armbruster, Nora Hagemeyer, Olaf Groß, Dominic Mai, Özgün Çiçek, Thorsten Falk, Martin Kerschensteiner, Dominic Grün, Marco Prinz. Single-cell profiling identifies myeloid cell subsets with distinct fates during neuroinflammation. Science. 2019

Yi-Heng Tai, Yu-Yi Lin, Kai-Chen Wang, Chao-Lin Chang, Ru-Yin Chen, Chia-Chu Wu, Irene H. Cheng. Curcuminoid submicron particle ameliorates cognitive deficits and decreases amyloid pathology in Alzheimer's disease mouse model. Oncotarget. 2018